

Optimum and Robust Geometric Design of Mechanical Parts

Dulyachot Cholaseuk

Submitted in partial fulfillment of the
requirements for the degree
of Doctor of Philosophy
in the Graduate School of Arts and Sciences

COLUMBIA UNIVERSITY

2001

© 2001
Dulyachot Cholaseuk
All Rights Reserved

ABSTRACT

Optimum and Robust Designs of Mechanical Parts

Dulyachot Cholaseuk

Some problems in constrained geometric optimization are considered. The goal has been to maximize or minimize a measure of device performance computed using CAE, with a CAD compatible representation and specified geometric constraints. This approach illustrates several issues in the integration of CAD and CAE systems. The free-form geometry of the device is represented by Bezier curves. Analysis tools such as a grid generator and the solver for device's performance are treated as a black box. The search pattern during the optimization process is suggested by the design of experiment methodology. The proposed framework is tested with four example problems: flow through a ninety degree bend in potential flow problem, a plane diffusers in laminar flow, an axisymmetric diffuser in laminar flow and a torque arm under static load. In all four problems the free form shape of the part is to be designed.

An optimum design is not an acceptable engineering solution unless it is also robust. For this reason, a method to identify robust designs of mechanical parts with free-form shapes is proposed. We attempt to quantify the robustness of a design by, first,

introducing noise to the design using a design of experiments approach. With this approach a fixed number of samples are generated around the design. Then we evaluate the performance of all the samples. Next, four quantities are computed, which are the mean, standard deviation, probability of failure and Taguchi's signal-to-noise ratio (*SNR*). Finally, these four quantities are used to compare the robustness between different designs. The methodology is applied to the designs obtained from the four example optimization problems. The results show that an optimum design is not necessarily robust.

The previously mentioned portion of this work can be classified as a single objective design but, in practice, design problems usually involve multiple criteria. In the later part of the thesis we explore a multicriteria design problem. For this purpose the design of corrugated panel structures, a fixed form geometric design problem, is examined. The goal of this exercise is to find guidelines for robust-optimum design of these structures. For design optimization the objectives include maximizing natural frequency and minimizing maximum deflection for a given range of structural weight. The objectives of robust design are to maximize *SNR* with respect to natural frequency and maximum deflection. We consider all the objectives for optimality as well as robustness to formulate a multicriteria design problem. To solve this multicriteria design problem, a large data set of trial designs is generated over a range of structural weight. This data set not only allows us to perform an exhaustive search but also to fill the design space for robustness testing. A finite element model is created for each trial design to solve for natural frequency and maximum deflection. The finite element solver is, again,

treated as a black box. *SNR* are then computed by gathering the information from the neighborhood of each design. The data set is then screened and reduced to a smaller set of feasible designs. Finally a set of robust-optimum designs is identified and design rules are extracted from this design set.

Table of Contents

Chapter 1 Introduction	1
1.1 Principles of engineering design	5
1.2 Overview of optimization problems	7
Chapter 2 Representation of the Freeform Geometry	10
2.1 Interpolation splines	13
2.2 Bezier curves	14
2.3 B-spline curves	16
2.4 Sensitivity of a NURBS curve to movements its of control points	18
Chapter 3 Optimization Techniques	21
3.1 Single objective optimization	22
3.1.1 Newton method	23
3.1.2 Steepest descent method	23
3.1.3 Design of experiments method	24
3.1.4 Comparison of single objective optimization techniques	30
3.2 Multicriteria optimization	32
3.2.1 Weight objectives	32

3.2.2 Min-max method	32
3.2.3 Goal programming	33
3.2.4 Global criteria method	33
3.2.5 Parameter space investigation method	34
Chapter 4 Optimum Geometric Design of Freeform Mechanical Parts	35
4.1 Optimization procedures	38
4.2 Algorithm for geometric optimization	40
4.3 Example problems	43
4.3.1 Ninety-degree bend in potential flow	43
4.3.2 Plane symmetric diffuser in laminar flow	46
4.3.3 Axisymmetric diffuser in laminar flow	52
4.3.4 Torque arm under static load	53
4.4 Discussion	57
Chapter 5 Robustness Analysis of Freeform Mechanical Parts	61
5.1 Methodology for robustness testing	64
5.1.1 Noise in freeform geometry	66
5.1.2 Signal-to-noise ratios	68
5.1.3 Probability of failure	71
5.2 Example problems	72
5.2.1 Ninety-degree bend in potential flow	72
5.2.2 Plane symmetric diffuser in laminar flow	72

5.2.3	Axisymmetric diffuser in laminar flow	73
5.2.4	Torque arm under static load	73
5.3	Discussion	78
Chapter 6 Designs of Corrugated Panel Structures		82
6.1	Theoretical background	87
6.2	Data generation	91
6.2.1	Modeling assumptions	93
6.2.2	Validation of similarity	94
6.2.3	Trial design generation	96
6.2.4	Results of numerical experiments	100
6.3	Data analysis	102
6.3.1	Robustness analysis	102
6.3.2	Feasible solutions	105
6.3.3	Pareto robust-optimum solutions	111
6.3.4	Guideline for robust-optimum design	115
6.4	Example problems	124
6.4.1	Corrugated panel structure with deflection constraint	124
6.4.2	Corrugated panel structure with deflection and height constraint	125
6.5	Discussion	126
6.5.1	Sensitivity analysis	126
6.5.2	Effect of numbers of samples on signal-to-noise ratios	128
6.5.3	Stress	129

6.5.4 Applications of design rules	130
Chapter 7 Concluding Remarks	132
Bibliography	135
Appendix	
A. Multi-dimensional response surface fitting	139
B. Validation of the black-box solvers	141
B.1 Potential flow solver	142
B.2 Laminar flow solver – CAFFA	143
B.3 Static finite element solver	145
B.4 I-DEAS linear statics and normal mode dynamics solvers	146
C. Batch mode program for I-DEAS Master Series 7	148

Chapter 1

Introduction

Design of mechanical parts frequently requires many engineering considerations, the primary ones being that the parts must provide the desired performance, they must be manufacturable and they must be robust. Designers also seek ways to improve an existing design to improve performance or for example to reduce its weight without a loss of performance. These considerations have been the subject of much academic research termed design optimization. Lack of consideration of all the primary issues however may sometimes lead to designs are either un-manufacturable or non-robust. To remedy this problem, the work reported in this thesis focuses on the issues of both robustness and optimality of a design.

The use of computer-aided design (CAD) systems for describing geometry is now commonplace in industry. Complex shapes can be defined by a few control points using NURBS in order to efficiently describe, store and transmit geometry. These systems have been integrated with computer-aided manufacturing (CAM) systems to generate geometric representations of steps involved in manufacture of the part - e.g., tool paths for a CNC machine. The last three decades have also seen considerable advances in the

use of computational techniques (e.g., boundary integral, finite element, finite difference, finite volume techniques) for the analysis of mechanical problems. These computational techniques fall in the realm of Computer Aided Engineering (CAE) systems. The maturing of CAE systems has led to the possibility of systematic improvements in design to achieve desirable properties and performance. When formalized this process is sometimes called “design optimization” if the performance can be characterized by an objective function and the design is systematically altered until the objective function is satisfied. Such a process now also falls within in the realm of CAE. Chapters 2 and 3 provide related details on CAD and CAE. In Chapter 2, techniques for efficient representation of freeform geometry are presented. Some selected optimization techniques are compared in Chapter 3 and techniques suitable for this thesis are selected.

Traditionally, analysis and design optimization (CAE components) have been carried out without considering the advantages or limitations afforded by CAD systems. In Chapter 4 the emphasis is placed on integration of the parametric representation of shape by CAD systems with CAE analysis tools and design optimization techniques. Bezier curves are used for representation of designed geometry, which is then optimized by means of gradient-based pattern search methods. CAE analysis tools such as the grid generators and the solvers for objective functions are treated as a “black box”. The proposed framework is tested with several design problems in fluid mechanics and elastic structures.

A method to identify robust designs of mechanical parts with free-form shapes is proposed in Chapter 5. For each design, the geometry and operating conditions represent one design point in the design space, with noise altering the design point leading to a change in performance. Robustness analysis is a process of quantifying such change. To demonstrate the methodology, robustness analysis is performed on the design problems examined in Chapter 4. For each problem, a set of iterative designs is generated during the optimization process with the final one being the optimum design. A design of experiments (DOE) approach is used to apply noise in order to generate samples around each and every iterative design point. Subsequently, we evaluate the performance of the samples. The mean, standard deviation of performance, probability of failure and signal-to-noise ratio (*SNR*) (Taguchi, 1986) are then computed and used to compare the robustness of all the designs. The results from the example problems show that an optimum design is not necessarily robust.

In Chapters 4 and 5 the focus is on design of freeform parts. In practice, however there may be constraints that limit the designs to fixed forms. Chapter 6 focuses corrugated panel structures, a class of fixed form mechanical parts of industrial importance. These parts are of a fixed form that is easily to manufacture and generally provides high strength to weight ratio. They are however frequently prone to vibration, a problem common to plate and shell structures. With proper design the vibration problem can be minimized while maintaining the strength of the structure. Here we attempt to find design guidelines for optimum and robust corrugated panel structures. For design optimization the objectives include minimizing weight, maximizing natural frequency

and minimizing maximum deflection. Robustness analysis is performed on all the designs using signal-to-noise ratio. The objectives of robust design are to maximize SNR with respect to natural frequency and to maximize SNR with respect to maximum deflection. We considered both the design objectives for optimality and those for robustness and form a multicriteria design optimization problem. The outcomes of this process are robust-optimum designs. Proposed design rules are extracted from those robust-optimum designs.

The major technical contribution of this thesis is to provide a methodology that demonstrates how existing CAD and CAE tools can be integrated to design robust and optimum mechanical parts. The CAD tools are used to generate design instances. The CAE tools are used as function evaluators. Optimum and robust design methods are wrapped around these “design instance generators” and “function evaluators”.

Concluding remarks are presented in Chapter 7. The “black box” solvers used in this study are described in the appendix. The sections that follow in this chapter provide brief overview of engineering design principles, and optimal design problems to show how our work fits in to the big picture.

1.1 Principles of engineering design

Engineering design is a part of the product development process. According to Ulrich and Eppinger (1995), a generic product development process can be drawn roughly as shown Fig. 1.1. Our work fits within the engineering function of the detail design stage.



Figure 1.1 Product development process.

As said earlier, the primary considerations in engineering design are functionality, manufacturability and reliability. However as technological advancements and market competitiveness urge designers to set higher standards; better performance, time-to-market, quality and cost also become significant. To deal with these issues, various engineering design principles have emerged. Some of them are:

Optimal design: Design to maximize performance under limited resources (constraints).

Probabilistic design (Haugen, 1968): Using means and standard deviations in the computation instead of nominal values for design variables and/or operating conditions, providing designers with probabilistic information.

Robust design (Phadke, 1989): Design to reduce sensitivity to variations.

Axiomatic design (Suh, 1990): This design principle is at conceptual or system level. In an ideal design, functional requirements (or design objectives) and design variables should have a one-to-one relationship.

Design for manufacturing and assembly or ***DFMA*** (Boothroyd, et. al. 1994): Reduce production cost and time and increase product quality by considering manufacturing and assembly issues during the design stage.

Product Platform Design (Meyer and Lehnerd, 1997): Design parts as common parts that can be used in a variety of products. This requires a compromise of multiple objectives of the parts for different products.

Key characteristics or ***KCs*** (Lee and Thornton, 1995): Key characteristics are features whose variations have the most effect on the overall product. Designers should identify and pay special attention to those features.

Single objective optimum design without consideration of other issues may leads to a design that is very sensitive to variations (not robust) or is not manufacturable. This research is built around the use of design optimization. The next section discusses some of the well-known categories of optimization problems and solution techniques.

1.2 Overview of design optimization problems

To optimize the design is to find values of the design variables that minimize or maximize the objective function while satisfying the constraints (if there are any). For example one might want to maximize the surface quality of the machined parts by treating turning speed, tool tip radius and feed rate as design variables. Design optimization is a very broad area. Table 1 provides some of the possible classifications of the optimization problem by different criteria.

Table 1 Classification of optimization problems.

Criteria	Classes
Constraint	Constrained*/unconstrained*
Continuity of design space	Continuous*/discrete/mixed-type
Number of Objective function	Single-objective*/multiple-objective*
Type of objective function	Linear/non-linear*; differentiable/non-differentiable*; Deterministic*/stochastic
Objective	Local*/global
Application specific	Geometric*/topology*/network/combinatorial/queuing/ space planning/scheduling and etc.

The asterisks indicate the classes that are applicable to this research. Solution techniques depend on the particular type of problem. In general the techniques can be categorized as direct and indirect techniques. The direct or analytical techniques use principles of variational calculus to analytically obtain the optimum solution.

Applications of such techniques are limited because most engineering problems are too complex to solve analytically. Indirect techniques improve the designs iteratively. They require more computation but take less time to develop. They are more versatile and due the speed of today's computer hardware and software, indirect techniques have become choice in engineering practice.

The following is a list of some well-known indirect techniques for single-objective optimization.

Gradient-based methods

These methods require derivative (gradient) information to move a design toward local optima. Examples of these methods are steepest descent method and Newton methods (and their modifications). In general a global optimum is not guaranteed. If the derivative information cannot be obtained analytically, finite difference techniques or response surface fits can be used to obtain the approximate information.

Zero-th order methods

These methods do not use derivative information but rely on logic and strategy. They usually incur more direct solutions than a gradient-based method. Examples of these methods are random search, pattern search, genetic algorithm and simulated annealing.

Mixtures of gradient-based and zero-th order techniques are also used. The techniques mentioned could also be used in multicriteria optimization. To do so, multiple objectives are reduced to a single objective by methods such as the weighted sum of objectives, min-max method and goal programming. This approach requires that different priorities be set for the objectives. Usually a single solution is expected. If, however, the priorities are not clear, exhaustive methods such as parameter space investigation are used to generate a feasible solution set and a set of extreme designs called “Pareto optimum solutions” are selected from the feasible solution set. More details of the indirect optimization techniques that are related to this work can be found in Chapter 3.

Chapter 2

Representations of Freeform Geometry

The representation of part geometry should allow the design space to be explored by as few parameters as possible in order to minimize computational effort. It would also be desirable for this representation to be compatible with CAD tools. Interpolation splines and NURBS such as B-spline and Bezier curves provide economic ways to describe freeform geometry. With a few control points these representations allow the shape of complex freeform geometry be controlled. This enables the development of an approximate mathematical model of the relationship between an objective function and the control point locations. The objective of shape optimization is then one of finding the locations of the control points that correspond to the optimum shape. These techniques are applicable to multi-dimensional geometry (curves, surfaces and hyper-surfaces) but since in the applications of interest in this study only two-dimensional geometry is required, we only discuss two-dimensional curves in this chapter.

Let $\mathbf{P}_i = \{x_i, y_i\}, i = 0, 1, 2, \dots, n$ be a set of $n + 1$ control points and $\mathbf{P}(t) = \{x(t), y(t)\}$ be a point on a curve defined by the control points at a parametric value t . Different representations can be used to relate control points to points on a curve. The frequently used representations are shown in Fig. 2.1a to d with the same set of control points. The mathematical formulations for those curves are discussed in Sections 2.1 to 2.3. Section 2.4 is an additional section that discusses the relationship between the movements of the control points and the geometry of a NURBS curve.

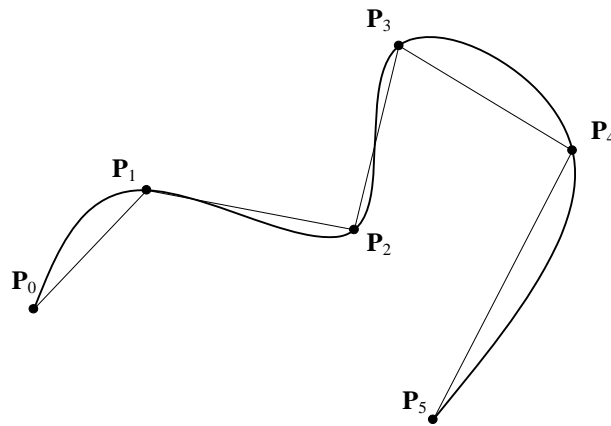


Figure 2.1a Natural cubic interpolation spline.

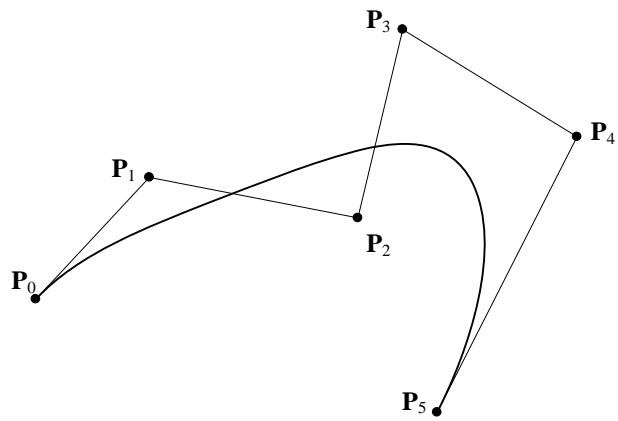


Figure 2.1b Bezier curve.

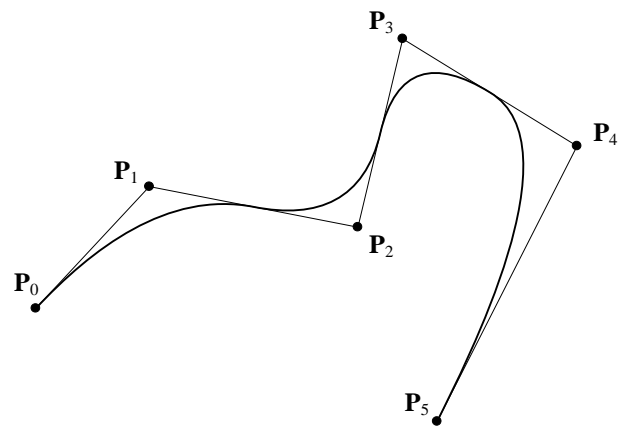


Figure 2.1c Quadratic B-spline curve.

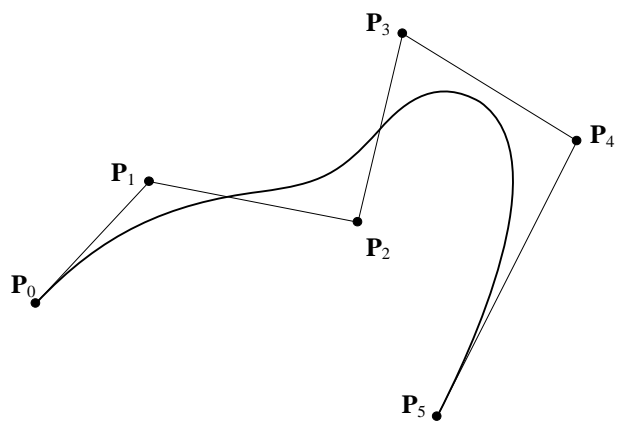


Figure 2.1d Cubic B-spline curve.

2.1 Interpolation splines

An interpolation spline is a set of piecewise curves. The most common form is a cubic spline, which has continuous first and second derivatives. Between two consecutive points a piece of curve defined parametrically by a cubic polynomial is used to connect the two points. Following Ferziger (1998) a cubic polynomial in parametric form joining \mathbf{P}_i and \mathbf{P}_{i+1} can be written as

$$\mathbf{P}(t) = \mathbf{P}_i \frac{(t_{i+1} - t_i)^3}{6\Delta_i} + \mathbf{P}_{i+1} \frac{(t - t_i)^3}{6\Delta_i} + \left[\frac{\mathbf{P}_i}{\Delta_i} - \frac{\Delta_i}{6} \mathbf{P}_i'' \right] (t_{i+1} - t_i) + \left[\frac{\mathbf{P}_{i+1}}{\Delta_i} - \frac{\Delta_i}{6} \mathbf{P}_{i+1}'' \right] (t - t_i) \quad (2.1)$$

where $\Delta_i = t_{i+1} - t_i$. Note that the index i starts from zero. The parameter t_i can be assigned to \mathbf{P}_i as proportion to the total distance of straight lines running from \mathbf{P}_0 to \mathbf{P}_i , i.e. $t_0 = 0$, $t_i = t_{i-1} + \sqrt{(x_i - x_{i-1})^2 + (y_i - y_{i-1})^2}$ or as uniform value proportional to the index value i.e. $t_i = i$.

To solve for the second derivatives, \mathbf{P}_i'' 's, differentiate the polynomials in Eq. 2.1 and match the values of the first derivatives at the control points; this provides the set of linear tridiagonal equations:

$$\frac{\Delta_{i-1}}{6} \mathbf{P}_{i-1}'' + \frac{(\Delta_{i-1} + \Delta_i)}{3} \mathbf{P}_i'' + \frac{\Delta_i}{6} \mathbf{P}_{i+1}'' = \frac{\mathbf{P}_{i+1} + \mathbf{P}_i}{\Delta_i} + \frac{\mathbf{P}_i + \mathbf{P}_{i-1}}{\Delta_{i-1}} \quad (2.2)$$

Different end conditions can be specified in Eq. 2.2; for examples with $n + 1$ control points \mathbf{P}_0'' and $\mathbf{P}_n'' = 0$ provides natural spline, $\mathbf{P}_0'' = \mathbf{P}_{n-1}''$ and $\mathbf{P}_n'' = \mathbf{P}_1''$ is a periodic spline.

The good property of this type of spline is that the control points lie on the curve but the main disadvantage is that the curve exhibits oscillating or wiggle behavior that can be hard to control. One possible solution is to use tensioned spline but then the curve become computationally more expensive. Moreover, different amount of tension must be determined for different geometry.

2.2 Bezier curves

Bezier curves are the most basic form of NURBS. Unlike interpolation splines, the control points in this case do not necessarily lie on the curve or surface they represent. A Bezier curve with $n + 1$ control points is an n^{th} degree Bezier curve. Mathematically an n^{th} degree Bezier curve can be evaluated in a parametric form by the following equation.

$$\mathbf{P}(t) = \sum_{i=0}^n B_i^n(t) \mathbf{P}_i \quad (2.3)$$

where $0 \leq t \leq 1$ and B_i^n are basis functions, which are Bernstein polynomials,

$$B_i^n(t) = \frac{n!}{i!(n-i)!} (1-t)^{n-i} t^i. \quad \text{Note that the Bernstein polynomials can be evaluated}$$

robustly by de Casteljau algorithm, which are repeated convex interpolations of control points (see Farin, 1993 and Hoschek and Lasser, 1993). Each Bezier curve is a one-piece curve; this means a movement of one control point affects the shape of the whole curve.

Some useful geometrical properties of the Bezier curves are

1. Convex hull: A planar Bezier curve always lays inside the convex hull formed by its control points (Fig. 2.2).

2. End slopes: The slope at each end of a Bezier curve always equals to the slope of the corresponding polyline that connects the end control point to the adjacent control point.

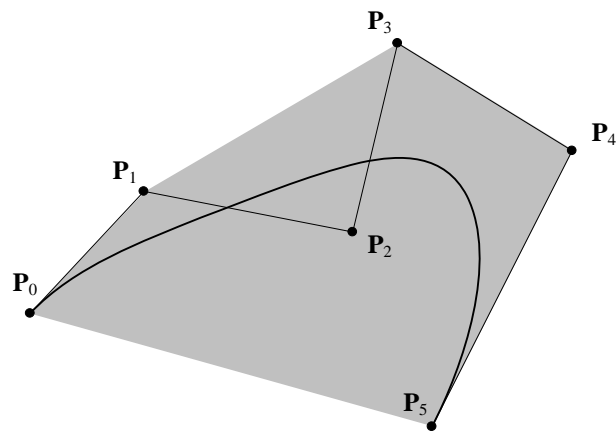


Figure 2.2 Convex hull property of a Bezier curve. Shaded area represents the convex hull.

3. Degree elevation: An n^{th} -degree Bezier curve can be exactly represented by a $(n + 1)^{\text{th}}$ -degree Bezier curve as shown in Fig. 2.3. Locations of the new set of control points \mathbf{P}_i^* can be computed as

$$\mathbf{P}_i^* = \begin{cases} \mathbf{P}_0 & \text{if } i = 0 \\ \left(\frac{i}{n+1}\right)\mathbf{P}_{i-1} + \left(1 - \frac{i}{n+1}\right)\mathbf{P}_i & \text{if } 1 \leq i \leq n \\ \mathbf{P}_n & \text{if } i = n + 1. \end{cases} \quad (2.4)$$

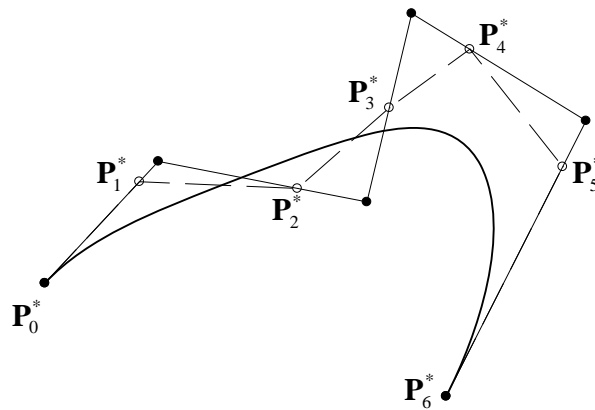


Figure 2.3 Degree elevation of Bezier curve.

Despite their useful properties, Bezier curves have some disadvantages. The curves are sometimes considered too stiff, i.e. the curves are less sensitive to the movement of the control points. Also as control points increase, the Bernstein polynomials are of a higher degree, resulting in costly computation. The use of B-splines alleviates these problems.

2.3 B-spline curves

A B-spline curve is a set of piece wise curves with each piece being a Bezier curve. A B-spline curve of order k consists of $n - k + 1$ Bezier curves of degree $k - 1$ joined together at the break points. In addition to control points, B-spline curves depend on a knot vector. A set of parametric values t_i 's form a knot vector

$$T = \{t_0, t_1, t_2, \dots, t_{n+k}\}.$$

Examples of $k = 2$ and 3 are shown in Fig. 2.1c and d respectively.

The steps to draw a B-spline curve of k order are the following. First, determine the knot vector, the simplest being the uniform knot sequences in Eq. 2.5

$$t_i = \begin{cases} 0 & \text{if } i < k \\ i - k + 1 & \text{if } k \leq i \leq n \\ i - k + 2 & \text{if } i > n \end{cases} \quad (2.5)$$

Next step is to obtain B-spline basis function $N_i^k(t)$ from

$$N_i^1(t) = \begin{cases} 1 & \text{if } t_i \leq t < t_{i+1} \\ 0 & \text{otherwise} \end{cases} \quad (2.6)$$

and use the recursive formula in Eq. (2.7) to compute the higher order basis functions.

$$N_i^k(t) = \frac{(t - t_i)}{(t_{i+k-1} - t_i)} N_i^{k-1}(t) + \frac{(t_{i+k} - t)}{(t_{i+k} - t_{i+1})} N_{i+1}^{k-1}(t) \quad (2.7)$$

Then compute the coordinate on the B-spline curve by Eq. (2.8).

$$\mathbf{P}(t) = \sum_{i=0}^n N_i^k(t) \mathbf{P}_i \quad (2.8)$$

Note that more flexibility can be added to a B-spline curve by using non-uniform knot sequences and assigning additional weighting factors to the terms in Eq. 2.8; in doing so the curve becomes a NURBS curve. In addition to control point locations, control parameters for a NURBS curve are knot values and weighting factors.

B-spline curves have the same convex hull and end slopes properties as Bezier curves but not the degree elevation property. Note that when $k = n + 1$ B-spline curves become the same as the Bezier curves. Using Eq. 2.4 to increase number of control points

will change the shape of the curves. Instead one can increase the number of control points without changing the shape of the B-spline curve by knot insertion. The knot insertion process requires specific information, i.e. one has to specify where to add the new control points, which is not preferred in this study because the information about location of the new control points is not available. Details about knot insertion and all other aspects of B-spline curves can be found in Farin (1993).

2.4 Sensitivity of a NURBS curve to movements of its control points

In order to use control points as the design variables and vary them to obtain optimum geometry as mentioned in the introduction, we need to know the sensitivity of the geometry of the curve to the variations in control point locations. This issue has been explored by Pottmann et. al. (2000) using the notation of “tolerance zones”. The development of a tolerance zone is based on the result of convex combination of two convex domains as shown in Fig. 2.4.

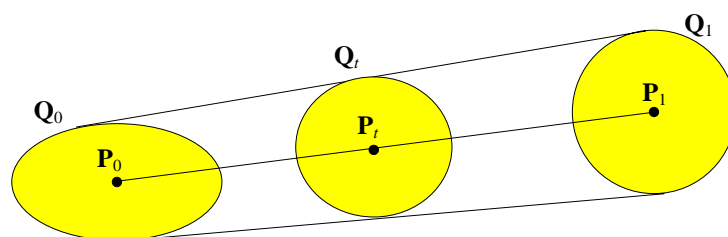


Figure 2.4 Linear interpolation of convex tolerance zones Q_0 and Q_1 .

Given points \mathbf{P}_0 and \mathbf{P}_1 with corresponding convex tolerance regions \mathbf{Q}_0 and \mathbf{Q}_1 such that $\mathbf{P}_0 \in \mathbf{Q}_0$ and $\mathbf{P}_1 \in \mathbf{Q}_1$, the point \mathbf{P}_t defined by a linear interpolation of \mathbf{P}_0 and \mathbf{P}_1

$$\mathbf{P}_t = (1 - t)\mathbf{P}_0 + t\mathbf{P}_1,$$

we seek the tolerance zone \mathbf{Q}_t such that $\mathbf{P}_t \in \mathbf{Q}_t$. Pottmann et. al. (2000) show that \mathbf{Q}_t is given by a linear interpolation of \mathbf{Q}_0 and \mathbf{Q}_1

$$\mathbf{Q}_t = (1 - t)\mathbf{Q}_0 + t\mathbf{Q}_1.$$

As mentioned in section 2.2, Bernstein polynomials, which are the basis functions for all the NURBS curves can also be constructed using repeated convex interpolations of control points (de Casteljau algorithm). This allows the application of the tolerance zone idea for NURBS curves. The simplified result is: if the tolerance zones of the control points are of the same shape \mathbf{Z} then the tolerance zone of the NURBS curve is formed by sweeping \mathbf{Z} along the nominal curve. Fig. 2.5 shows an example where \mathbf{Z} is a circular zone. Note that this result is not applicable to the interpolation splines. The more complex cases where control points have different shapes of tolerance zones can be found in Pottmann et. al. (2000).

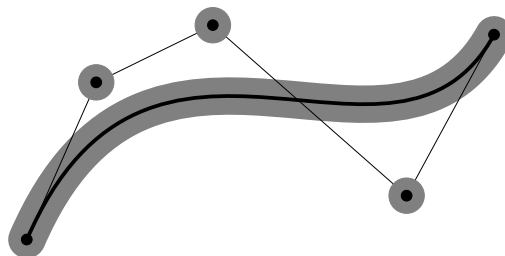


Figure 2.5 Tolerance zones of control points and of the corresponding NURBS curve.

Later, when we need to generate several shapes in the neighborhood of the original design shape, we will use this tolerance zone idea. We will choose instances of control points from a neighborhood Z centered at the original location of the control points. We are then guaranteed that the resulting curves will all lie within the swept tolerance zone as shown in Fig. 2.5.

Chapter 3

Optimization Techniques

Optimization techniques can be classified into two types, direct and indirect techniques. The direct or analytical techniques use principles of variational calculus to analytically obtain the optimum solutions. Applications of these techniques are limited because most engineering problems are too complex to solve analytically. Indirect techniques improve a design iteratively. They require more computation but take less time to develop. They are more versatile and due to the high speed and low cost of computing, indirect techniques have emerged as the preferred techniques. This chapter presents some of the indirect optimization techniques that are related to the work in this thesis. To discuss optimization techniques, it is necessary to introduce some mathematical notations. First, let us define the optimization problem as

Find \mathbf{d} that minimize (or maximize) $\mathbf{F}(\mathbf{d})$.

Here \mathbf{F} is a set of objective functions (vector quantity) $\mathbf{F} = (f_1, f_2, f_3, \dots, f_m)^T$, $m = 1$ for single-objective and $m > 1$ for multiple-objective or the so-called *multicriteria optimization* problems. \mathbf{d} is a set of design variables (or the so-called design point or

design vector or just “design”), $\mathbf{d} = (d_1, d_2, d_3, \dots, d_n)^T$ and n is number of design variables or degrees of freedom (D.O.F.) or the so-called dimension of the design space.

The following are a few techniques that are well known for single-objective and multicriteria optimization problems in engineering applications.

3.1 Single objective optimization

Optimization methods presented in this section require derivatives or sensitivity information to iteratively improve a design. Two of the fundamental methods are presented in 3.1.1 and 3.1.2. We only consider the cases where the derivative information cannot be obtained analytically, but can be estimated by design of experiments techniques described in section 3.1.3. Solutions by these methods are usually local optima. The normal practice is to move a design in the direction that should improve an objective function. This can be written as

$$\mathbf{d}^* = \mathbf{d} + \alpha \mathbf{s} \quad (3.1)$$

where \mathbf{d}^* is a new design, \mathbf{d} is an existing design, α is an adjustment coefficient and \mathbf{s} is a direction vector. The design becomes optimum when the size of the gradient reaches zero. There are many methods to compute the direction vector; the following are two basic methods illustrating minimization.

3.1.1 Newton method

This method is based on the Taylor series expansion. First, let us assume that the point $\mathbf{d} + \mathbf{s}$ is an optimum design. We approximate $f(\mathbf{d} + \mathbf{s})$ using three-term Taylor series expansion,

$$\hat{f}(\mathbf{d} + \mathbf{s}) = f(\mathbf{d}) + \mathbf{g}^T \mathbf{s} + \frac{1}{2} \mathbf{s}^T \mathbf{H} \mathbf{s}, \quad (3.2)$$

where \hat{f} is an approximate of f , $\mathbf{g} = \nabla f(\mathbf{d})$ is a gradient and $\mathbf{H} = \nabla^2 f(\mathbf{d})$ is a Hessian. If

$\hat{f}(\mathbf{d} + \mathbf{s})$ is minimized then $\frac{d\hat{f}(\mathbf{d} + \mathbf{s})}{ds} = 0$, so we differentiate Eq. 3.2 with respect to \mathbf{s}

and obtain

$$\mathbf{H} \mathbf{s} = -\mathbf{g}. \quad (3.3)$$

We can then solve Eq. 3.3 for vector \mathbf{s} and use it in Eq. 3.1. Usually some modifications are required to ensure the convergence or to reduce the number of samples, which is required to estimate the gradient and Hessian. Those modifications are truncated Newton methods, quasi-Newton Methods, etc.

3.1.2 Steepest descent method

This method can be best described with Fig. 3.1. To minimize an objective function, the design is moved in the direction opposite to the gradient.

$$\mathbf{s} = - \frac{\mathbf{g}}{|\mathbf{g}|} \quad (3.4)$$

When use in Eq. 3.1, α is about the same as the search radius, R , that is used to estimate the gradient (this is explained in 3.1.3).

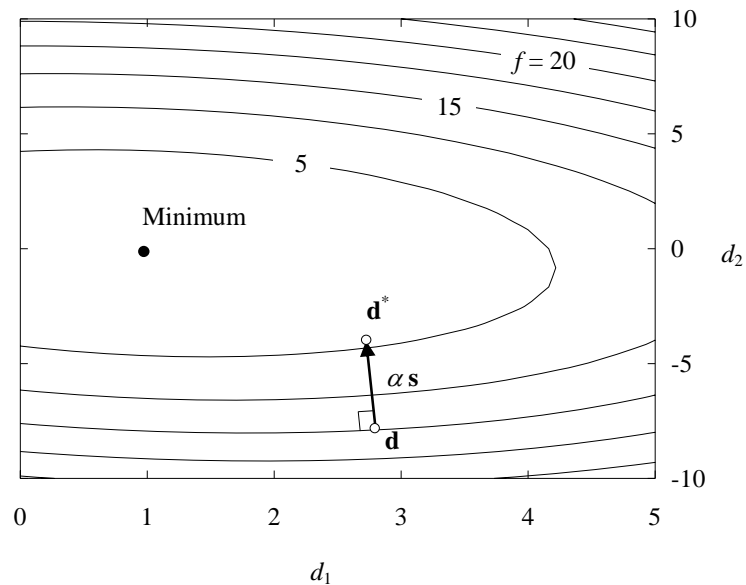


Figure 3.1 Graphical representation of steepest descent method for $n = 2$.

3.1.3 Design of experiments method

Design of experiments (DOE) is part of a collection of statistical and mathematical techniques called response surface methodology (Myers and Montgomery, 1995). The idea is that by systematically sampling the design space one can build a mathematical model called *response surface* (or response function) to approximate the behavior of the objective function. Once the response function is built an estimate of gradient $\hat{\mathbf{g}}$ (and Hessian $\hat{\mathbf{H}}$, if applicable) can be computed and used instead of the exact gradient in the optimization process. Several techniques are available depending on what the users want from the model. The following are some of the techniques.

Central difference

This method use a simple central difference pattern shown in Fig. 3.2 ($n = 2$) and Fig. 3.4a ($n = 3$) to estimate a gradient and diagonal components of a Hessian without an intention to fit a response function.

$$\hat{g}_i = \frac{f_i^+ - f_i^-}{2\Delta d_i} \quad \text{and} \quad \hat{H}_{ii} = \frac{f_i^+ - 2f + f_i^-}{\Delta d_i^2} \quad \text{where } f = f(\mathbf{d}), \quad f_i^+ = f(d_1, d_2, \dots, d_i + \Delta d_i, \dots, d_n),$$

$f_i^- = f(d_1, d_2, \dots, d_i - \Delta d_i, \dots, d_n)$ and Δd_i 's are step sizes. The search radius, R , is the same as the step size or equal to 1 if the design space is coded as shown in Fig. 3.2b.

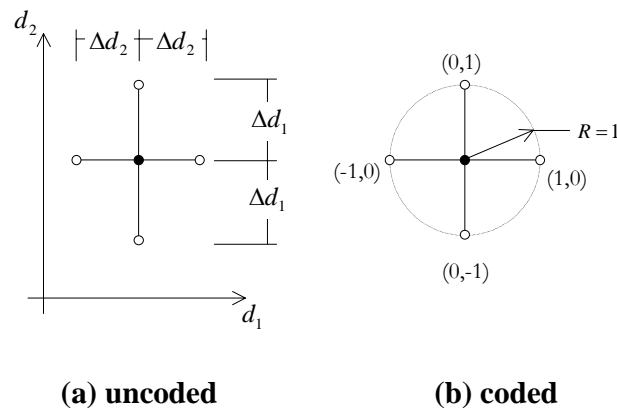


Figure 3.2 Finite difference pattern for $n = 2$.

Two level factorial design (2^n)

The method is briefly described here, with a detailed description given in Box et al. (1979). Samples are selected on vertices of a hypercube (shown in Fig. 3.3 for $n = 2$ and Fig. 3.4b for $n = 3$), which makes a number of samples 2^n . Although the center point is not required as a part of the samples, in an optimization process the value of the objective function at the center point must also be known. This makes the total number of

samples $2^n + 1$. The primary use of this design is to find main effects and cross-effects of design variables on an objective function by fitting a multi linear response function.

A two-dimensional case ($n = 2$) in Fig. 3.3 will be used to demonstrate the process. A step size is specified for each design variable d_i denoted as Δd_i . These are then used to obtain a coded design point \mathbf{D} . Each design variable is coded by $D_i = \frac{d_i - d_i^0}{\Delta d_i}$ where the super script zero denotes the initial value (the center point in Fig. 3.3a and b) so that $D_i^0 = 0$ and a coded step sizes equal unity. Experiments (direct solutions for the objective function) are conducted on four sample points (the four vertices in Fig. 3.3a and b). From the geometry of the search shown in Fig. 3.3b, the radius of the search in coded form is $R = \sqrt{n}$.

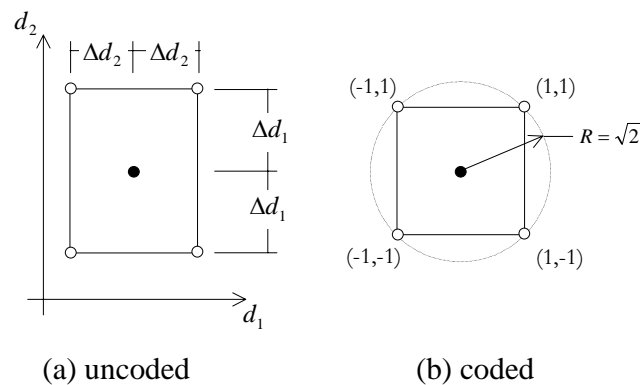


Figure 3.3 Two-level DOE search pattern for $n = 2$.

Once the experiments are completed, one can build an approximate mathematical model from this data. For small Δd_i 's, $\hat{f}(\mathbf{D})$, an estimate of an objective function $f(\mathbf{d})$, can be created as a multi-linear function,

$$\begin{aligned}
\hat{f}(\mathbf{D}) = & c_1 + c_2 D_1 + c_3 D_2 + c_4 D_3 + \dots + c_{n+1} D_n \\
& + c_{n+2} D_1 D_2 + c_{n+3} D_1 D_3 + c_{n+4} D_1 D_4 + \dots + c_{\dots} D_{n-1} D_n \\
& \vdots \\
& + c_k D_1 D_2 D_3 \dots D_n.
\end{aligned} \tag{3.5}$$

Here, $k = 2^n$.

For the case of $n = 2$, the multi linear function in Eq. 3.5 becomes

$$\hat{f}(\mathbf{D}) = c_1 + c_2 D_1 + c_3 D_2 + c_4 D_1 D_2.$$

A matrix equation can be set up to solve for the coefficients c_i 's as the following.

$$\mathbf{E} \cdot \mathbf{c} = \mathbf{f} \tag{3.6}$$

$$\text{where } \mathbf{E} = \begin{array}{c} \begin{array}{cccc} & (D_1) & (D_2) & (D_1 D_2) \\ & | & | & | \\ \begin{bmatrix} 1 & 1 & 1 & 1 \\ 1 & 1 & -1 & -1 \\ 1 & -1 & 1 & -1 \\ 1 & -1 & -1 & 1 \end{bmatrix} & & & \end{array} \end{array} \text{ represents the full factorial combinations of the design}$$

$$\text{variables, } \mathbf{c} = \begin{bmatrix} c_1 \\ c_2 \\ c_3 \\ c_4 \end{bmatrix} \text{ and } \mathbf{f} = \begin{bmatrix} f_1 \\ f_2 \\ f_3 \\ f_4 \end{bmatrix}.$$

By using Yate's algorithm in Eq. 3.7 (described in Box et al., 1979), the coefficients c_i 's can be easily obtained without inverting matrix \mathbf{E} .

$$c_i = \frac{1}{2^n} \sum_{j=1}^{2^n} E_{ji} f_j \quad (3.7)$$

Once the model is built a gradient at point \mathbf{D}^0 can be obtained by differentiating the model. Because of the coding, values of the coded design variables are zero at the initial point and this causes the gradient in coded form to be $\{c_2, c_3, \dots, c_{n+1}\}$. After decoding, the actual gradient can be estimated as $\hat{\mathbf{g}} = \left\{ \frac{c_2}{\Delta d_1}, \frac{c_3}{\Delta d_2}, \dots, \frac{c_{n+1}}{\Delta d_n} \right\}$.

Composite Designs

To fit a second order response function (Eq. 3.8) for n design variables at least n_s

$= \frac{n(n-1)}{2} + 2n + 1$ samples are needed.

$$\begin{aligned} \hat{f}(\mathbf{d}) = & c_1 + c_2 d_1 + c_3 d_2 + \dots + c_{n+1} d_n \\ & + c_{n+2} d_1^2 + c_{n+3} d_2^2 + \dots + c_{2n+1} d_n^2 \\ & + c_{2n+2} d_1 d_2 + c_{2n+3} d_1 d_3 + \dots + c_{n_s} d_{n-1} d_n \end{aligned} \quad (3.8)$$

DOE techniques that use exactly n_s samples are called saturated designs. Saturated designs are not preferred mainly because they cannot handle “noise” (here noise refers to non-smoothness in the response surface such as that caused by truncation errors during the computation of an objective function). Composite designs are near saturated methods that use close to (but no less than) n_s samples to fit a response function and the excess samples help in smoothing out the effect of noise. Some of these methods are central composite design-CCD (Box and Wilson, 1951), Box-Behnken Design-BBD (Box and

Behnken, 1960) and small composite design-SCD. Figure 3.4 shows a comparison of sampling patterns for different kinds of DOE techniques.

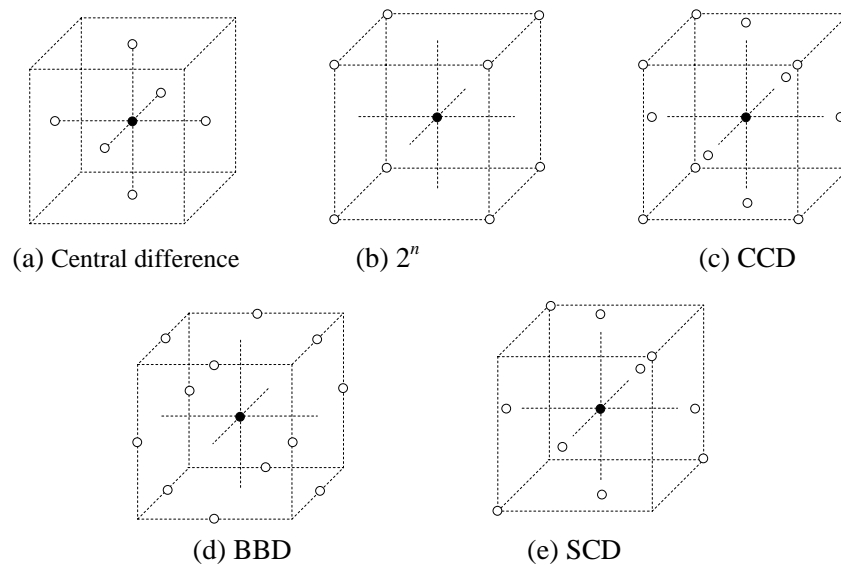


Figure 3.4 Sampling pattern of different design experiments for $n = 3$.

BBD has a comparable number of samples to CCD but it provides relatively poor fitting at the corners area (vertices of the cube). CCD combines central difference with two-level factorial design to produce the total of $n_{\text{ccd}} = 2^n + 2n + 1$ samples, which provides excellent fitting, but for large n , it becomes too expensive. SCD uses half-factorial (2^{n-1}) and central difference, which requires $2^{n-1} + 2n + 1$, is an alternative that produces a second order response function. Detail of response function fittings can be found in Appendix A where a matrix equation is set to solve for the values of coefficients, c_i by the least square method. Once the coefficients are computed, the gradient and Hessian can be estimated accordingly. Details of the composite designs and other DOE techniques can be found in Myers and Montgomery (1995)

3.1.4 Comparison of single objective optimization techniques

To select the right technique it is required to consider the following issues: (a) numbers of direct solutions required, (b) degrees of freedom, (c) efficiency and (d) nature of the objective function.

For our applications, the geometry of the parts can be represented with a few control points using NURBS. After geometric constraints are applied, the degrees of freedom usually lie between 2 and 5. Figure 3.5 compares numbers of samples (one sample is one direct solution) used in different DOE techniques for one iteration. SCD and 2^n factorial use comparable numbers of samples while central difference use the least. But as far as the total numbers of direct solutions are concerned all the techniques are quite comparable since central difference may require more iterations to converge than the other two techniques.

The nature of the objective function is the prime issue that determines the choice of the optimization techniques. In this thesis, objective functions are evaluated by solving differential equations. The solvers themselves have unavoidable truncation errors and errors due to approximations. Those errors are then built into the objective function and so it can be considered that the objective functions come with certain amount of “noise”. The existence of noise makes it preferable to use low order model. For this reason we choose steepest descent method with variable step size for the optimization process in Chapter 4. The details of the process are described in Section 4.1. Primarily, two-level

factorial design is used for gradient approximation and in cases of large n we use central difference method.

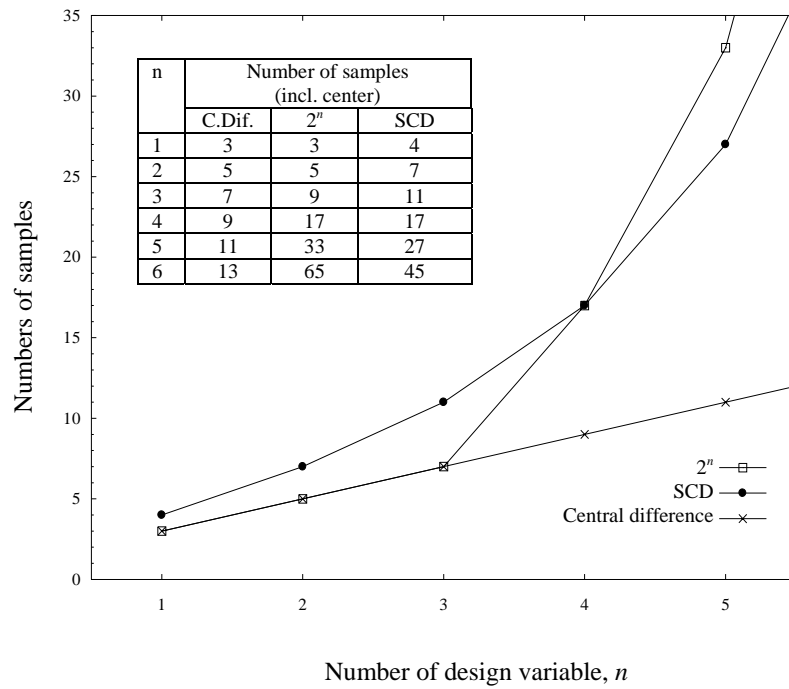


Figure 3.5 Comparison of numbers of samples used by different DOE techniques.

3.2 Multicriteria optimization

In case of a multicriteria optimization problem, one approach to solve the problem is to reduce the complexity of the problem so that the techniques for single-objective can be utilized. Solution techniques base on this approach result in a single solution. Another approach is to retain multiple objectives and try to find a set of possible optimum solutions. The following are some well-known solution techniques.

3.2.1 Weight objectives

This is the most primitive method; the idea being to assign different weights or priorities, to different objectives in forms of coefficients, w_i . The new objective function, $f(\mathbf{d})$, is then a weighted-sum of all the objectives as shown in Eq. 3.9.

$$f(\mathbf{d}) = \sum_{i=1}^m w_i f_i \quad (3.9)$$

The coefficient w_i are usually scaled to satisfy Eq. 3.10.

$$\sum_{i=1}^m w_i = 1 \quad (3.10)$$

3.2.2 Min-max method

This method is best described by the following formulation. First we set up target or ideal values f_i^* for all objective functions. Next, re-scale each objective function f_i using f_i^* as a reference.

$$z_i(\mathbf{d}) = \frac{f_i(\mathbf{d}) - f_i^*}{f_i^*}, \quad i = 1, 2, 3, \dots, m \quad (3.11)$$

Finally, a new objective function is obtained from Eq. 3.12.

$$f(\mathbf{d}) = \max_{i=1,2,3,\dots,m} z_i(\mathbf{d}) \quad (3.12)$$

And a new single-objective optimization problem is

$$\text{Minimize } f(\mathbf{d}).$$

See Hook and Jeeves (1961) for more detail.

3.2.3 Goal programming

With this method, quantitative goals are set to all objectives as constraints. Priorities are assigned to all the objectives. The optimization process is performed on the highest priority objective first with the constraints set. Then the process is repeated for lower priority objectives with an additional constraint that the optimum values of the higher priority objectives must also be met. The process goes all the way down to the least priority objective. More detail can be found in Ignizio (1976).

3.2.4 Global criteria method

In global criteria method (GCM) (Hwang and Masud, 1979), the new objective function is taken to be a measurement of *closeness* between points formed by the value of objective functions and the target or ideal value the objective functions. Figure 3.6 shows a graphical representation of this method, where two objective functions f_1 and f_2 are minimized. Each point represents a performance of one design. The closed curve shown in Fig. 3.6 bounds the region of feasible solutions. Point $\mathbf{F}^* = (f_1^*, f_2^*)$ is an ideal solution. With this method point a , which is closest to \mathbf{F}^* , is the optimum solution. The formulation for the new objective function $f(\mathbf{d})$ is given in Eq. 3.13.

$$f(\mathbf{d}) = \left[\sum_{i=1}^m \left(\frac{f_i(\mathbf{d}) - f_i^*}{f_i^*} \right)^p \right]^{\frac{1}{p}} \quad (3.13)$$

When $p = 2$, f is a measure of distance but other real values also can be used.

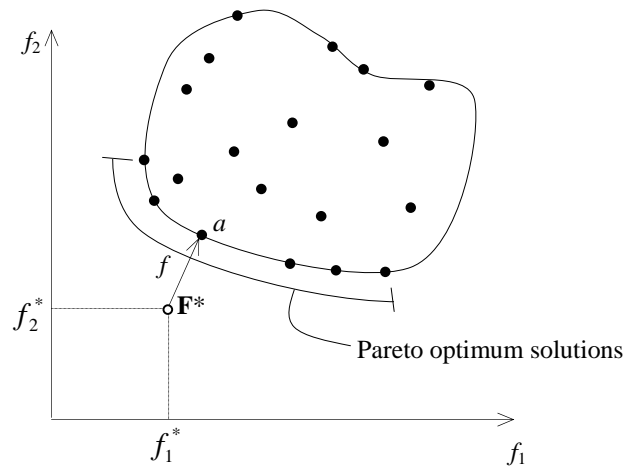


Figure 3.6 Graphical representation of GCM. (Pareto optimum solutions is explained in 3.2.5).

3.2.5 Parameter space investigation method

Parameter space investigation or PSI method is proposed by Statnikov and Matusov (1995). This method is used when there are not enough constraints or preference information to solve the problem by the methods described in 3.2.1 to 3.2.4. It requires that designers first generate a set of trial designs covering the entire design space. Then they solve for objective functions and analyze the results and determine suitable constraints on objective functions. With the constraints a feasible region is set up as the last step in a decision making process to choose “Pareto optimum solutions” (Pareto, 1906), which is a set of possible-optimum solutions that compromise all objectives as shown in Fig. 3.6.

Chapter 4

Optimum Geometric Design of Freeform

Mechanical Parts

Earlier work in optimum design of fluid flow devices provided a reference point for the present effort. The Navier-Stokes equations are a set of nonlinear partial differential equations that are elliptic in space for steady, incompressible flow. Using ideas of variational calculus and optimal control it is possible to derive adjoint equations, the solution to which can provide the direction and magnitude in shape change that can ensure improvement in a specified objective function. A comprehensive review of such and other techniques is provided by Pironneau (1984) and Labrujere and Slooff (1993). Using the ideas of Pironneau, optimum laminar flow diffusers were considered by Cabuk and Modi (1992). Similar ideas were also used in Huan and Modi (1996) for design of airfoils for minimum drag. These studies are, however, limited in the choice of objective functions, choice of boundary conditions and geometry constraints. Consequently, in spite of their computational efficiency, their applicability to practical problems is limited.

One can also possibly use derivative-free methods, treat the solver as a black box, and use a simplex search or genetic algorithm to carry out the optimization. But the high computational cost associated with each direct solution of some non-linear problems such as fluid flow problems makes such an approach impractical.

The present study seeks a generic optimization algorithm that is independent of the precise governing equation, boundary conditions and geometric constraints. Towards this goal a pattern search method based on the design of experiments (DOE) techniques is utilized in the optimizer to determine the derivative information. These ideas have also been explored for a structural optimization problem by Zagajac (1998).

To achieve our goal, the representation of geometry should allow the design space to be explored by as few parameters as possible in order to minimize computational effort. It would also be desirable for this representation to be compatible with CAD tools. NURBS provide an economic way to describe a shape. With a few control points, the shape of the curve (the idea can also be extended to 3 dimensional surfaces) can be controlled. This allows the development of an approximate mathematical model of the relationship between the objective function and the control point locations. The goal of shape optimization is to find the locations of the control points that correspond to the optimum shape. In Fig. 4.1, the optimizer performs optimization on the control point locations and uses the geometrical processor to convert the control point locations to the boundary points on the NURBS curves. The approach treats the solver as a black box. As

shown in Fig. 4.1, inputs to the black box are the geometry together with material properties and boundary conditions. Output from the black box is the solution field.

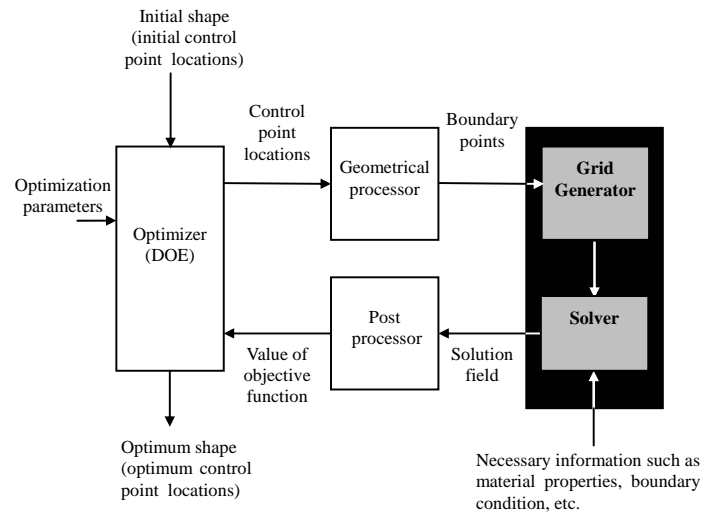


Figure 4.1 Overview of the optimization process.

In Section 4.1 optimization procedures are formed by combining two-level DOE technique with steepest descent method. The optimizer is utilized with a freeform geometry representation to form the shape optimization algorithm described in Section 4.2. In Section 4.3 the optimization algorithm is first verified using an idealized problem of designing a ninety-degree bend in two-dimensional potential flow. Then the problems of the design of plane and axisymmetric two-dimensional diffusers in laminar flow are considered followed by a solid mechanics problem of designing a minimum weight torque arm. These results are discussed in Section 4.4

4.1 Optimization procedures

We use an iterative approach to improve from an initial design \mathbf{d}^0 to the new design \mathbf{d}^1 such that the objective function $f(\mathbf{d}^1)$ is better (higher for minimization; lower for maximization) than $f(\mathbf{d}^0)$. DOE technique is used to conduct a pattern search as well as to estimate the gradient. Eq. 3.1 can be re-written to use specifically with the steepest descent method as

$$\mathbf{d}^* = \mathbf{d}^0 \pm q \cdot \Delta d \cdot \hat{\mathbf{g}} \quad (4.1)$$

(plus for maximization and minus for minimization),

where \mathbf{d}^* is the tentative design point for which we expect $f(\mathbf{d}^*)$ to be an improvement over $f(\mathbf{d}^0)$; q is an adjustment factor, which should not be much larger than the coded radius of the search. Note that the coded radius of the search is equal to 1 for central difference and \sqrt{n} for two-level DOE as described in 3.1.3. In the above, Δd is a step size and $\hat{\mathbf{g}}$ is the estimated gradient.

The tentative point \mathbf{d}^* is not yet the point \mathbf{d}^1 for the next iteration. Assume that the optimization problem is that of maximizing the objective function. In order to determine the new point we must consider the following three cases:

Case 1. $f(\mathbf{d}^*)$ is higher than the objective function at the initial point and all the sample points. Then the search continues along the steepest direction until there is no further improvement of the objective function. The next iteration begins at this point.

Case 2. The best design is found during the DOE process. Then that design is chosen as the initial point for the next iteration.

Case 3. No improvement is found. In this case a smaller step size, specifically half the initial size, is used and the whole process is repeated until the step size is smaller than some critical value. The search also terminates when the size of the gradient becomes close to zero or when the number of iterations reaches a predetermined value.

The search pattern for maximizing $f(\mathbf{d})$ during one such iteration process for $n = 2$ is shown in Fig. 4.4 where the first and the third iterations correspond to case 1, the second iteration to case 2 and the fourth, fifth and the sixth iterations to case 3.

The use of lower order methods for DOE allows us to limit a number of samples to a manageable level while allowing an estimate of the local gradient with sufficient accuracy. As described in case 3, when there is no improvement in the search, it is logical to assume that the optimum point lies within the search radius so the optimizer reduces the step size. This allows the optimizer to converge to a local optimum without having to use a higher order scheme. Accuracy of the optimum solution corresponds to the smallest step size used.

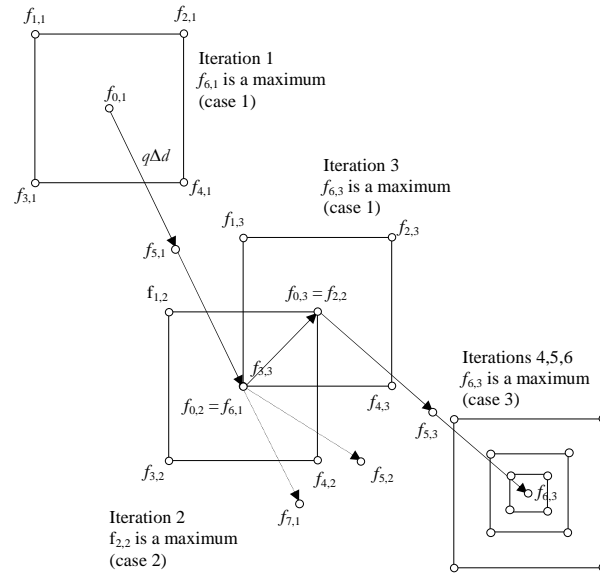


Figure 4.2 Search pattern in a maximization problem with $n = 2$ using two-level DOE.

4.2 Algorithm for geometric optimization

In Fig. 4.1, the optimization is performed on the control point locations and a geometrical processor is used to convert the control point locations to boundary points on a curve. The approach treats the solver as a black box. As shown in Fig. 4.1, inputs to the black box are geometry of the parts, material properties and boundary conditions. Output from the black box is the solution of the objective function. The optimization procedure is described next.

Step 1. Represent the initial boundary of interest with a Bezier curve (or a B-spline curve) described in Chapter 2 using m control points. The initial optimization parameters are also specified at this step. These are: the initial step size, the smallest step size, the maximum number of iterations and the maximum number of control points. Value of an objective function f depends on the locations of the control points.

$$f = f(\mathbf{P}_0, \mathbf{P}_1, \mathbf{P}_2, \dots, \mathbf{P}_m)$$

Step 2. Apply geometrical constraints to the control points.

These constraints may consist of

- a) fixing the end point of the curve
- b) fixing either x - or y -coordinates of all the control points
- c) fixing the slope at one of the end points of the curve.

When this is done, the total number of variables is reduced. The remaining coordinates are considered to be the n design variables (degrees of freedom = n) and together they form the vector of design variable \mathbf{d} .

Step 3. Use the optimization procedures described in Section 4.1 to find a new design point given by the values of the n variables in order to improve the objective function. The new values of the n variables at each iteration define the new locations of the control points. These control points describe the new shape of the curve and hence the boundary points on the new curve. Note that the black-box solver (consisting of the grid generator and the flow solver) is used to compute the values of the objective function for any given

set of boundary points on the curve. Each implementation of step 3 is considered one design iteration. Note that each design iteration consists of several direct solutions.

Step 4. Check whether the following criteria are satisfied.

- a) the step size is smaller than prescribed smallest critical size
- b) there is no improvement in the objective function for two consecutive iterations
- c) the prescribed maximum number of iterations has been reached.
- d) Size of the gradient vector is smaller than the prescribed value.

If none of these conditions is met then return to step 3. If any of these conditions is met, then go to step 5.

Step 5. Check if any of the following two conditions is met.

- a) There has been no improvement in the objective function between the current shape represented by m control point and the shape obtained using $m + 1$ control points
- b) The prescribed maximum number of control point is reached.

If either of these conditions is met then stop the entire optimization process. If not, then increase the number of control points. For a Bezier curve, use of degree elevation leads to the same shape. For a B-spline curve, addition of one more control point using degree elevation algorithm leads to minor change in shape. Repeat the optimization process by returning to step 2.

4.3 Example problems

4.3.1 Ninety-degree bend in potential flow

An idealized problem of a two-dimensional potential flow through a ninety-degree bend is considered. This problem does not account for the effects of viscosity, nor does it allow three-dimensional behavior. However it provides a test bed for validating the concepts of optimization and robust design. With a potential flow assumption, the governing equations for fluid flow are reduced to the Laplace equation. A boundary element method (Liggett and Lui, 1983) is used for flow solution after discretizing the boundary into 76 segments as shown in Fig. 4.3.

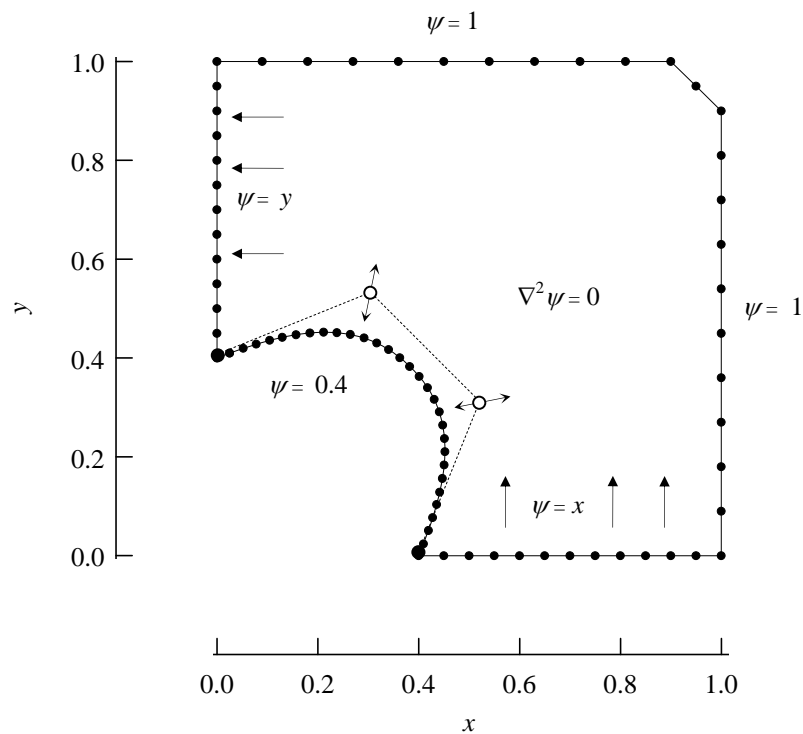


Figure 4.3 Ninety-degree bend in potential flow.

The objective is to find the shape of the inner wall that minimizes the transverse velocity components at the inlet and outlet sections. Hence the objective is to minimize the sum of the modulus of the transverse velocity components at the inlet and outlet boundaries and is given by

$$\min f, \text{ where } f = \sum_i \left| \frac{d\psi_i}{d\bar{n}} \right|, i = \text{inlet and outlet boundary nodes.}$$

Since a complex optimum geometry is expected, cubic B-spline curves are chosen to represent the geometry of the inner wall. A central difference pattern is used in the optimization to reduce number of direct solution. The initial step size is 0.05 and the minimum step size is 0.01. During the optimization process the number of control points is increased as needed in order to handle more complex geometry of the optimum inner wall shape. Initial number of control points is five; two are fixed at both ends of the curve so there are three control points that have to be adjusted. Both x - and y -coordinates of the free control points are free to move but the movement will be constrained in the normal direction only in order to reduce number of design variables. This makes the initial degrees of freedom to be three instead of six. Figure 4.4 shows the history of convergence. An optimum design is obtained at the fifteenth design iteration. The total number of direct solutions is 172. The optimum design and some intermediate designs are shown in Fig. 4.5. The optimum design was represented with seven control points (degrees of freedom = 5). The optimum design has an objective function value of 0.3 compared to 2.05 of the initial design. In Fig. 4.6, the optimum geometry is compared with the result from adjoint method by Cabuk and Modi (1990). A close agreement is observed.

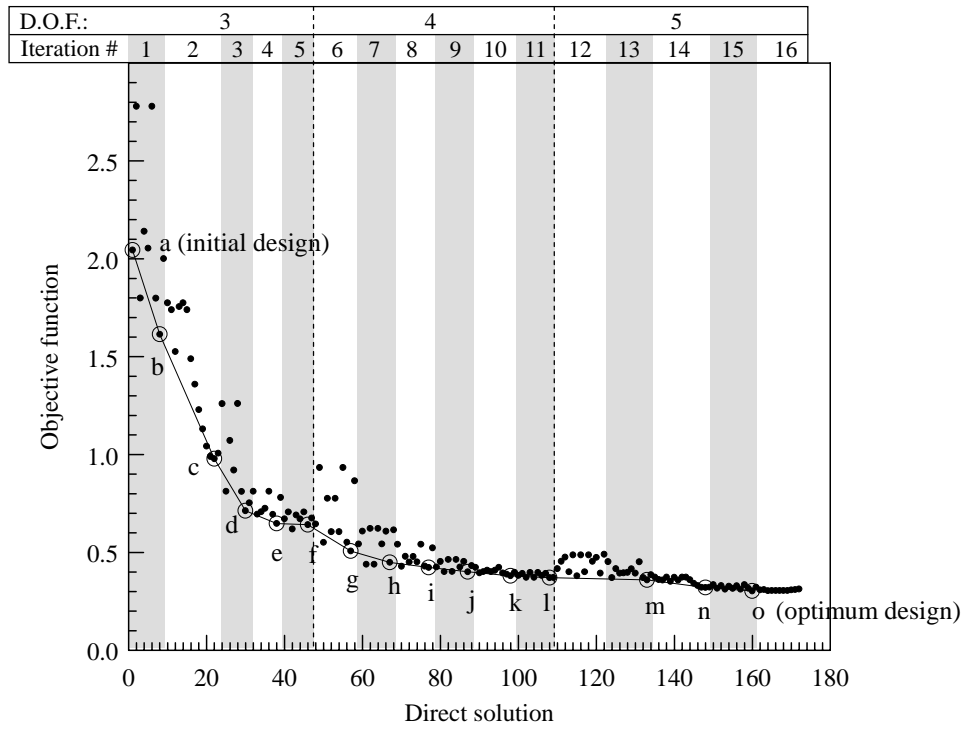


Figure 4.4 History of convergence in design optimization of ninety-degree bend.

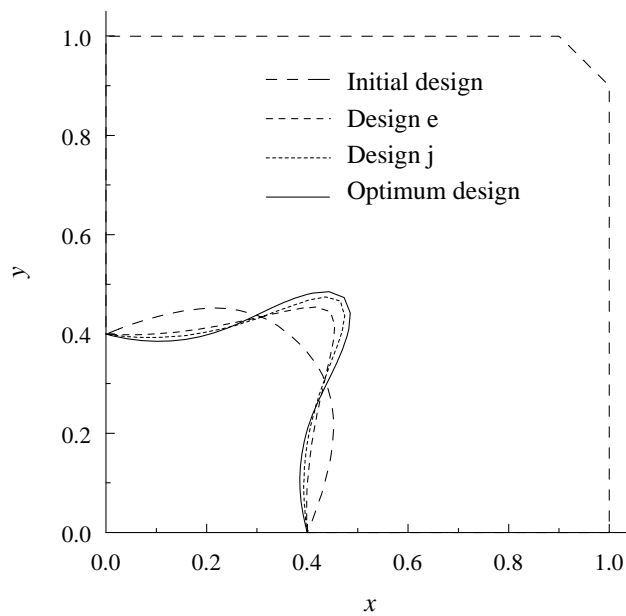


Figure 4.5 Geometry of ninety-degree bend at different design iterations.

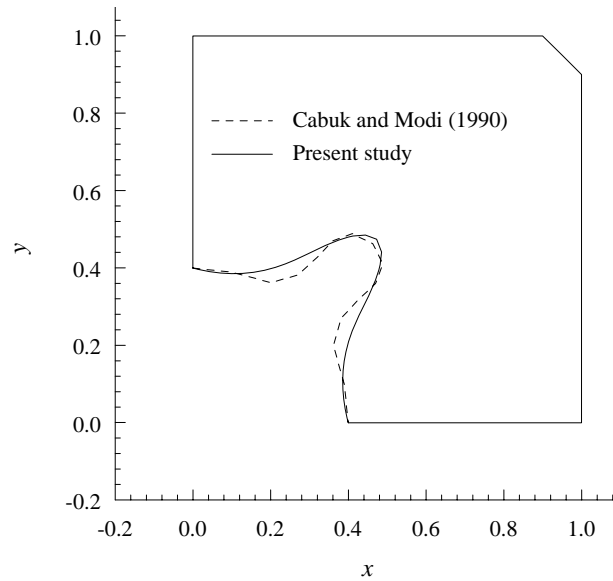


Figure 4.6 Comparison between the optimum geometry from this study and from Cabuk and Modi (1990).

4.3.2 Plane symmetric diffuser in laminar flow

The second problem examined was that of determining the shape of a plane symmetric diffuser that leads to maximum pressure rise under certain flow, boundary and geometric constraints. The flow is assumed to be steady, laminar and incompressible; governed by the Navier-Stokes equations. Note that unlike the problem in section 4.3.1, the flow is no longer a potential flow and cannot be treated by a boundary element method. Due to symmetry, only the symmetric half of the diffuser is considered and is shown in Fig. 4.7. The diffuser centerline has symmetry boundary conditions and the upper wall is a no-slip wall. A parabolic velocity profile corresponding to a fully developed laminar channel flow is specified at the inlet. The geometric constraints are: prescribed inlet width H , prescribed diffuser length $3H$, constant length inlet and outlet

sections of size $0.75H$ and $6H$ respectively. The objective is to maximize the pressure rise through diffuser. The pressure rise also depends upon the flow rate through the diffuser, characterized by the non-dimensional parameter, Reynolds number $Re = u_i H / \nu$ where ν is the kinematics viscosity of the fluid and u_i is the average inlet velocity. A non-dimensional pressure rise is defined by a pressure coefficient C_p given as,

$$C_p = \frac{p_o - p_i}{\frac{1}{2} \rho u_i^2}, \quad (4.2)$$

where p_o and p_i are the area averaged diffuser outlet and inlet pressures and ρ is the fluid density.

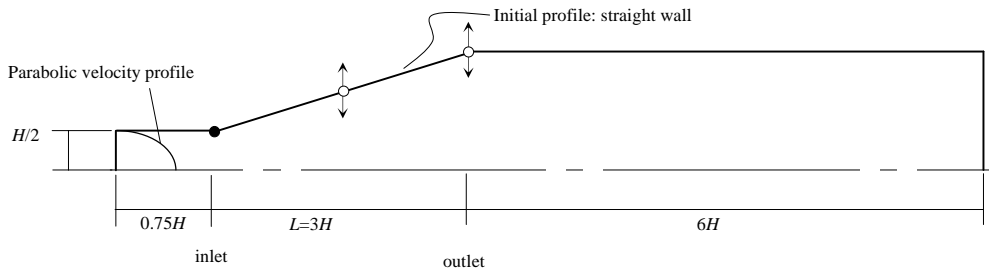


Figure 4.7 Plane symmetric diffuser.

The initial diffuser shape was represented by a Bezier curve with the first control point always kept fixed at the inlet and the x -coordinate of the others kept fixed during the optimization process. The actual control points were successively increased as described in Section 4.2 beginning with 3 points up to a maximum of 6 control points. A laminar fluid flow code, CAFFA by Ferziger and Peric (1996), was modified for use as the flow solver.

Figure 4.8 shows a typical grid of 55×10 that was used for the computation. The CAFFA flow code is a multi-grid flow solver that automatically generates a second finer grid of twice the density in each direction, i.e. 110×20 by interpolating the original 55×10 grid.

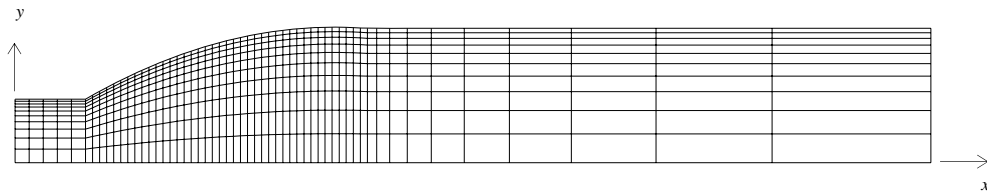


Figure 4.8 Typical grid of 55×10 .

Because of the inherent inability of any flow solver to accurately predict the pressure coefficient with more than two significant figures, the optimization process was terminated when the second significant figure in C_p was no longer altered, although three significant figures were used in computing the steepest direction. The choice of the initial diffuser profile is made in the following fashion. The pressure coefficient for a given Reynolds number is computed for a progressively increasing diffuser area ratio AR (exit width/inlet width) for straight walled diffusers. The pressure coefficient achieves a maximum at some value of AR during this process. The straight wall profile corresponding to this area ratio AR is assumed to be the initial diffuser profile for a given Reynolds number. The improvement in C_p over the C_p value for a straight walled diffuser represents the gain in pressure rise due to shaping of the diffuser with a Bezier curve.

Diffuser shape optimization using ideas described in Section 4.3 is carried out for $Re = 50, 100, 200$ and 400 . The optimized diffuser shapes are shown in Fig. 4.9. Note that only the diffusing portion of the upper wall is shown in Fig. 4.9. The constant width inlet and exit sections are not shown.

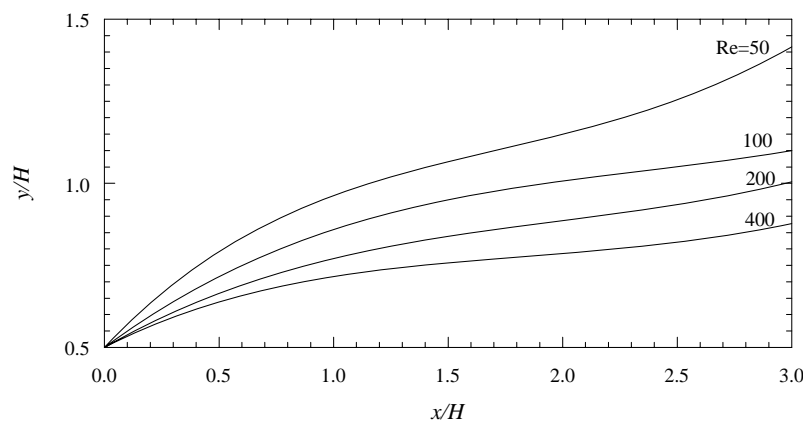


Figure 4.9 Optimum plane diffuser profiles with $L/H = 3$ at $Re = 50, 100, 200$ and 400 .

The case for $Re = 100$ is discussed in further detail. A plot of C_p versus AR for all the direct solutions is shown in Fig. 4.10 in order to describe the optimization process for this particular case. The solid curve represents the straight walled diffusers computed in order to select an initial shape. Each direct solution is shown on the plot as a single point. The dotted lines connect the points corresponding to the optimum shapes obtained at the end of each iteration. From this figure we observe that the optimum diffuser profile at $Re=100$ has a lower area ratio than the best straight walled diffuser and yet produced a larger pressure rise. This is found to be true for all the Reynolds numbers that were examined. Figure 4.11 shows convergence history of C_p . The C_p value of the optimum

shape is 0.45. Compared to the C_p of 0.41 of the initial shape there is a 10% improvement.

The optimum shape obtained in the present study is compared in Fig. 4.12 to the results of Cabuk and Modi (1992) obtained using an adjoint variable method derived using ideas of Pironneau (1974). The close agreement in diffuser profiles obtained with these two different optimization techniques and two different flow solvers lends a degree of confidence to the present computations.

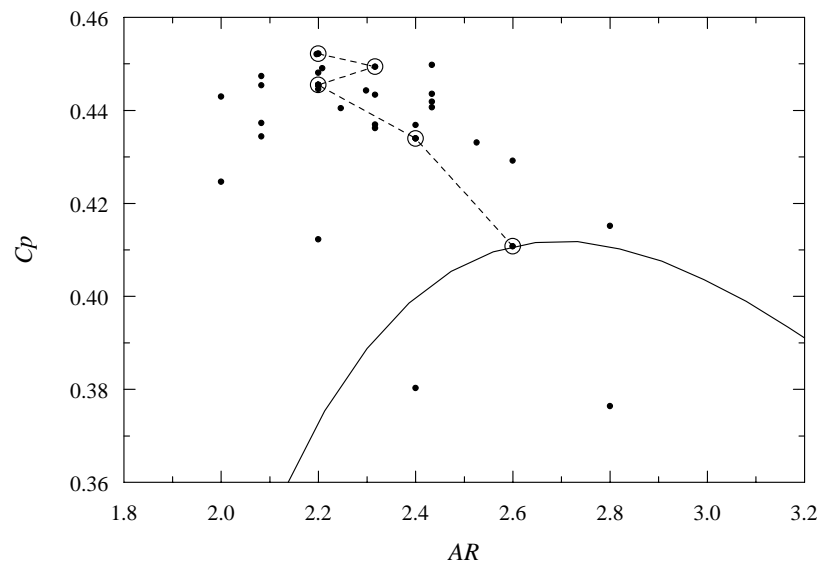


Figure 4.10 Pressure coefficient vs. area ratio for plane symmetric diffusers with $L/H = 3$ at $Re = 100$.

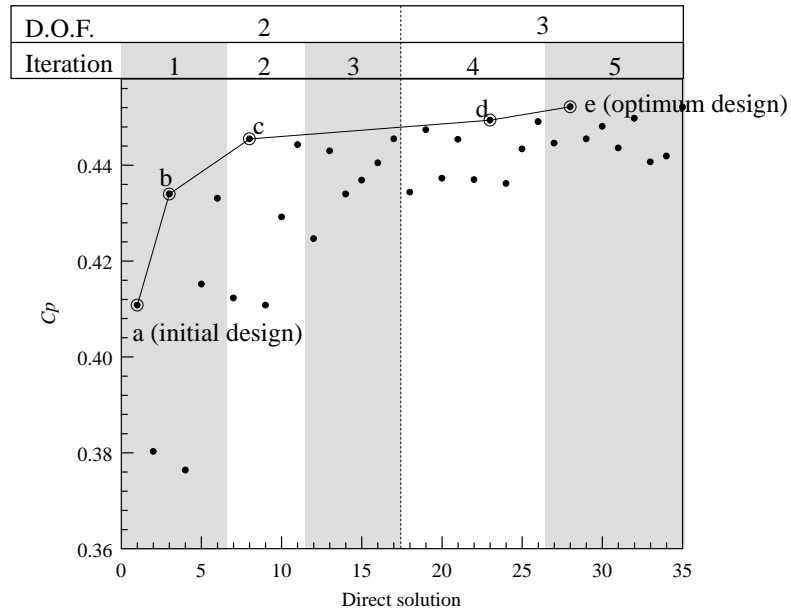


Figure 4.11 History of convergence in design optimization of plane symmetric laminar flow diffuser for the Reynolds number of 100.

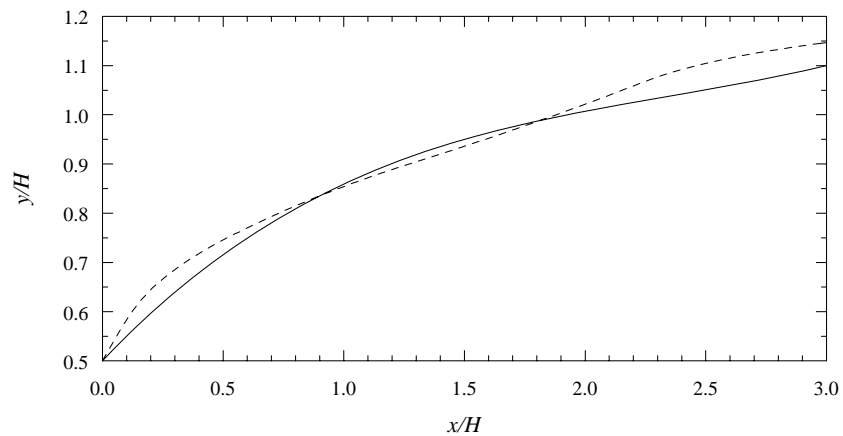


Figure 4.12 Optimum plane diffuser profiles with $L/H = 3$ at $Re = 100$. The dashed line is the result from Cabuk and Modi (1992) for a grid of 31x11 and the solid line is the present result.

4.3.3 Axisymmetric diffuser in laminar flow

The problem of optimizing axisymmetric diffusers for laminar flow is addressed next. The diffuser configuration, flow assumptions, boundary conditions and the geometry constraints are identical to those considered in section 4.3.2 except that now axisymmetric diffusers with inlet diameter D (replacing inlet width H) are used instead of plane diffusers. Once again optimum diffusers for laminar flow Reynolds numbers of 50, 100, 200 and 400 are computed. The final results of the optimization process are shown in the Fig. 4.13. Figure 4.14 shows the convergence of C_p during the optimization process for the case of $Re=100$, 15% improvement in C_p value is observed for the optimum design.

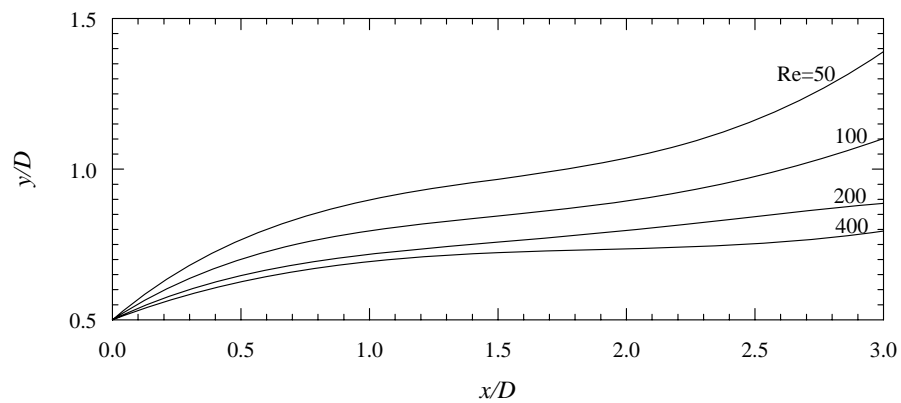


Figure 4.13 Optimum axisymmetric diffuser profiles with $L/D = 3$ at $Re = 50, 100, 200$ and 400 .

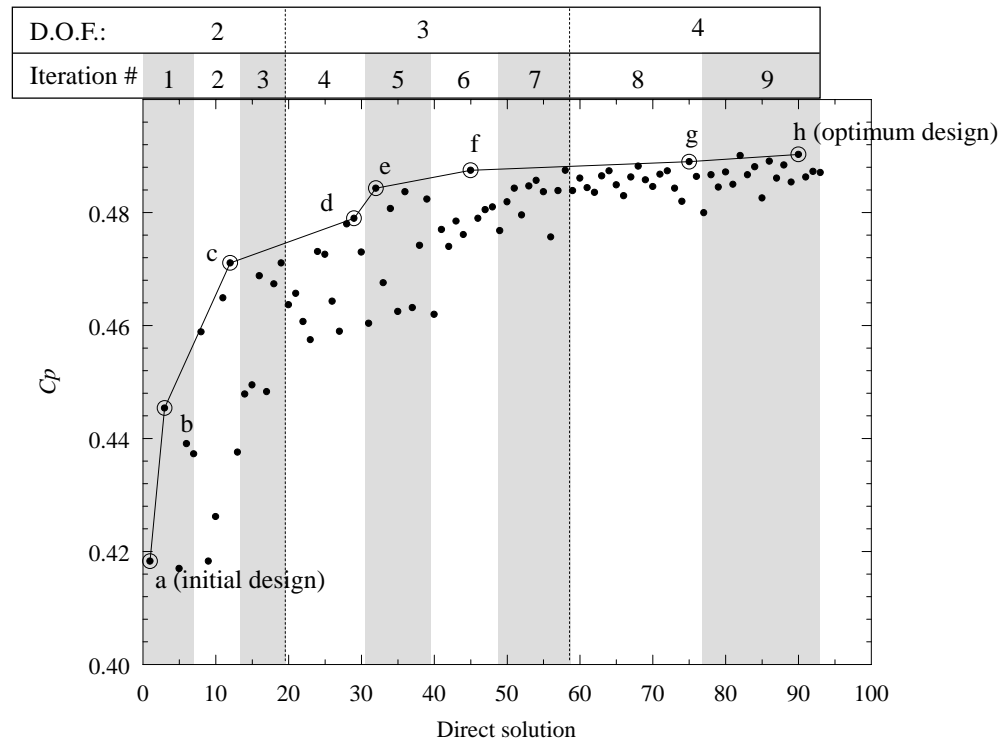


Figure 4.14 The progression of the pressure coefficient with each direct solution during the optimization process of axisymmetric diffusers with $L/D = 3$ at $Re = 100$.

4.3.4 Torque Arm under static load

A problem first introduced by Botkin (1982) where the objective is to minimize the weight w of a torque arm subjected to axial and transverse loads is considered next. Ultimate stress of the material used is $\sigma_u = 972 \text{ MPa}$. With a safety factor of 1.2, the design maximum stress is set to be $\sigma_d = 810 \text{ MPa}$. The overall geometry is shown in Fig. 4.15. The shape of the straight boundary between the two holes is to be optimized. A stress constraint is handled by a discrete penalty function; the objective function is described in Eq. 4.3.

$$f = \begin{cases} \frac{w}{w_0} & \text{if } \sigma_e \leq \sigma_d \\ \frac{w}{w_0} \left(1 + \frac{\sigma_e}{\sigma_d}\right) & \text{if } \sigma_e > \sigma_d \end{cases} \quad (4.3)$$

The thickness of the arm is assumed to be 3 mm; radii of the small and the large holes are taken to be 20 mm and 40 mm respectively. A geometric constraint that the torque arm be symmetric about the x -axis is imposed. A finite element code (linear quadrilateral element) by Betti (1997) is used to solve for the maximum element stress in the 282 elements. The typical mesh for finite element solutions is shown in Fig. 4.16.

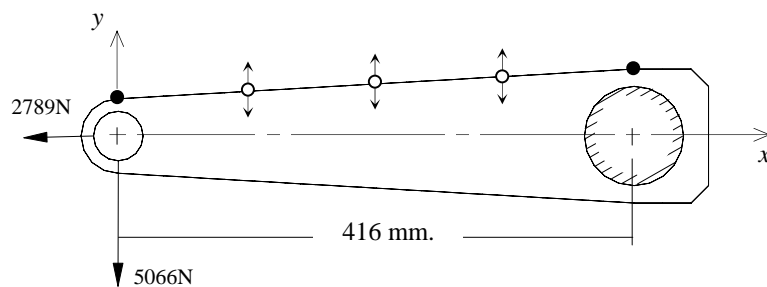


Figure 4.15 Torque arm under static loads.

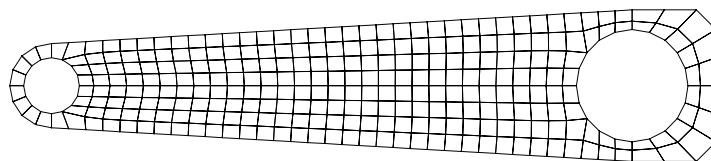


Figure 4.16 Typical quadrilateral mesh.

The shape of the boundary is initially represented by a cubic B-spline curve with five control points (both ends are fixed). The number of control points is increased as

required to handle more complex geometry. Design variables are the y-coordinates of the free control points. The optimization process is carried out using two-level DOE. Figures 4.17a and b show a history of convergence of weight and maximum stress respectively. The optimum design and some intermediate designs are shown in Fig. 4.18. The optimum design is obtained with a six-control point curve. Ninety-two direct solutions were made. The optimum weight is 67% of the initial weight. In Fig. 4.19, the result is compared with the optimum design obtained by Richards (1995) using genetic algorithm. A close agreement is observed.

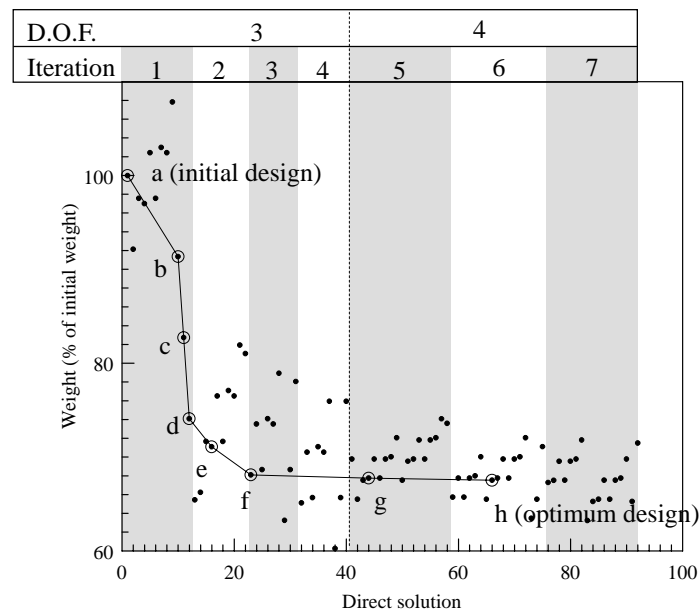


Figure 4.17a History of convergence of the weight of the torque arm.

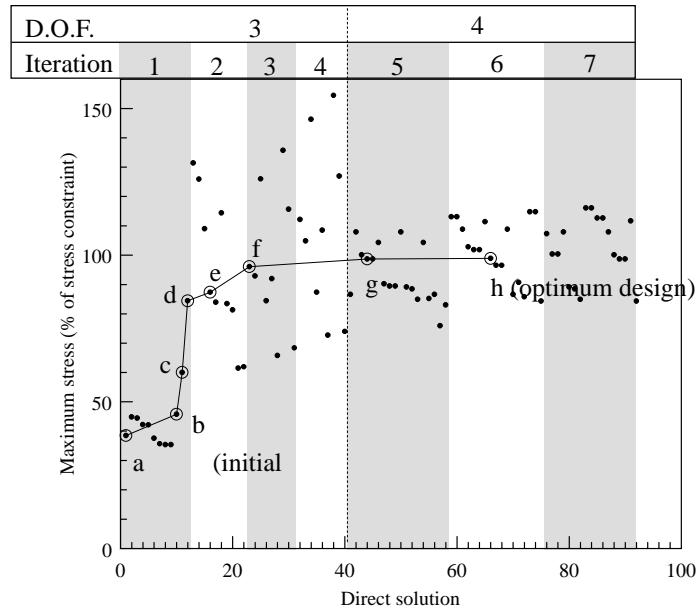


Figure 4.17b History of convergence of maximum stress in the torque arm.

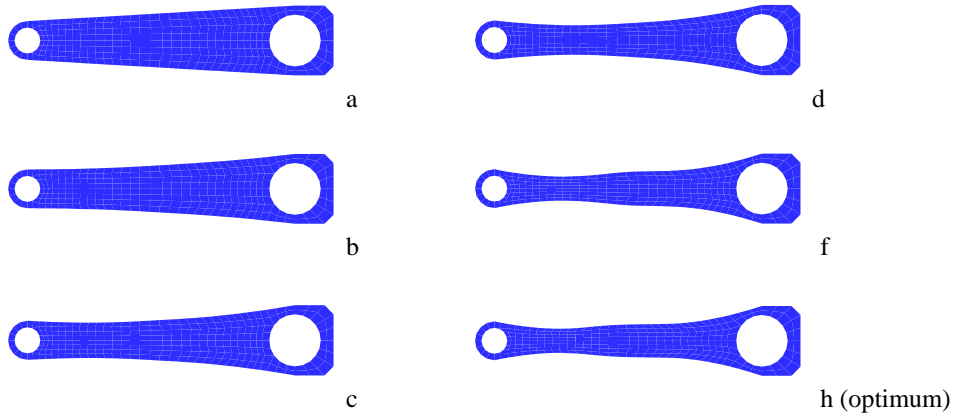


Figure 4.18 Evolution of torque arms geometry.

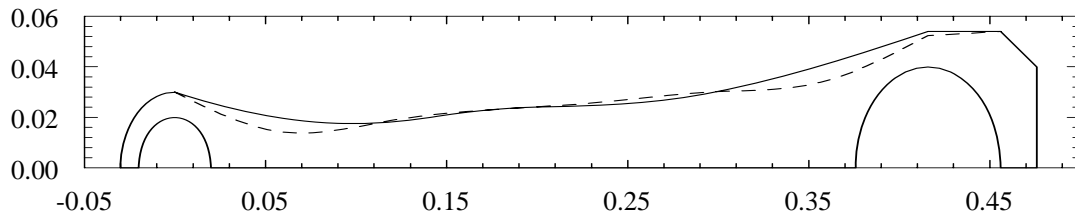


Figure 4.19 Comparison between the torque arm geometry from this study (solid line) and from Richards (1995) (dashed line).

4.4 Discussion

For the potential flow problem of section 4.3.1 we verified that the algorithm was able to achieve the considerably complex optimum shape by a few control points. In section 4.3.2 and 4.3.3 we applied the algorithm to two laminar diffuser problems and the results were also encouraging. Significant improvement in C_p 's for both plane and axisymmetric cases is achieved for all the Reynolds numbers in the study.

Consider the result of the optimization process for the plane symmetric diffuser at $Re = 100$, the maximum C_p obtained from computations is 0.452. Since we expect no more than a two significant figure accuracy from the solver, CAFFA, we consider the maximum to be $C_p = 0.45$ and the intermediate results with $C_p > 0.445$ obtained during the optimization process to correspond to optimum profiles. With this in mind, the optimum region lies above $C_p = 0.445$ as shown in Fig. 4.10. This implies that there is a family of profiles obtained from the optimization process that can be considered optimum. These profiles are shown in Fig. 4.20 corresponding to the points in the optimum region of Fig. 4.21.

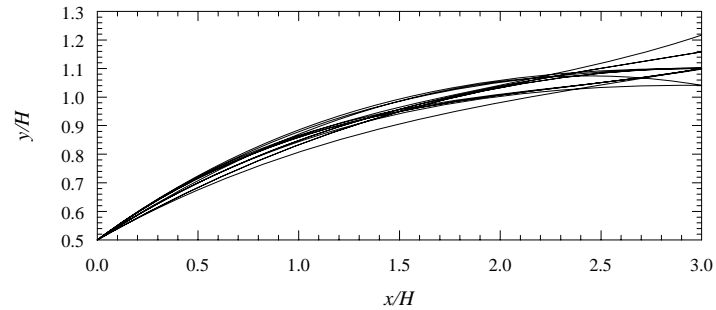


Figure 4.20 Family of optimum plane diffuser profiles with $L/H = 3$ and $Re = 100$.

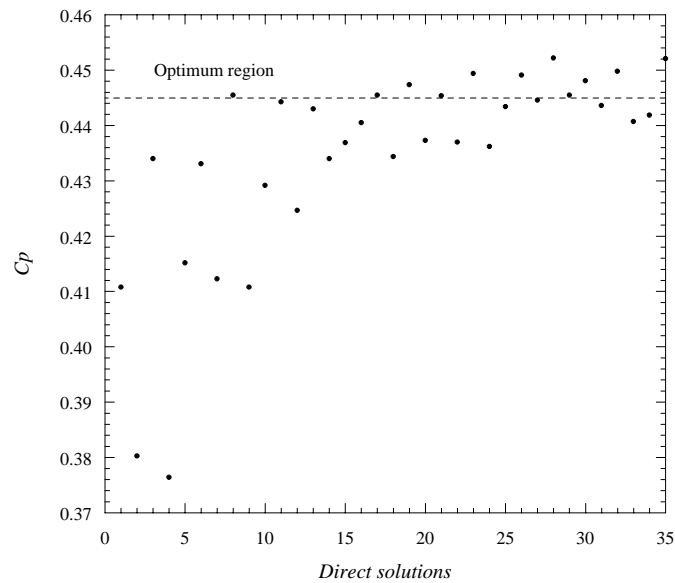


Figure 4.21 The progression of pressure coefficient with each direct solution during the optimization process of plane diffusers with $L/H = 3$ at $Re = 100$. The dashed line represents the lower bound of the optimum region.

In design of minimum weight torque arm, we observe from the stress distribution plot (Fig. 4.22a and b) that the areas around the centerlines of the torque arms have minimal stress levels while the areas along the boundaries have maximum stress levels,

which are consistent with the beam theory. It may be more preferable in some cases to have the torque arm configured with a slot in the middle (see Fig. 4.23) as investigated by Botkin (1986), Zhang and Belegundu (1992) and Wang and Grandhi (1996). In fact a solid-empty approaches (Bendsoe, 1989) should also lead to the optimum solution that has no material in the centerline area. No matter which configuration is used, the optimum torque arm is still subjected to the peak stress close to the constraint value at the boundary as shown in Fig. 4.21. Under this stress condition, any tolerance in the shape may lead to failure. By this reason, we suspect that the optimum torque arm may not be robust. This issue of robustness will be discussed in the next chapter.

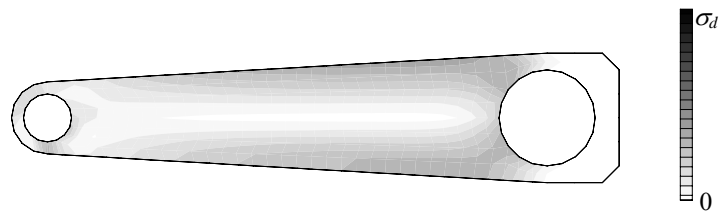


Figure 4.22a Stress distribution in the initial torque arm.

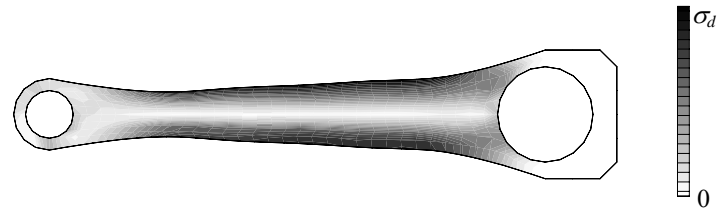


Figure 4.22b Stress distribution in the optimum torque arm.

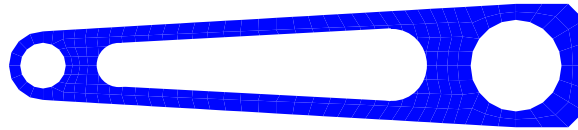


Figure 4.23 Torque arm with slot design.

Chapter 5

Robustness Analysis of Freeform Mechanical Parts

Engineers refer to the stability of designs as the robustness of designs. Simply stated, a robust design is one that delivers roughly the same performance in the presence of inevitable variations in the manufactured instances of a product as well as in its operating conditions. A mathematical abstraction of the notion of robustness is shown in Fig. 5.1. A point p in the space P of product and environmental parameters maps to a point f in the space F of performance indicators. Assuming some mild smoothness of this mapping function, a neighborhood $N_P(p)$ maps to a neighborhood $N_F(f)$. The neighborhoods are shown as shaded regions in Fig. 5.1. A robust design is a point p in P whose finite neighborhood $N_P(p)$ maps to a “small” neighborhood $N_F(f)$. In contrast, an optimum design is a point p in P whose mapping f in F achieves the maximum of the desired performance over F .

Designers seek optimum designs that are also robust. If this is not achievable, then sub-optimal designs that exhibit robustness may be acceptable. But any design, optimal or otherwise, that is not robust is not an acceptable engineering solution. This

opens up several interesting questions. What is the measure of smallness of the neighborhood $N_F(f)$? How can one explore the neighborhood of points in P ? We propose to answer these questions in this chapter and test them on several examples. We make no special assumptions about the mapping function except that we have at our disposal a function evaluator that, given a point p in P , evaluates a point f in F . We use computer simulation to perform this evaluation. We then sample several discrete points in P and probe the neighborhood of each point for robustness.

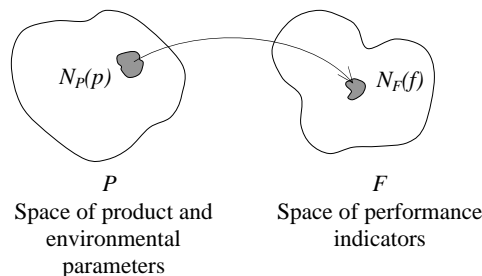


Figure 5.1 A mapping for a mathematical abstraction of robustness in design.

Researchers have adopted a variety of approaches in the area of computational shape optimization of mechanical parts. These include black-box optimization of the previous chapter, adjoint operator or optimal control based methods (Pironneu, 1974, 1984, Cabuk and Modi, 1992) and genetic algorithms (Richards, 1995). With modeling approximation and limited solver accuracy, optimum shapes obtained using computational shape optimization can only be approximate. Moreover, in practice the mechanical parts may be subjected to uncontrollable factors (or noise) such as finite manufacturing tolerances and variations in operating conditions. In order that a chosen design remains close to optimal during practical use, the design must be relatively

insensitive to noise. A design that meets these qualifications will be referred to as a robust design.

Phadke (1989) suggests one way to classify noise by its source as internal noise, external noise and deterioration. Unit-to-unit variation due to manufacturing imperfections such as dimensional tolerances or variations in material properties is internal noise. External noise consists of changes in operating conditions such as temperature, humidity etc. Deterioration refers to changes of the parts from their original state in time due to aging and wear. In this study, the source of noise is not of concern and hence deterioration will be considered as part of internal noise.

To achieve robustness and optimality at the same time may not always be possible in most cases and a compromise must be made. Following Taguchi (1986), the quantity signal-to-noise ratio (*SNR*) is used in robustization. It characterizes the ratio of mean performance to variance of performance under the presence of noise. The larger *SNR* usually leads to the more robust design, however there are some cases where this is not true. An example of a problem one can encounter in using *SNR* can be found in Wilde (1991).

Other than the use of *SNR*, Cagan and Williams (1993) propose a method based on an extension of the Lagrangian and *KKT* conditions of optimality to take into account the measurement of flatness and curvature of the objective function. The method requires the use of second order derivatives and finally human judgement may be required. There

are several other techniques for robust design such as worst case analysis, corner space evaluation, etc. A recent article by Chen and Du (1999) provides a comparison of some of these methods.

In this chapter, a method for robustness analysis is presented based on the black-box approach carried on from the previous chapter. We analyze the effect of noise on the design by using *SNR* together with the simple statistical method of finding mean, standard deviation and probability of failure. The methods are presented in the next section followed by their applications to the example problems from the previous chapter.

5.1 Methodology for robustness testing

Most applications of robust design techniques have been to problems with analytical solutions permitting inexpensive computation. In the present study, we focus on the design of freeform shapes, which involve many design variables and where no prior analytical solution to the relationship between performance and shape is available. Moreover methods such as *worst case analysis* may not be appropriate in our applications since the worst case noise factors are not necessarily the extreme values of the specifications. And due to a large number of design variables and time consuming yet inaccurate iterative direct solution, we cannot afford to use *SNR* as objectives of the designs or the use of Lagrangian based methods. Our approach to the problem is to first perform a numerical shape optimization process to maximize (or minimize) the performance (the process is described in Chapters 3 and 4). Then check for robustness of each iterative design. The approach is shown in Fig. 5.2a and b. Figure 5.2a shows the

shape optimization process and Fig. 5.2b shows the robustness analysis process performing on the iterative designs obtained from the optimization process.

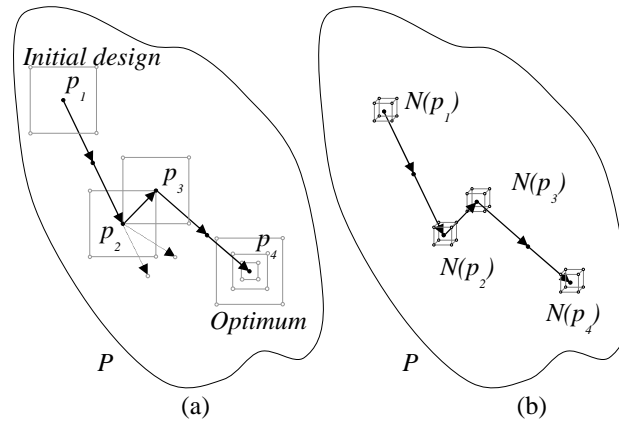


Figure 5.2 (a) Search pattern in the design space P for optimum design, (b) Applying noise to critical points.

The procedure for robustness analysis starts with the generation of neighborhood samples to simulate the effect of noise on each iterative design. Next the objective function of each sample is evaluated. From the samples we compute the values of SNR , mean, standard deviation and probability of failure. The computation of these values and the techniques to generate noise are described next. Subsequently this information can be utilized to identify robust designs.

5.1.1 Noise in freeform geometry

Noise in a freeform geometry can be viewed as changes of shape within a tolerance zone of the size $\pm d$ as shown in Fig. 5.3a. There are infinite numbers of free form shapes in the zone. In our optimization algorithm, the shapes are represented by either Bezier or B-spline curves. The number of control points that define the curve is progressively increased during the optimization process until no further improvement in objective function is achieved. As a result, a design from each successive iteration may be represented with a different number of control points. Since the control points are treated as design variables subject to noise and since the number of neighbors for each design point are given by 2^n factorial (for n free control points), the number of neighbors will be different at each design iteration. The varying number of neighbors make it difficult to compare *SNR*, standard deviations and means obtained at design iterations. Moreover, in practice, noise in free-form shape mechanical parts does not originate at the designed control points but in the parts themselves.

To address this problem, once the optimization process is terminated, the control points themselves are discarded and only the shapes obtained from design iterations are considered. Noise on each shape is generated by applying the changes directly to the shape. We impose new quadratic B-spline curves on the shape as noise. Figures 5.3b and c show different shapes obtained by imposing different quadratic B-spline curves over the designed shape. With this approach we can control the number of neighbor samples by controlling the number of the B-spline control points. With the same number of samples, the *SNR* from different design iterations are comparable. As more control points

are used, more shape variations within the tolerance zone are obtained, leading to a better estimate of robustness.

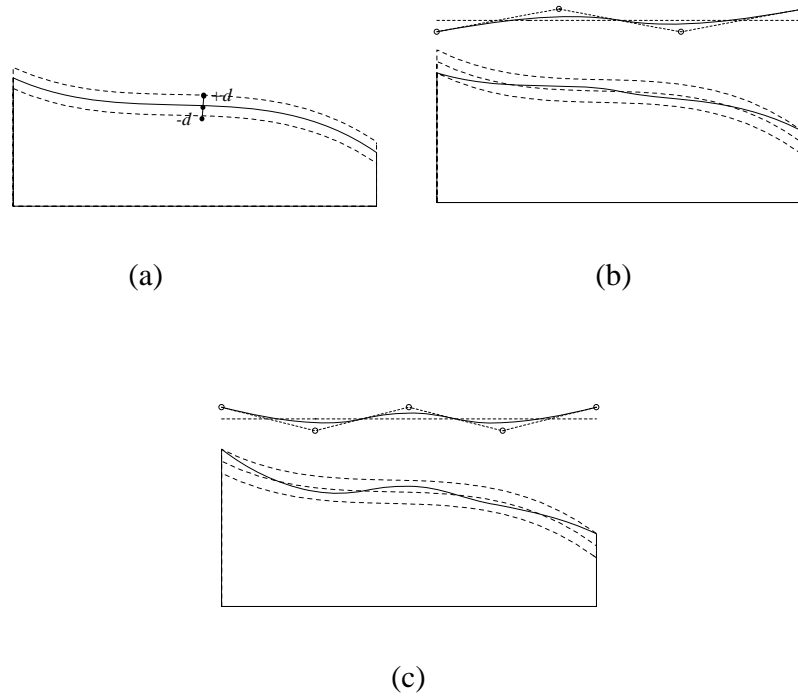


Figure 5.3 Simulation of noise in freeform shape. (a) A designed shape and its tolerance zone, (b) A 4-control point quadratic B-spline curve overlapping the designed shape, (c) A 5-control point quadratic B-spline curve overlapping the designed shape.

5.1.2 Signal-to-noise ratios

Taguchi (1986) derives signal-to-noise ratios (*SNR*) from quality loss function.

Three formulations of *SNR* for different objectives are shown in Eq. (5.1) to (5.3).

$$\text{Minimization:} \quad SNR_S(f) = -10 \text{Log} \left(\frac{1}{m} \sum_{i=1}^m f_i^2 \right) \quad (5.1)$$

$$\text{Maximization:} \quad SNR_L(f) = -10 \text{Log} \left(\frac{1}{m} \sum_{i=1}^m \frac{1}{f_i^2} \right), \quad (5.2)$$

$$\text{Target-is-best:} \quad SNR_N(f) = 10 \text{Log} \left(\frac{1}{m} \cdot \frac{\bar{f}^2}{SD^2} \right), \quad (5.3)$$

where f_i ($i = 1, 2, 3, \dots, m$) is the performance of neighboring samples around the design point and represents the effects of noise. Moreover the mean performance \bar{f} and variance s^2 are:

$$\bar{f} = \frac{1}{m} \sum_{i=1}^m f_i, \quad (5.4)$$

$$SD^2 = \frac{1}{m-1} \sum_{i=1}^m (f_i - \bar{f})^2 \quad (5.5)$$

where SD is a standard deviation.

From Eq. 5.1 to 5.3, we can observe that *SNR* are formed by basic arithmetic operations of mean and standard deviation. It is seen in Eq. 5.3 that SNR_N is the logarithmic function of the mean to standard deviation ratio. For SNR_S , we can show that it is the logarithmic function of the addition of square of mean and square of standard deviation in the form of

$$SNR_s(f) = -10 \text{Log}(\bar{f}^2 + SD^2). \quad (5.1a)$$

Here, since the number of neighboring samples m is large, $m - 1 \approx m$, so

$$\begin{aligned} \bar{f}^2 + SD^2 &= \frac{1}{m} \sum_{i=1}^m f_i + \frac{1}{m} \sum_{i=1}^m (f_i - \bar{f})^2 \\ &= \bar{f}^2 + \frac{1}{m} \sum_{i=1}^m (f_i - \bar{f})^2 \\ &= \bar{f}^2 + \frac{1}{m} \sum_{i=1}^m (f_i^2 - 2f_i\bar{f} + \bar{f}^2) \\ &= \bar{f}^2 + \left(\frac{1}{m} \sum_{i=1}^m f_i^2 \right) - 2\bar{f}^2 + \bar{f}^2 \end{aligned}$$

And finally we have

$$\bar{f}^2 + SD^2 = \frac{1}{m} \sum_{i=1}^m f_i^2.$$

Note that the formula for SNR_L in Eq. 5.2 can be considered as $SNR_s(1/f)$.

To compute SNR , noise is applied to the design point. The performance of each of the m neighbors (due to noise) is evaluated. Note that the following quantities are known as part of design specifications: target range of performance, range of operating conditions (external noise) and allowable tolerances (internal noise). In practice, noise occurs in unpredictable patterns, so there is no obvious way to simulate noise. One way to generate noise is simply use a random number generator. An alternate way is to produce systematic patterns using full or partial factorial DOE. Figure 5.4 shows the four neighbors of a design point obtained by applying 2^2 combinations of two noise factors.

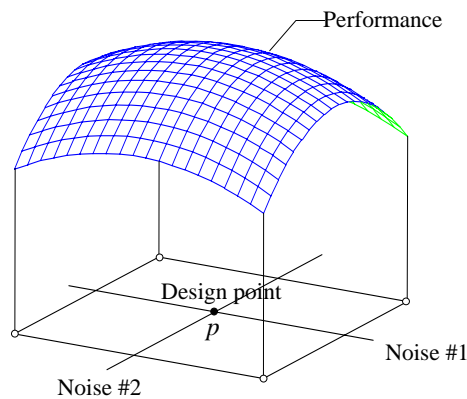


Figure 5.4 Four neighboring samples (open circles) obtained by applying 2^2 combinations of two noise factors to a design point (solid circle) are shown.

From Eq. (5.1) to (5.3), a larger SNR should lead to a design that is robust as well as close to the optimum; so a process that maximizes SNR would be a good means to achieve a compromise (the design process that leads to the compromise of robustness and optimality is sometime called “robustizaion”). However, there are some disadvantages in the use of SNR . First, it requires numerous direct solutions in order to simulate the effect of noise. If we use a design of experiment method to robustize a design with $n1$ design variables and consider $n2$ noise factors, we must construct crossed arrays (Myers and Montogomery, 1995). Figure 5.5 shows a crossed array with $n1 = 2$ and $n2 = 3$. The filled circles represent the inner array of design variables used to estimate derivative information (of SNR with respect to the design variables). The empty circles refer to the outer arrays that take into account the effect of noise to compute SNR for each point of the inner array. A total of $2^{n1} \times (2^{n2} + 1) = 36$ direct solutions are needed for one design iteration. Another disadvantage is an aliasing problem, since mean and variance are

confounded in *SNR*. For example, to maximize the performance, a design with high mean and high variance can have the same *SNR* as another design with low mean and low variance. In such cases, constraints on mean, variance and range of performance have to be imposed in the optimization process to determine a feasible region.

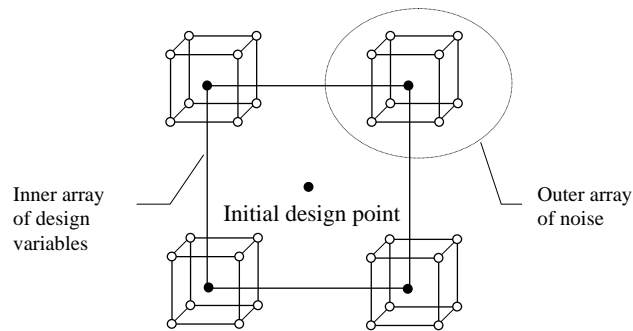


Figure 5.5 Crossed arrays for robustization.

5.1.3 Probability of failure

With the mean and variance that are computed at the same time as *SNR*, one can use the Normal distribution function

$$G(f) = \frac{1}{\sqrt{2\pi} SD} e^{-\frac{1}{2} \left(\frac{f - \bar{f}}{SD} \right)^2}, \quad (5.6)$$

where f is objective function, \bar{f} is the mean and SD is the standard deviation, to determine the probability of failure (*POF*) by integrating the function $G(f)$ over the range of f that is out of specification.

5.2 Example problems

5.2.1 Ninety-degree bend in potential flow

For the purpose of examining robustness internal noise is generated within a shape tolerance of ± 0.01 using seven-control point quadratic B-spline error curves (both ends fixed). There is no external noise introduced in this case. Thirty-two samples in a two-level DOE pattern are used per design. At each design iteration, the signal-to-noise ratio, SNR_S and the standard deviation SD is obtained using Eq. (5.1) and (5.5). Probability of failure is computed based on a normal distribution. The failure criteria is when $f > 0.6$. The means, SD , SNR_S and POF are shown in Fig. 5.6. The figure shows that the optimum design has highest SNR_S , highest mean, lowest SD and lowest POF , which imply that the design is also robust.

5.2.2 Plane symmetric diffuser in laminar flow

Internal noise is generated within a tolerance of $\pm 0.05H$ by five-control point quadratic B-spline error curve. External noise is generated by changing the operating inflow Reynolds number of 100 by $\pm 20\%$. With two-level designed experiment noise sampling, total number of samples per design is thirty-two. A worst case minimum value of $C_p = 0.42$ is specified as a requirement for the design. Probability of failure is computed based on this criterion. After evaluating C_p for all the samples, a robustness measurement is obtained in the form of mean and standard deviation of the objective function, SNR_L and POF as shown in Fig. 5.7. With all the information, the optimum

design is found to be robust as indicated by a high SNR_L , low standard deviation and low POF .

5.2.3 Axisymmetric diffuser in laminar flow

The same process as in 5.2.2 is applied. The result of the analysis is shown in Fig. 5.8. Again, the optimum diffuser is found to be robust.

5.2.4 Torque arm under static load

For the purpose of robustness analysis, internal noise within the shape tolerance of ± 5 mm is applied in the form of quadratic B-spline error curves with 7 control points (fixed both ends) using two-level DOE pattern. This makes the number of samples to simulate noise 32 per design. Figure 5.9 shows the convergence history of weight, means, SD , SNR_N and POF , all with respect to maximum element stress.

Design c may be chosen as a compromise between robust design (design a) and optimum design (design h). Because design c has a much lower standard deviation and a volume of 83% of the initial design (compared to the minimum volume of 67% of the initial design of design h), but have almost zero POF compare to design h, which has 62% POF .

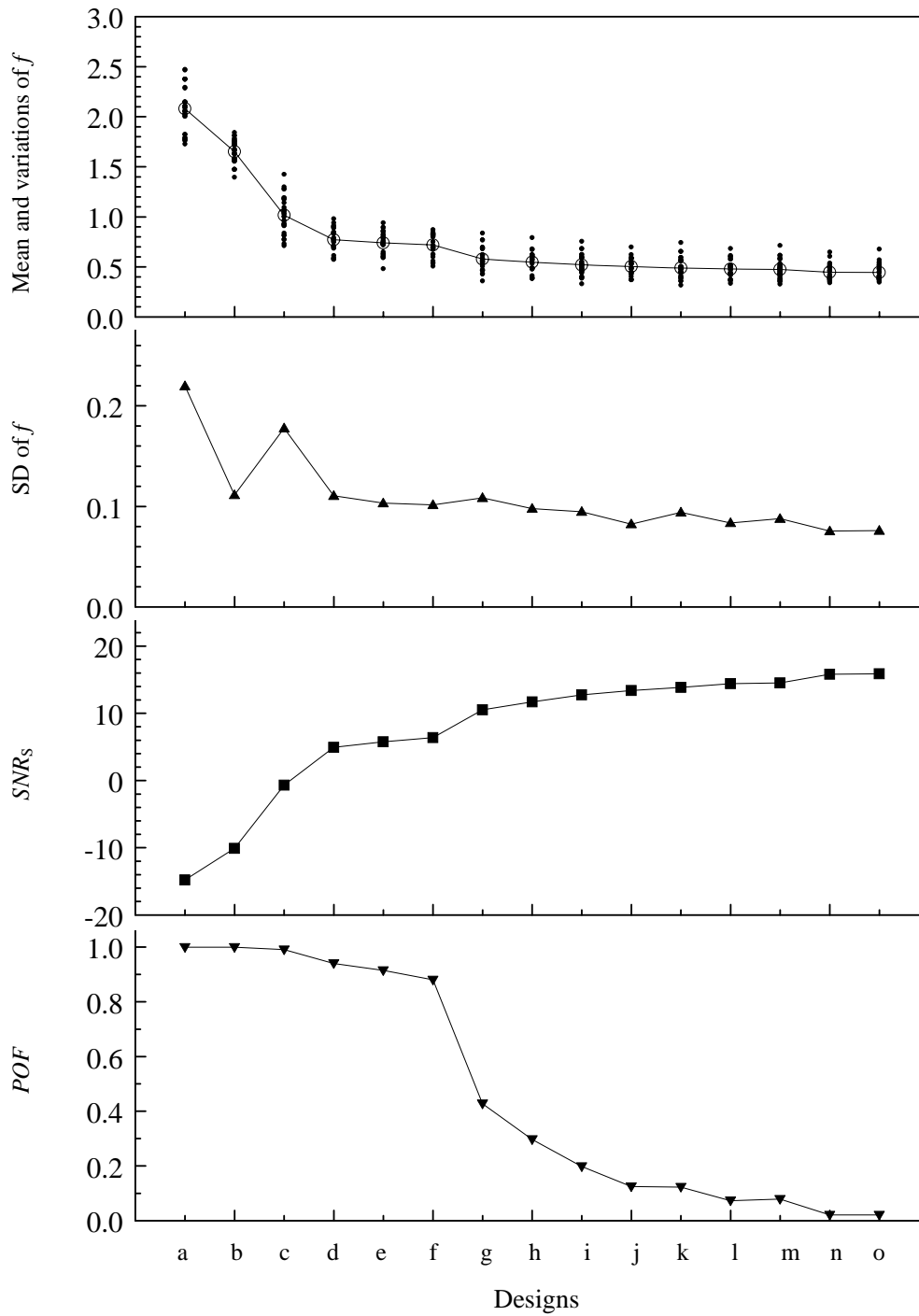


Figure 5.6 Robustness analysis for the design of ninety-degree bend.

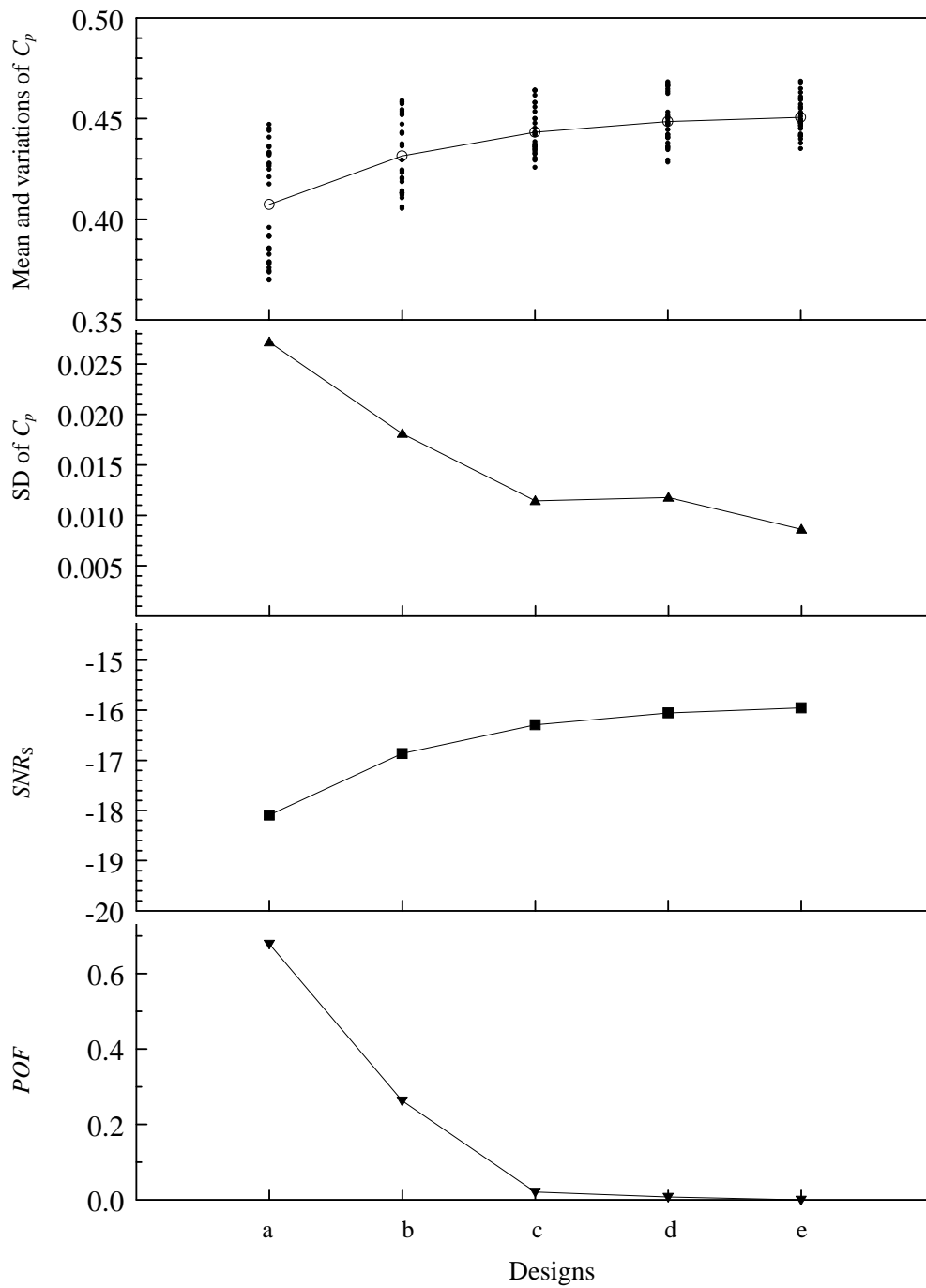


Figure 5.7 Robustness analysis of plane symmetric flow diffusers for Reynolds number of 100.

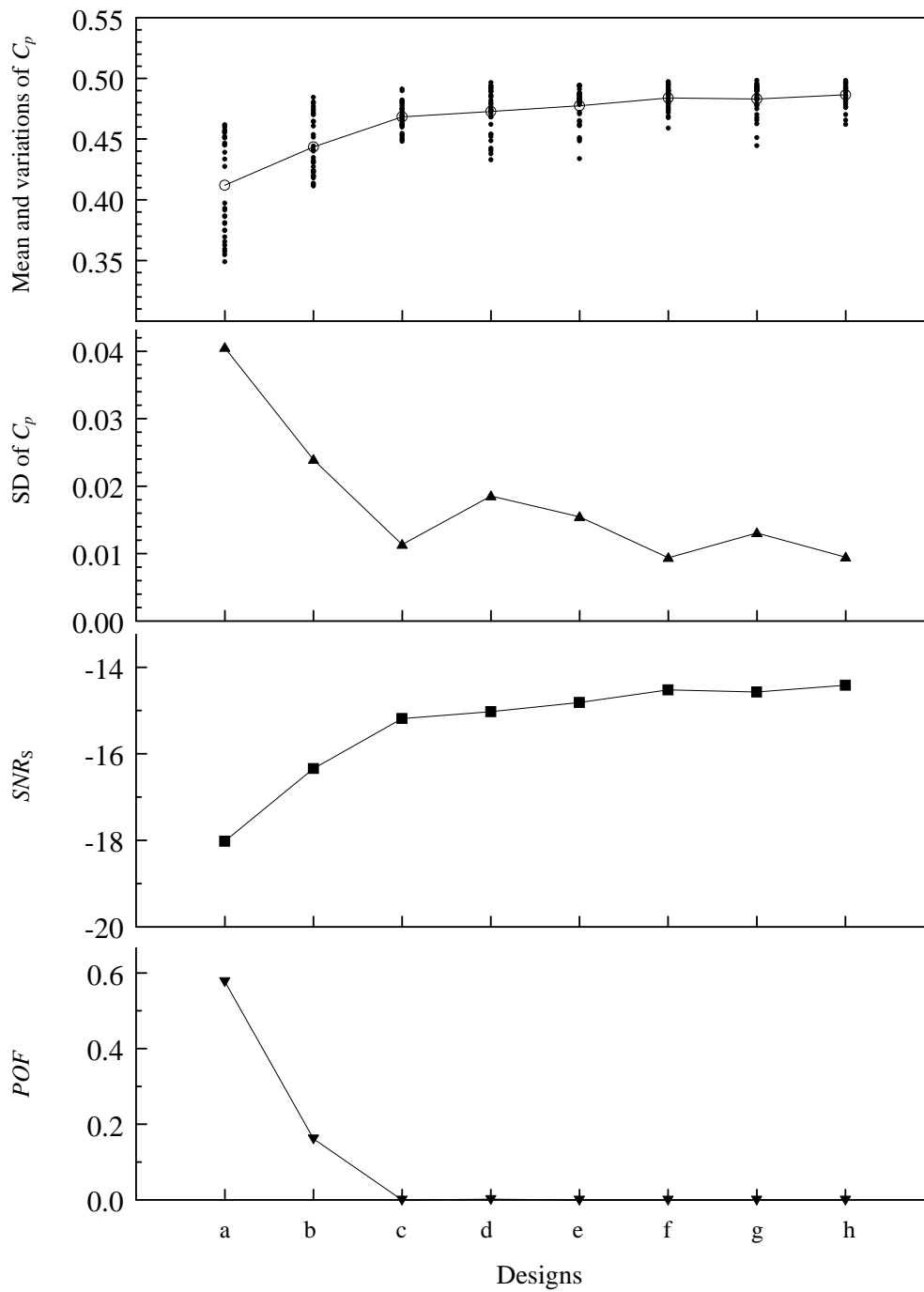


Figure 5.8 Robustness analysis of axisymmetric flow diffusers for Reynolds number of 100.

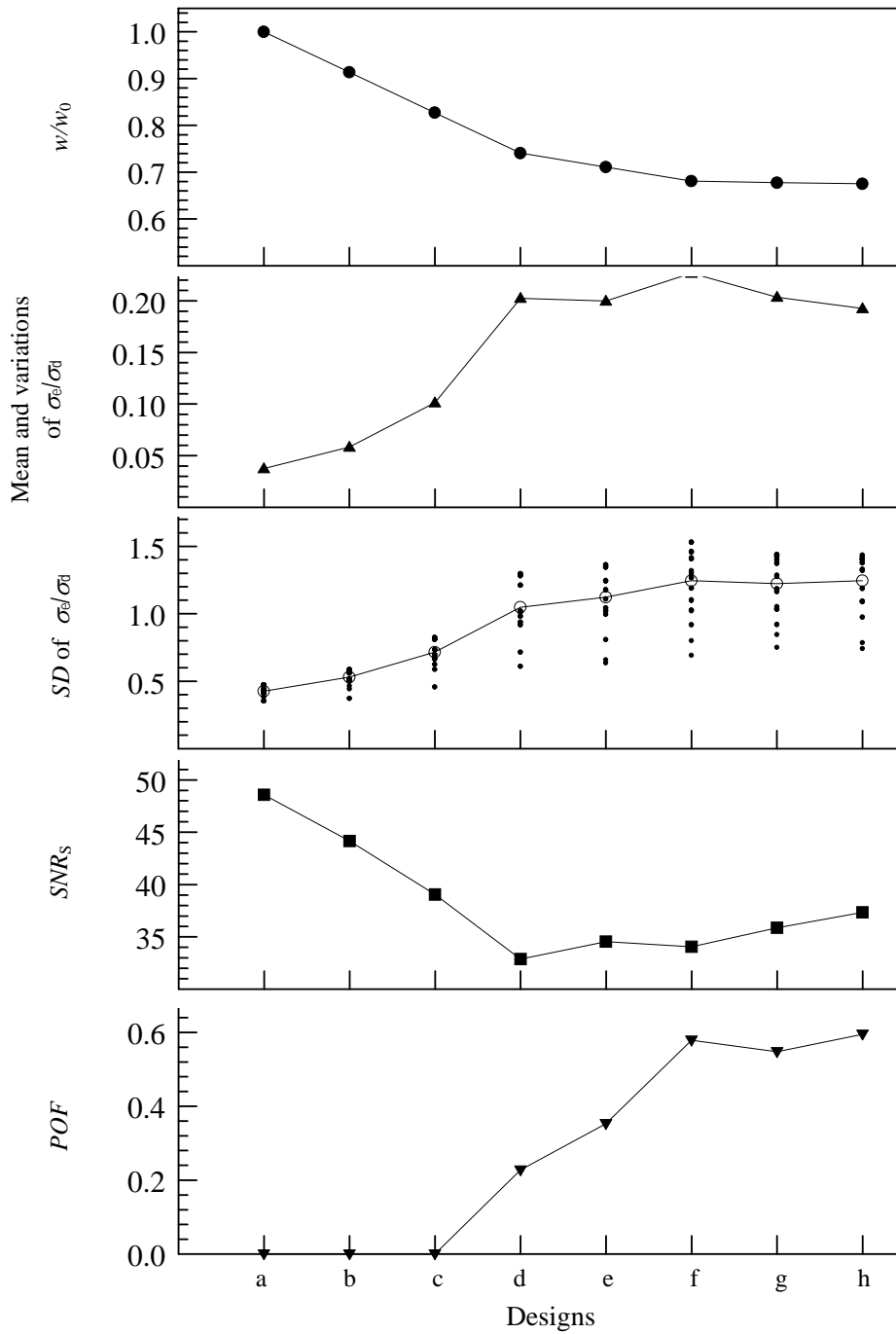


Figure 5.9 Robustness analysis for design of torque arms.

5.3 Discussion

The robustness analysis of the first three examples referred to objective functions that were obtained from integration (sum of nodal transverse velocity in the first example and area averaged pressure in the second). In the last example, robustness is based on a stress constraint, which is the local maximum element stress. By nature, the values from integration are usually less sensitive to noise than the local point values. The physical nature of each problem also plays a role in robustness of the optimum results. For example, performance of the optimum diffuser seemed to be not very sensitive to internal noise (shape changes) since for the optimum design, minor changes in shape do not cause much change to the whole flow field so the pressure rise does not change much. In contrary, for the torque arm problem, minor change of shape at some location can cause a large change in local stress concentration; hence the optimum torque arm is more sensitive to internal noise.

As mentioned in Chapter 1, our approach to robust-optimum design problems is to find optimum designs in term of objective function with robustness as a constraint. However, when we put the idea to work the robustness constraint is imposed after the optimization processes are completed in order to reduce number of direct solutions that may require if robustness analysis is perform during optimization process.

In all the examples we find that the designs with higher *SNR* or lower *POF* also have lower standard deviations and better mean (higher for maximization problems; lower for minimization problems), so we may use either *SNR* or *POF* as a scalar to

quantify robustness. From the examples, we can see that SNR is a relative quantity. It can indicate that one design is more or less robust than the other but it cannot provide an absolute measure such that one can say, for example, that $SNR > 40$ implies a robust design. POF , on the other hand, provides an absolute statistical measure, but to estimate it more closely a suitable distribution function should be chosen according to the histogram plot (in all the examples, we assume a normal distribution). Figure 5.10 shows an example of a histogram plot of the stress in torque arm designs subjected to noise. It shows that the initial design follows the normal distribution but other designs seem to have non-symmetric distributions (leaning toward the worse side). This indicates that the POF for the optimum design in this case is under-predicted.

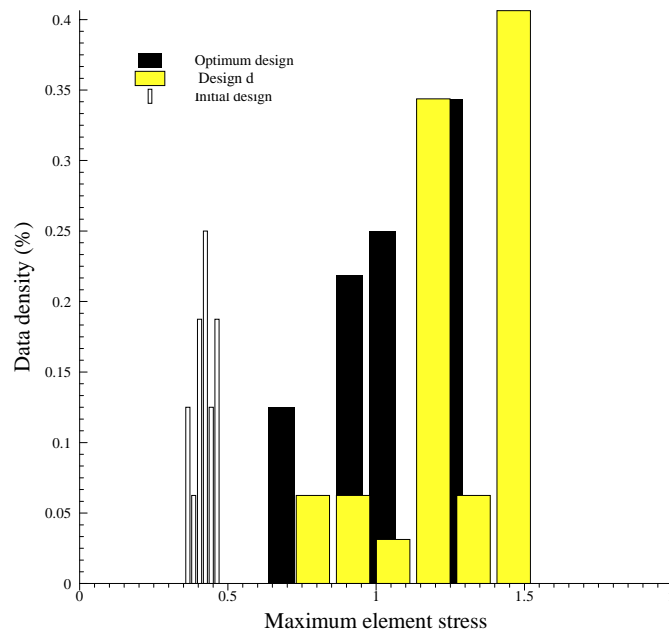


Figure 5.10 Weight vs. probability of failure of torque arms.

To check for the convergence of the robustness analysis results, we carry out the robustness analysis of the torque arm problem using different number of neighboring samples. The result in Fig. 5.11 shows that the current number of samples (32 samples per design) is sufficient to identify trends for comparative purposes.

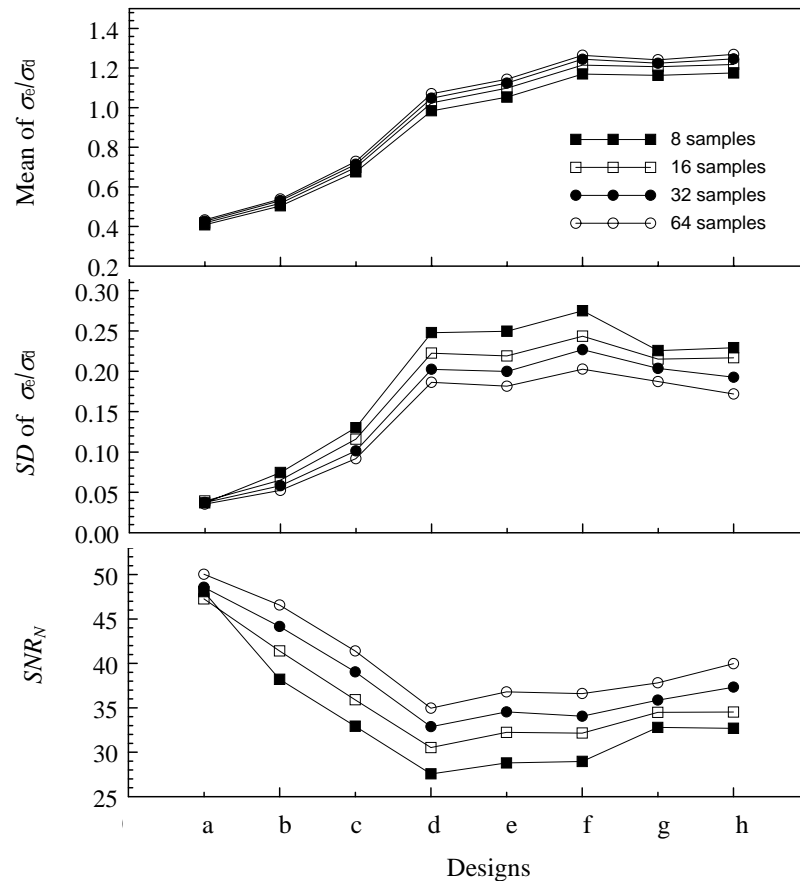


Figure 5.11 Convergence study of the robustness analysis of the torque arm problem.

In the torque arm problem, if we examine the problem as a multicriteria problem with the weight and probability of failure as the objectives then we can create a plot as shown in Fig. 5.12 and conclude that any design between the third and the eighth

iteration (designs c thru h) can be a solution, depending upon how much probability of failure or weight is allowed. This kind of problem will be discussed in the next chapter.

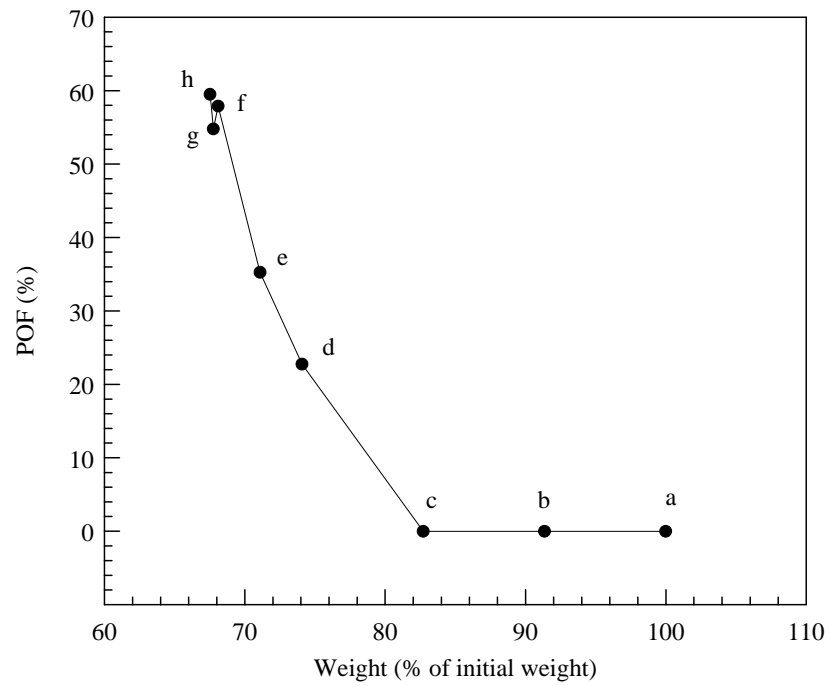


Figure 5.12 Weight vs. probability of failure.

Chapter 6

Design of Corrugated Panel Structures

In the previous chapters we have explored optimum and robust geometric design of free-form mechanical parts and used four academic examples to demonstrate the design process, each with a single objective. In this chapter we explore a different class of geometric design, fixed-form geometric design. This class of design problems occurs in many practical situations. Moreover, engineers also encounter the need to design parts that satisfy multiple objective functions. These so-called multicriteria design problems will also be explored in this chapter through the design of corrugated panel structures.

The strength of a plate is frequently enhanced by adding stiffening elements. The addition of these elements is a preferred mean of reducing cost and weight rather than simply using a thicker plate. Many studies have addressed the problem of design of stiffeners for a variety of applications. Bendsoe (1989) and Luo and Gea (1998) set up an optimum stiffener design problem as a material distribution problem. In the later study using theory of composite materials, they model an increase in an effective Young's modulus with an addition of stiffening material. With the assumption of an effective

Young's modulus, optimization problems were set up to distribute and orient a fixed amount of stiffening material in order to create a plate and shell structure that maximizes the first few modes of natural frequencies or minimize the mean compliance under static loads. This approach in general leads to an optimum stiffener design of arbitrary shape, which may be acceptable for applications such as fiber glass reinforced structures but may be unsuitable in sheet metal or concrete applications due to manufacturing or cost reasons. Figure 6.1a shows an exploded view of a plate structure that uses a freeform sheet metal stiffener.

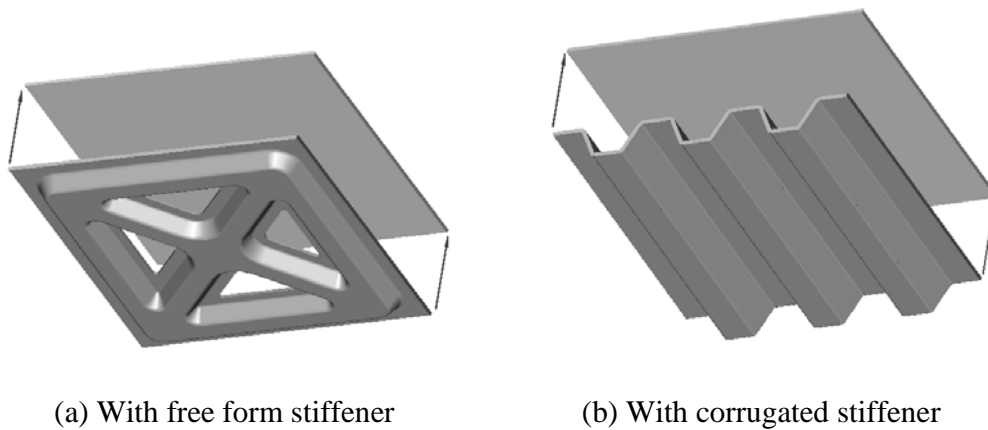


Figure 6.1 Panel structures.

A simpler kind of stiffener, such as a corrugated stiffener (or so-called corrugated cladding when used by itself without the flat panel) shown in Fig. 6.1b, is easier to form and assemble leading to lower cost. Although the best strength to weight ratio cannot be guaranteed, decent performances can be achieved with proper design. Faupel and Fisher (1981) provide experimental data on stiffness of fifteen different plate stiffener configurations, which have rather simple geometry such as angles, corrugated plate,

channels, honeycomb and ribs. The comparison under static loading indicates that the corrugated stiffener is among the stiffest structures.

The following studies focus on the design of corrugated claddings. They set up the shape optimization problems to find the optimum profiles of the corrugated claddings for specific objectives under specific operating conditions and constraints. Seaburg and Salmon (1971) try to minimize the weight of a corrugated cladding while satisfying a stress constraint. In Lee, et.al. (1995), the objective is to minimize the bending stress while satisfying some imposed dimensional constraints and this study also investigates corrugated panel structures. The design of corrugated panels to minimize cost and weight with several failure criteria as constraints was explored by Rahman (1996). All those studies provide methodologies for optimum shape design under specific objectives and constraints. However, they do not provide fundamental design guidelines or rules such as optimum thickness of the material, optimum pitch and optimum height. The objective of this chapter is to find such rules.

Finding an optimum corrugated stiffener design is not trivial. Without a constraint on weight or an objective function e.g. natural frequency, maximum deflection etc., the design problem is considered multicriteria. The example shown in Fig. 6.2 is based on the maximization of natural frequency and minimization of weight. From numerical experiments, the relationship between natural frequency and weight of the structure does not exhibit a clear maximum but there exists a boundary formed by extreme designs (optimum designs and worst designs). Each solid point in Fig. 6.2 represents one design with each open point being the optimum design in its own weight class shown as vertical

bars. For this kind of problem the goal is to find a set of optimum designs that are a compromise between different objectives. This set of designs is the so-called Pareto solutions (Pareto, 1906). Pareto solutions can be obtained by collecting the designs that lie on a part of boundary of the objective function space shown as thick line in Fig. 6.2. In order to find the boundary, the design space has to be explored or to be filled with trial designs and if there are large number of trial designs then the part of the boundary of those designs (design 1 to 5 in Fig. 6.2) will converge to the Pareto solutions.

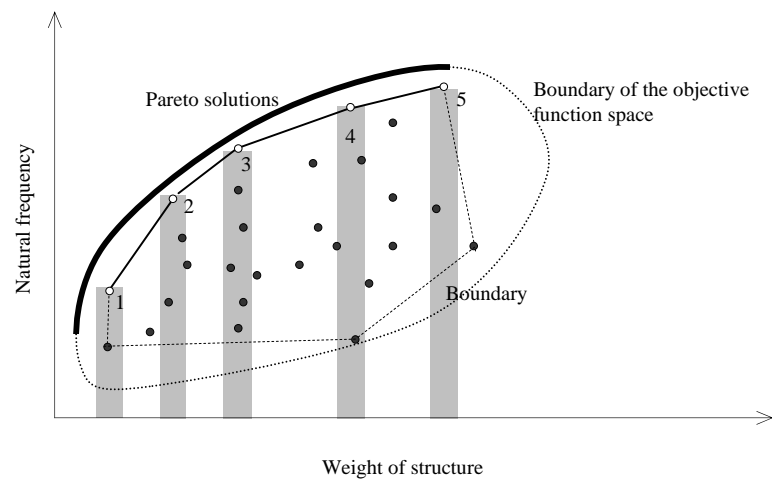


Figure 6.2 Pareto solutions. Objectives include maximizing natural frequency and minimizing weight.

Genetic algorithms have been used intensively in multicriteria optimization but usually do not address the robustness issue. In this study an exhaustive search is used to generate trial designs, this may seem like the PSI method (Statnikov and Matusov, 1995) but the purpose is not only to find an optimum design but also to fill the design space with a variety of designs during the search so that the information can be used later to determine the robustness of the designs.

Section 6.1 discusses the theoretical formulation for deflection, stress and natural frequency of plate structures. It also describes how similarity can be used to identify non-dimensional parameters. Maximization of natural frequency and minimization of maximum deflection are the two objectives that we consider. We do not use maximum stress as an additional objective function because we cannot obtain an accurate stress solution from the solver using our current finite element models (see Appendix B.4 for convergence test of the solver). The solution process consists of two stages. The first stage is data generation, in which the design variables are set-up and trial designs are generated by varying those design variables. A finite element model is constructed for each design and numerical experiments are performed to obtain the values of the two objective functions. This stage is presented in Section 6.2. The second stage is data analysis. In this stage robustness analysis is performed to obtain *SNR* of both objective functions. Those *SNR* together with the two objective functions are taken to be the four design objectives. Upon observation of the objective function space, criteria are set up and a feasible solution set is selected. The robust-optimum solutions are obtained by comparing the solutions obtained by using min-max method with the solutions obtained using single-objectives. Finally we compile all the information and come up with the design rules. The second stage is presented in Section 6.3. A discussion is presented in Section 6.4.

6.1 Theoretical background

Before we discuss corrugated panel structures, let us first consider a simple plate as shown in Fig. 6.3. A square plate of width a and thickness t , simply supported along all the four edges is subjected to a uniformly distributed load of intensity q . The material is assumed to be isotropic. According to Timoshenko (1940), the governing equation for the deflection u is a biharmonic equation.

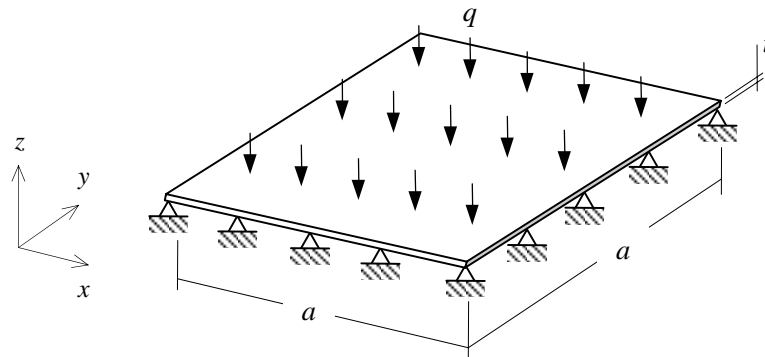


Figure 6.3 Plate with simply supports.

$$D \left(\frac{\partial^4 u}{\partial x^4} + 2 \frac{\partial^4 u}{\partial x^2 \partial y^2} + \frac{\partial^4 u}{\partial y^4} \right) = q \quad (6.1)$$

with

$$D = \frac{E I}{(1 - \nu^2) a}$$

where E is the Young's modulus, ν is the Poisson's ratio of the material and I is the moment of inertia around the centerline of the plate cross section which is equal to $at^3/12$.

One can solve Eq. 6.1 and obtain u_{\max} , the maximum deflection at the center of the plate and σ_{\max} , the maximum bending stress located at mid-point of each edges to be

$$u_{\max} = 0.00406 \frac{a^4 q}{D}, \quad (6.2)$$

$$\sigma_{\max} = 0.287 q \frac{a^2}{t^2}. \quad (6.3)$$

Dynamic behavior is described by the governing equation

$$D \left(\frac{\partial^4 u}{\partial x^4} + 2 \frac{\partial^4 u}{\partial x^2 \partial y^2} + \frac{\partial^4 u}{\partial y^4} \right) + \rho t \ddot{u} = 0. \quad (6.4)$$

From the solution for harmonic motion (Rao, 1999), the first mode natural frequency, ω , can be obtained as

$$\omega = 0.907 \frac{t}{a^2} \sqrt{\frac{E}{\rho(1-\nu^2)}} \quad \text{Hz} \quad (6.5)$$

Now consider a case where a corrugated stiffener is attached to the bottom of the square plate to form a strong plate structure. In sheet metal applications, the two parts are usually held together by spot welding. If the parts are too thick for spot welding then slots are cut into one of the part in order to create welding area. Modeling of the welded joint is a complicated process. We avoid this complication by assuming that a sufficient number of welded joints are made so that the structure can be treated a single homogeneous part of different thickness as shown in Fig. 6.4. From a static point of view, the structure behaves as a stiffer plate of orthotropic nature, i.e. stiffer in one direction than the other. Then the governing equation for static deflection becomes the Huber equation.

$$D_x \frac{\partial^4 u}{\partial x^4} + D_{xy} \frac{\partial^4 u}{\partial x^2 \partial y^2} + D_y \frac{\partial^4 u}{\partial y^4} = q \quad (6.6)$$

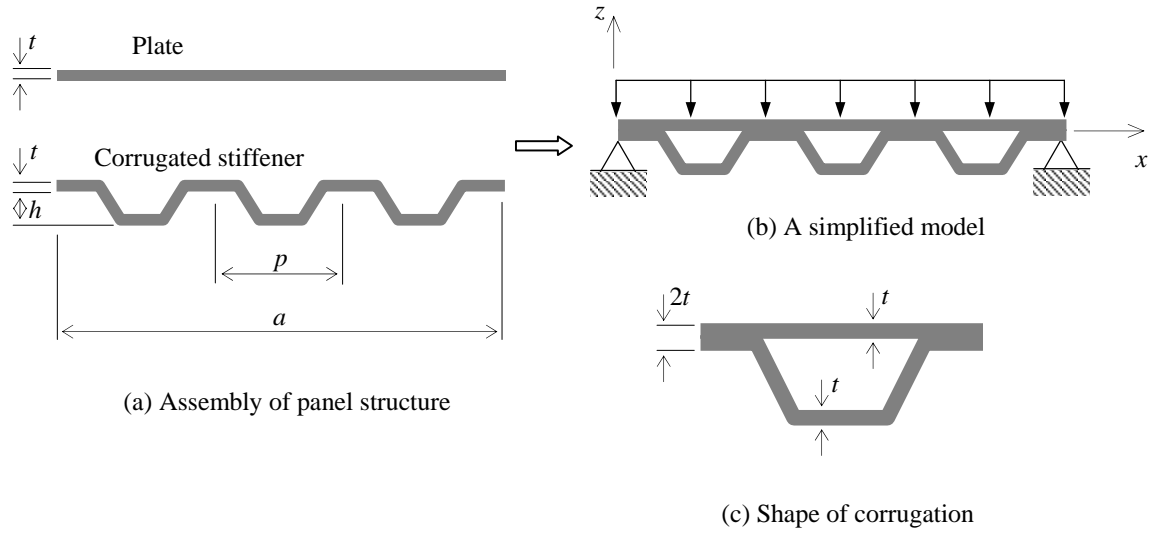


Figure 6.4 Simplified model of a corrugated panel structure (cross-sectional view).

Troitsky (1967) gives stiffness values D_x , D_y and D_{xy} for box-type bridge structures that can be applied to the plate structure in Fig. 6.4(b). These are

$$\begin{aligned} D_x &= \frac{E}{(1-\nu^2)} \frac{I_{yy}}{a}, \\ D_y &= \frac{E}{(1-\nu^2)} \frac{I_B}{p}, \\ D_{xy} &= G \frac{4A_R^2}{\sum_i \frac{s_i}{t_i}}. \end{aligned} \quad (6.7)$$

In the above, I_{yy} is the moment of inertia about the y-axis, which is approximated as $a(2t)^3/12$; I_B is moment of inertia of the cross section in Fig. 6.4(c) around the neural axis; G is the shear modulus. A_R is the area enclosed inside the corrugated fold; s_i is the perimeter of the enclosing wall and t_i is the corresponding thickness. For an isotropic

material the shear modulus is a linear function of the Young's modulus and is given by $G = E/2(1 + \nu)$. Note that all the moment of inertia terms are functions of geometry. Now we scale all the length scales with the plate width a and obtain non-dimensional geometric parameters as

$$\text{non-dimensional plate thickness} \quad T = t/a,$$

$$\text{non-dimensional height of corrugation} \quad H = h/a,$$

$$\text{and non-dimensional pitch of corrugation} \quad P = p/a,$$

The Huber equation can be written in non-dimensional form as

$$\left(\frac{g_x}{1-\nu^2} \right) \frac{\partial^4 U}{\partial X^4} + \left(\frac{g_{xy}}{1+\nu} \right) \frac{\partial^4 U}{\partial X^2 \partial Y^2} + \left(\frac{g_y}{1-\nu^2} \right) \frac{\partial^4 U}{\partial Y^4} = 1 \quad (6.8)$$

where

$$U = \frac{Eu}{qa} \quad (6.9)$$

and g_x, g_{xy}, g_y are function of geometry which are invariant as long as the similarity of geometry are kept.

Similarity of Eq. 6.8 will be maintained as long as Poisson's ratio ν is invariant. The solution of the Huber equation can be written in the form of Fourier series but the way to compute coefficients in the series is complicated and will not be discussed in this thesis. The expressions for maximum deflection, maximum bending moment and natural frequency are expected to be close to the Eq. 6.2, 6.3 and 6.5 respectively. With this assumption we scale the rest of the solutions as follows.

Non-dimensional stress, $S = \sigma / q$ (6.10)

Non-dimensional frequency, $\Omega = a\omega / \sqrt{E/\rho}$ (6.11)

Lastly, let w be the weight of the structure, the non-dimensional weight can be written as,

$$W = w / \rho a^3 \quad (6.12)$$

These expressions are numerically proven to be true and are shown in Table 6.1 in Section 6.3. With this non-dimensionalization and assuming a Poisson's ratio of 0.29 (close approximation for steel and most alloys), the solutions for maximum deflection, maximum stress and natural frequency of a flat plate (Eq. 6.2, 6.3 and 6.5 respectively) can be written in non-dimensional forms as the following.

$$U_{\max} = \frac{0.0446}{W^3} \quad (6.13)$$

$$S_{\max} = \frac{0.287}{W^2} \quad (6.14)$$

$$\Omega = 0.948W \quad (6.15)$$

6.2 Data generation

Several variables are needed to configure the corrugated stiffener, These are; height (H), thickness (T), pitch (P) and shape of the corrugation. Note that, in this study, the thickness of the corrugated stiffener is set to be the same as the plate thickness. For computational purposes, shape of corrugation will be represented by a parameter Γ . With these four parameters the weight W and the objective functions natural frequency Ω and maximum deflection U_{\max} become:

Weight,	$W = W(T, \Gamma, P, H)$
Natural frequency,	$\Omega = \Omega(T, \Gamma, P, H)$
Maximum deflection,	$U_{\max} = U(T, \Gamma, P, H)$

Three basic shapes of corrugation are considered, which are rectangle ($\Gamma = 1$), trapezoid ($0 < \Gamma < 1$), and triangle ($\Gamma = 0$). The three shapes are constrained by height and pitch as shown in Fig. 6.5.

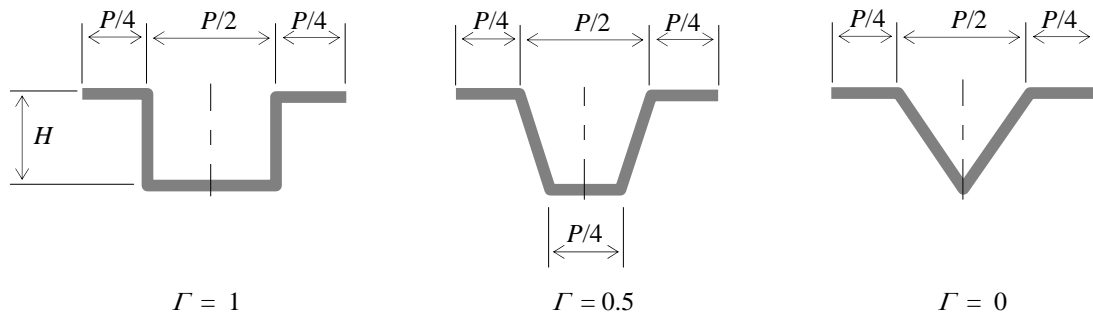


Figure 6.5 Shapes of the corrugations.

A finite element solver I-DEAS for linear statics and response dynamics is used to solve for deflections and natural frequencies of the designed structures. With the capability of I-DEAS to run in a batch mode, we can set up an automated process to run all the experiments without user intervention (see Appendix C for detail on batch mode programming). But before setting up the experiments, proper modeling assumptions have to be made. Moreover the similarity derived in the previous section has to be validated. The next sections discuss these issues, followed by a section describing the data generation method.

6.2.1 Modeling assumptions

The following assumptions are made to simplify the computation;

- (a) Body force is neglected since the stress generated by the weight of the structure is negligible compared to that due to load.
- (b) Radius of bending is neglected.
- (c) We assume that there are sufficient joints between the plate and the stiffener to treat the assembled structure as one homogeneous piece (see Fig. 6.4c)

For computational efficiency linear quadrilateral thin shell elements are used instead of solid elements. From a convergence study (see Appendix B.4), element size of about 5% of the plate width is found to provide an accuracy of about 10% for natural frequency and 15% for maximum deflection. However the stress solution is not grid converged hence we will not use the stress solution. The level of accuracy of natural frequency and maximum deflection is sufficient to provide comparisons between different designs. Figure 6.6 shows typical grids that are used through out this study.

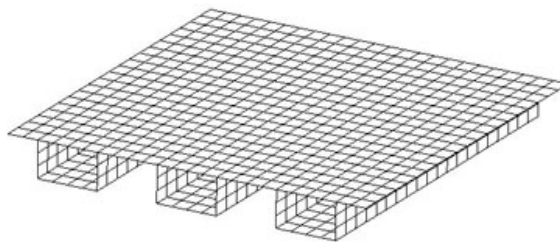


Figure 6.6 Typical quadrilateral grids.

6.2.2 Validation of similarity

In order to validate the similarity derived in Section 6.1 we carry on a set of six numerical experiments to find natural frequency, maximum deflection and maximum stress in corrugated panel structures with simply supports and under uniformly distributed loads. In the first experiment material properties are $E_1 = 207$ Gpa, $\rho_1 = 7820$ kg/m³ and $\nu = 0.29$. The shape of corrugation is a rectangle and the structure has the following dimensions: $a_1 = 0.1$ m, $h_1 = 0.01$ m, $p_1 = 0.03$ m and $t_1 = 0.0005$ m. This structure has a weight of $W = 0.013$. Load intensity is $q_1 = 10,000$ N/m². In five other experiments, these parameters (E, ρ, q, a) are altered while relative geometry is kept invariant. The results from the six experiments (shown in Table 6.1) show that the non-dimensional solutions are the same in all experiments and thus the derived similarity is valid. The first mode shape of the natural frequency for the first run is shown in Fig. 6.7. A stress distribution and deflection plot is shown in Fig. 6.8.

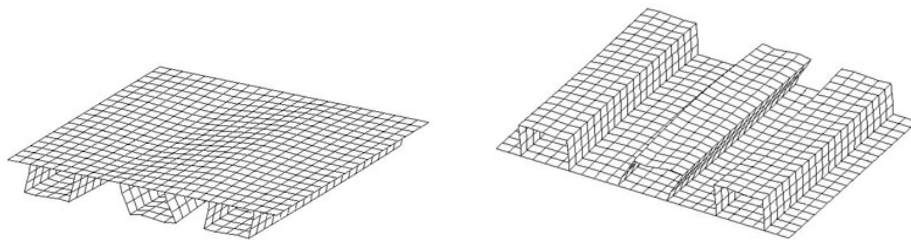


Figure 6.7 First mode shape from two view angles.

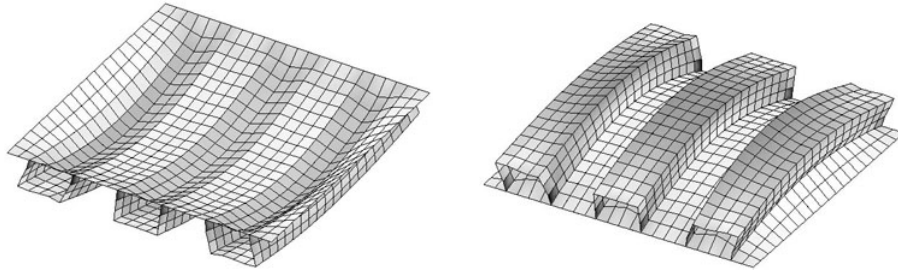


Figure 6.8 Stress distribution and deflection from two view angles. Dark areas represent high stress.

Table 6.1 Validation of similarity.

Experiment No.	Properties				Results			Non-dimensional results		
	E	ρ	q	a	ω (Hz)	u (mm.)	σ_{\max} (Mpa)	Ω	U_{\max}	S_{\max}
1	E_1	ρ_1	Q_1	a_1	2680	0.0033	8.3	0.052	674	828
2	$2E_1$	ρ_1	Q_1	a_1	3790	0.0016	8.3	0.052	674	828
3	E_1	$2\rho_1$	Q_1	a_1	1900	0.0033	8.3	0.052	674	828
4	E_1	ρ_1	$2q_1$	a_1	2680	0.0065	16.5	0.052	674	828
5	E_1	ρ_1	Q_1	$2a_1$	2680	0.0065	8.3	0.052	674	828
6	$2E_1$	$3\rho_1$	$4q_1$	$5a_1$	2190	0.033	33.1	0.052	674	828

6.2.3 Trial design generation

A set of trial designs is generated from combinations of the four design variables in the following ranges:

Thickness,	$0.0005 \leq T \leq 0.01$
Pitch	$0.025 \leq P \leq 0.5$
Height	$0.02 \leq H \leq 0.2$
Shape	$0.0 \leq \Gamma \leq 1.0$

The weight is in the range of $0.002 \leq W \leq 0.02$.

Twenty five hundred trial designs are generated from the pre-determined discrete combinations of the following values:

Thickness,	$T =$	(0.0005, 0.001, 0.0012, 0.0015, 0.0018, 0.0002, 0.0022, 0.0025, 0.0028, 0.0003, 0.0035, 0.004, 0.0045, 0.005, 0.006, 0.007, 0.008, 0.009, 0.010)
Pitch,	$P =$	(0.025, 0.04, 0.05, 0.054, 0.06, 0.07, 0.08, 0.1, 0.11, 0.12, 0.13, 0.15, 0.18, 0.22, 0.29, 0.4, 0.5)
Height,	$H =$	(0.02, 0.025, 0.05, 0.075, 0.1, 0.125, 0.12, 0.175, 0.2)
Shape,	$\Gamma =$	(0, 0.5, 1)

Not all combinations of the above values are selected, the trial designs are constrained by the weight range and some unreasonable configurations are eliminated (for example too high and too thin). Note that these trial designs are not generated all at

once but rather in a progressive manner, i.e. one thousand designs are generated in the beginning and the numerical experiments are carried on, then we observe the design and objective function spaces to determine the regions that need additional exploration and generate more trial designs to fill those regions.

Two thousand additional trial designs are randomly generated to be uniformly distributed along the weight. This is done by using a random number generator to generate values of design variables in the ranges given above. The weight of each design is computed. The weight range is divided into twenty equal intervals and we make sure that there are equal number of designs in every weight interval, i.e. each interval has one hundred designs.

Figures 6.9a to d show the distribution of thickness, pitch, height and shape of the 4,500 trial designs with weight. The open points are the randomly generated designs and the solid points are the pre-determined designs.

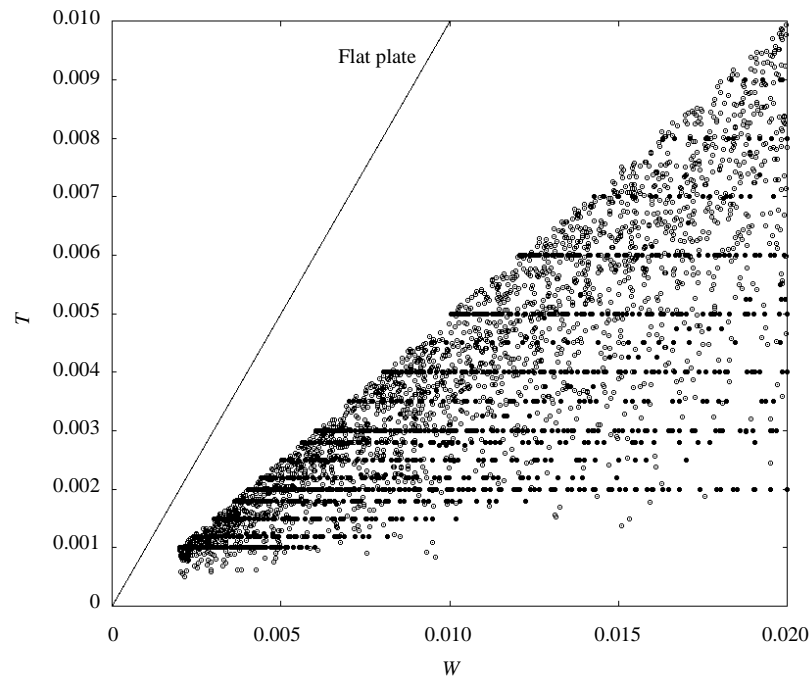


Figure 6.9a Distribution of the thickness of the trial designs with weight.

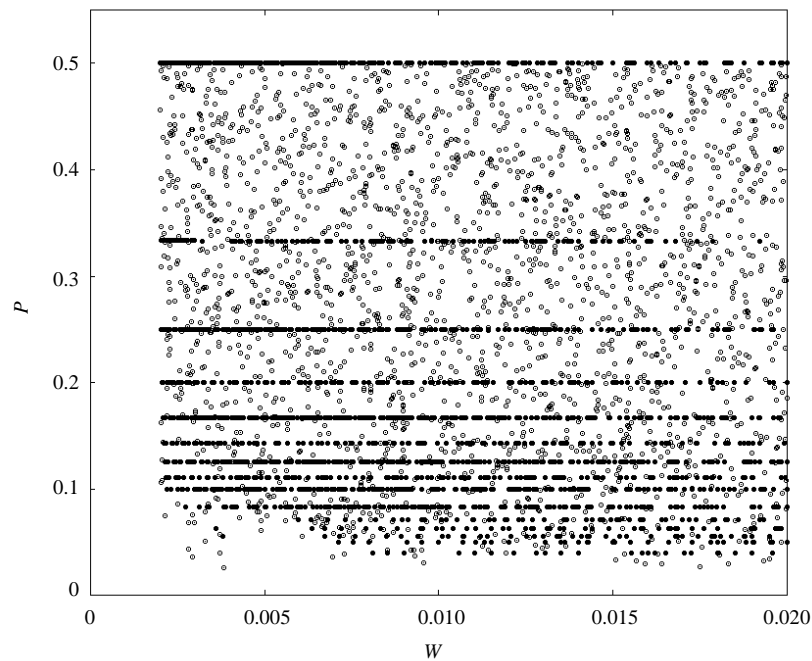


Figure 6.9b Distribution of the pitch of the trial designs with weight.

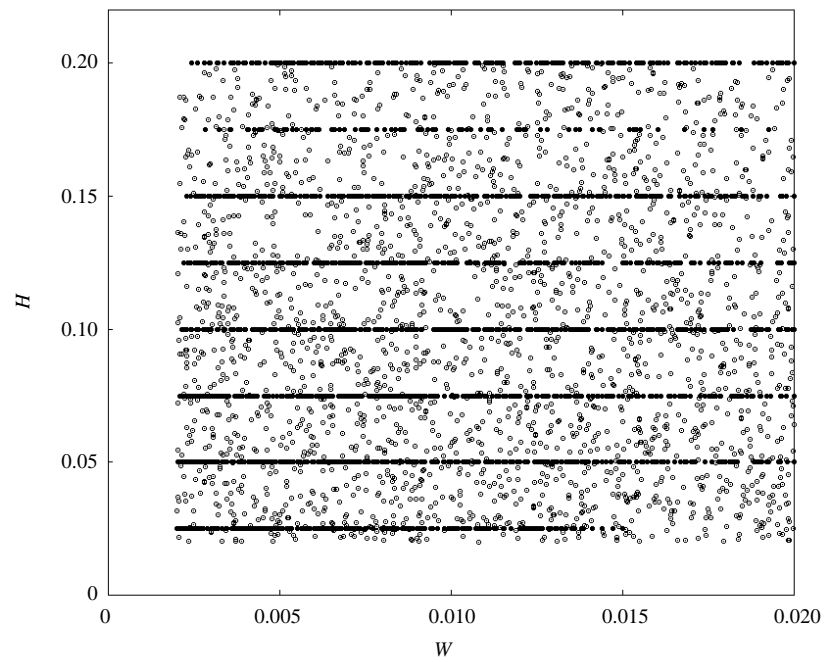


Figure 6.9c Distribution of the height of the trial designs with weight.

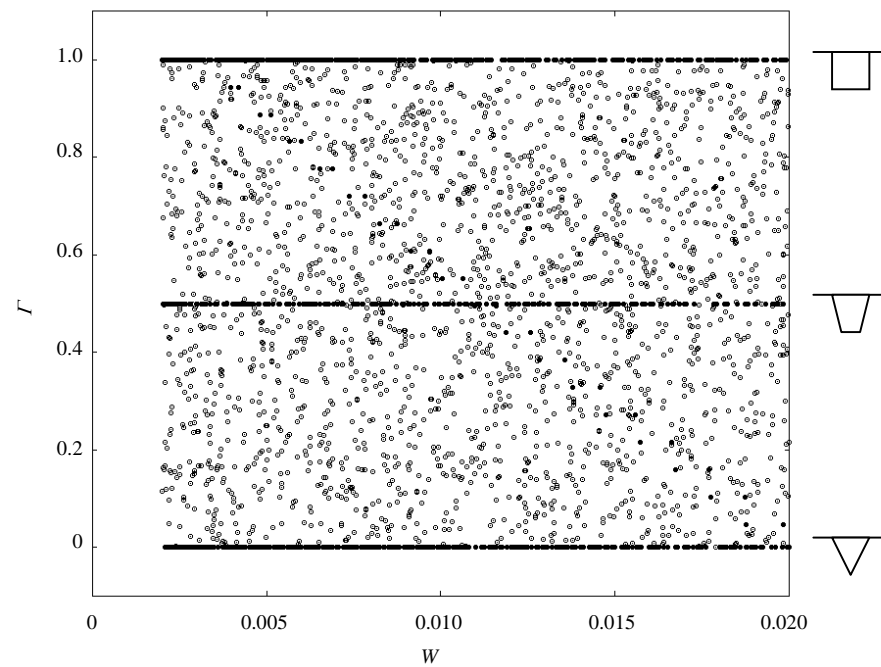


Figure 6.9d Distribution of the shape of the trial designs with weight.

6.2.4 Results of numerical experiments

Results of numerical experiments are shown in Fig. 6.10a and b. In both figures, each point represents one design; the solid lines represent the natural frequency and maximum deflection of flat plates (according to Eq. 6.15 and 6.13). The computations were carried out using SDRC I-DEAS Master Series 7 software running on a personal computer with Pentium III 500Mhz CPU and Windows NT operating system. Approximate time to solve for each design is 2 minutes, which results in 150 hours of total computation time for 4,500 trial designs.

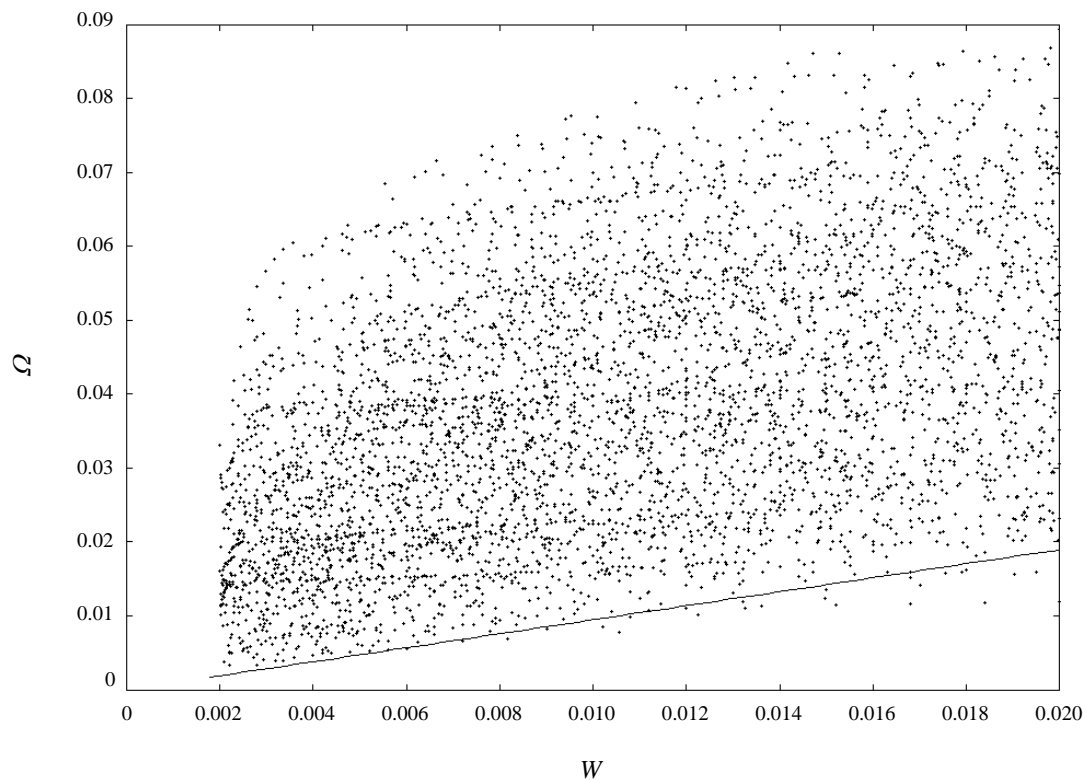


Figure 6.10a Natural frequency of the trial designs plotted against their weight. The solid line represents the variation of the natural frequency of a flat plate with weight.

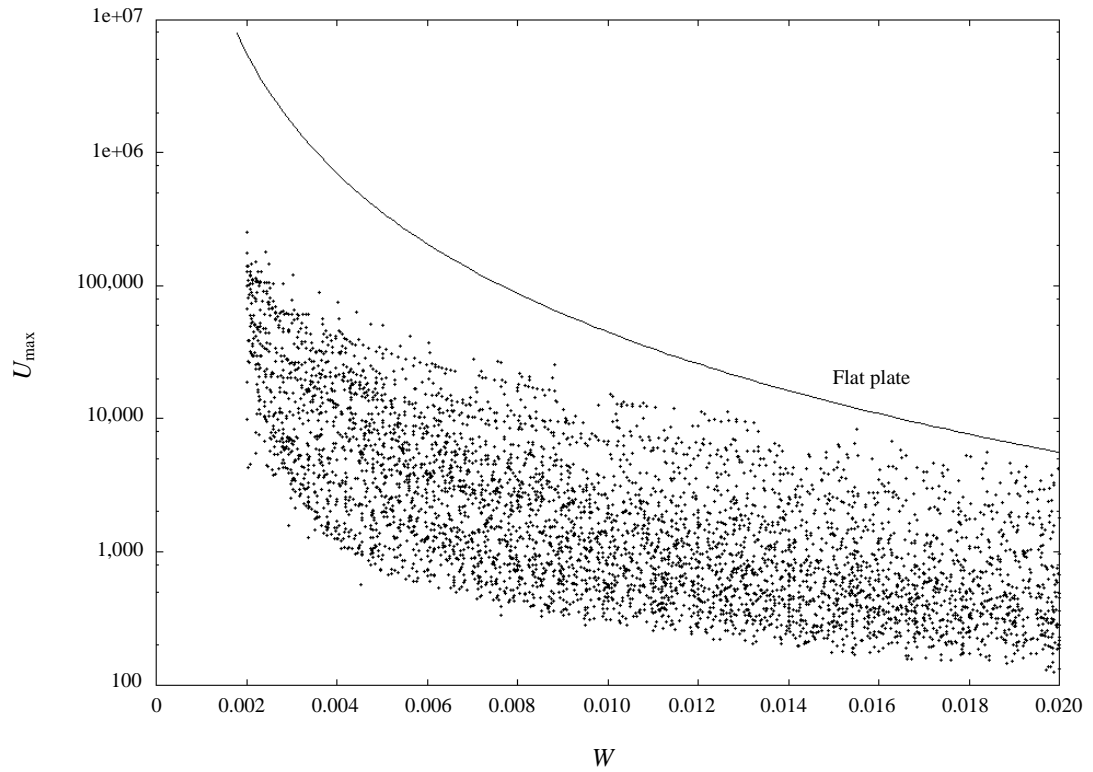


Figure 6.10b Maximum deflection of the trial designs plotted against their weight. The solid line represents the variation of the maximum deflection of a flat plate with weight.

6.3 Data analysis

In this stage robustness analysis is performed to obtain SNR with respect to both the objective functions. Those SNR together with the two objective functions are taken to be the four design objectives. Upon observation of the objective function space, performance criteria are set up and a feasible design set is selected. Subsequently, robust-optimum solutions are extracted from the feasible design set. Finally all the information is compiled into design rules. The details of each step are presented next.

6.3.1 Robustness analysis

In the previous section, we have conducted numerical experiments on 4,500 trial designs. This information can be reused in robustness analysis. Since the design space is filled with trial design; for each trial design we can gather the neighboring designs to use in computing SNR . In order to gather the neighboring designs, we assume that internal noise can occur to the design condition, which makes the design move away from the original design point. Consider a design space in Fig. 6.11 and let r_{ij} be the distance from the neighboring design j to the original design i . This distance can be computed from the following formula;

$$r_{ij} = \sqrt{(\mathbf{T}_j - \mathbf{T}_i)^2 + (\mathbf{P}_j - \mathbf{P}_i)^2 + (\mathbf{H}_j - \mathbf{H}_i)^2} \quad (6.16)$$

where \mathbf{T} , \mathbf{P} and \mathbf{H} are the normalized form of the non-dimensional variables, T , P and H , such that the maximum value of each variables is one and the minimum value is zero, i.e. $\mathbf{T} = (T - T_{\min}) / (T_{\max} - T_{\min})$. We also obtain \mathbf{W} , the normalized form of W , by the same way.

Given that R is the neighborhood radius that is caused by noise, design j can be considered as the neighbor of design i if both of the following conditions are satisfied:

- (1) $r_{ij} \leq R$
- (2) $|\mathbf{W}_i - \mathbf{W}_j| \leq R$

Note that the shape of the corrugation, Γ , is not used in computing the neighborhood. This is because we do not wish to limit the shape to small perturbations and instead take all shapes corresponding to Γ between 0 and 1. Once the neighbor designs are gathered, the values of their objective functions are used to determine SNR by Eq. 5.2 for natural frequency and Eq. 5.1 for maximum deflection.

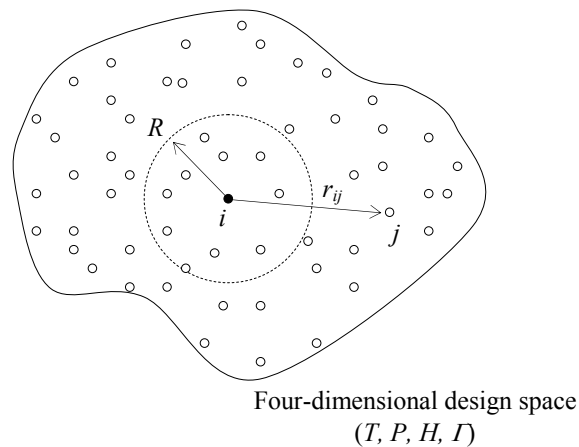


Figure 6.11 Neighborhood of a design.

Using this method with $R = 10\%$, most of the trial designs have more than 25 neighboring points. We are able to check for robustness of all the 4,500 trial designs. The results are shown in Fig. 6.12a and b.

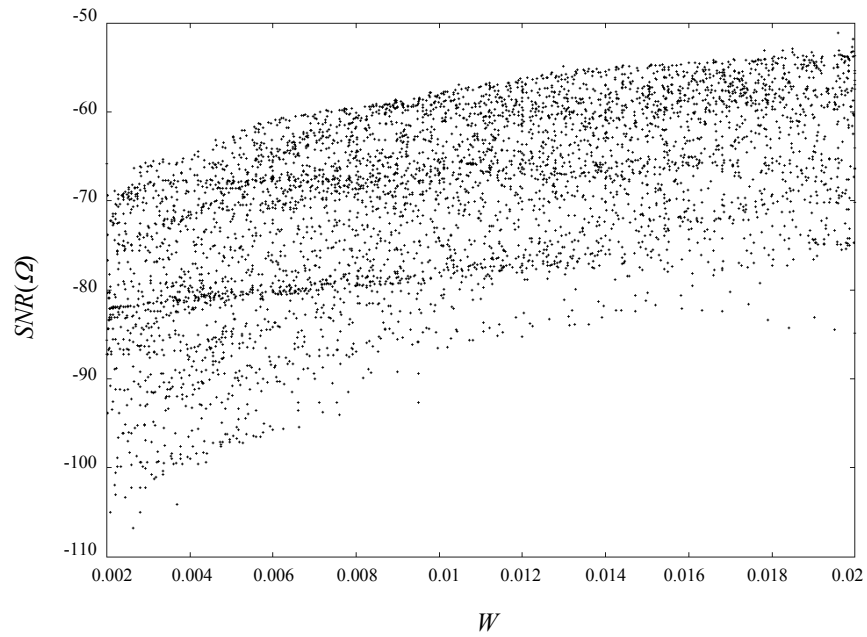


Figure 6.12a Signal-to-noise ratio with respect to the natural frequency of the trial designs.

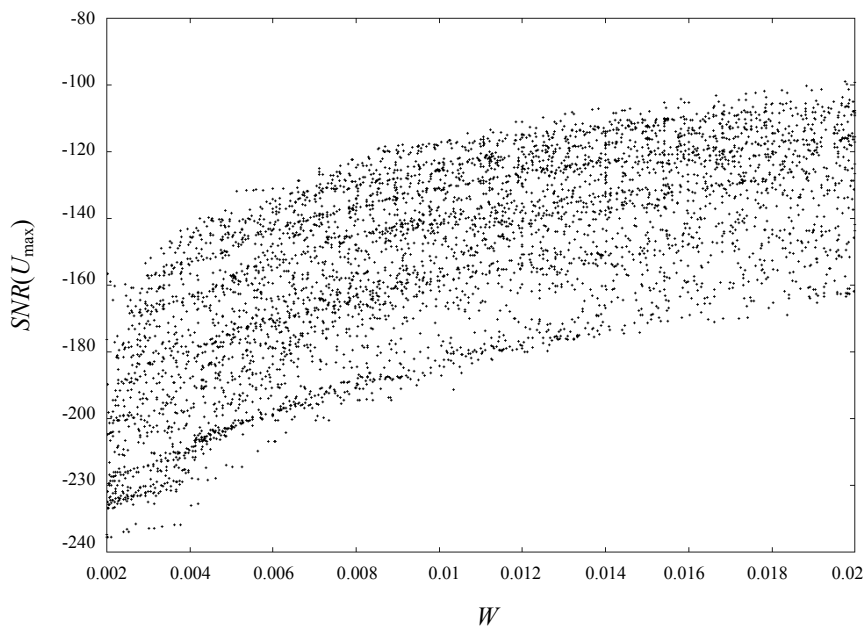


Figure 6.12b Signal-to-noise ratio with respect to the maximum deflection of the trial designs.

6.3.2 Feasible solutions

At this stage we have four objectives to consider, which are maximization of Ω , minimization of U_{\max} , maximization of $SNR(\Omega)$ and maximization of $SNR(U_{\max})$. To select feasible designs from the trial designs we first observe the objective function space in Fig. 6.10a and b and Fig. 6.12a and b. Boundary points are extracted from each figure. Parts of the boundary points are used to form upper and lower envelopes. The envelopes are made smooth and continuous by cubic interpolation splines. We then use these envelopes to rescale the objective function and apply the min-max method (described in section 3.2.2) to form a new quantity called the feasibility index. The details of the process are shown next with the use of an example for natural frequency objective.

Step 1. Boundary extraction

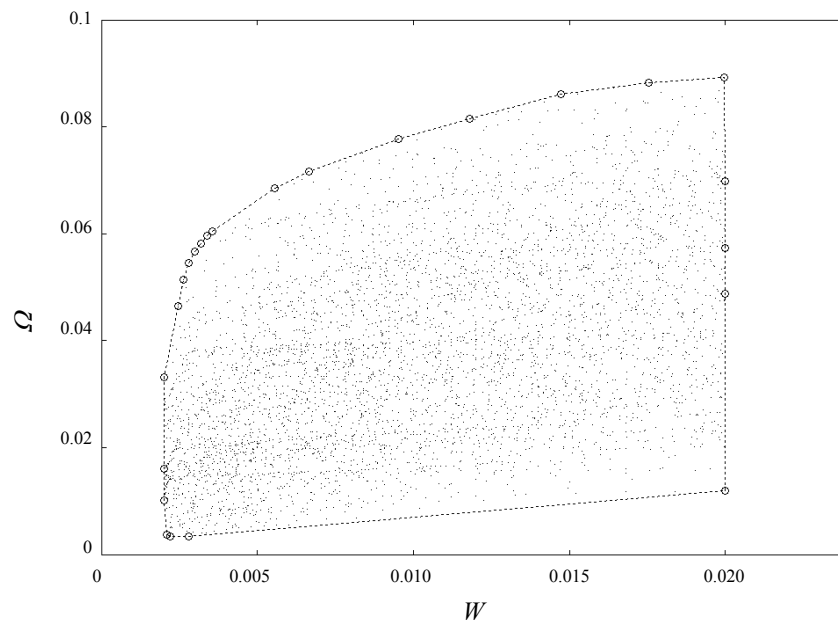


Figure 6.13 Convex hull of a plot between natural frequency and weight.

A convex hull method (O'Rourke, 1993) is used to find the boundary of the data points. The result is shown in Fig. 6.13, where open circles are the boundary points that form a convex hull.

Step 2 Determining the feasible region

The upper part of the boundary in Fig 6.13, which we call “upper envelope”, corresponds to the best design. The upper envelop is made smooth and continuous by a cubic interpolation spline (shown as \mathbf{B}_0 in Fig. 6.14). The worst design boundary or the so called “lower envelope” is obtained from the natural frequency of a flat plate (given in Eq. 6.15 and shown as \mathbf{B}_1 in Fig. 6.14). The objective function space is now bounded with upper and lower envelopes as shown in Fig. 6.14.

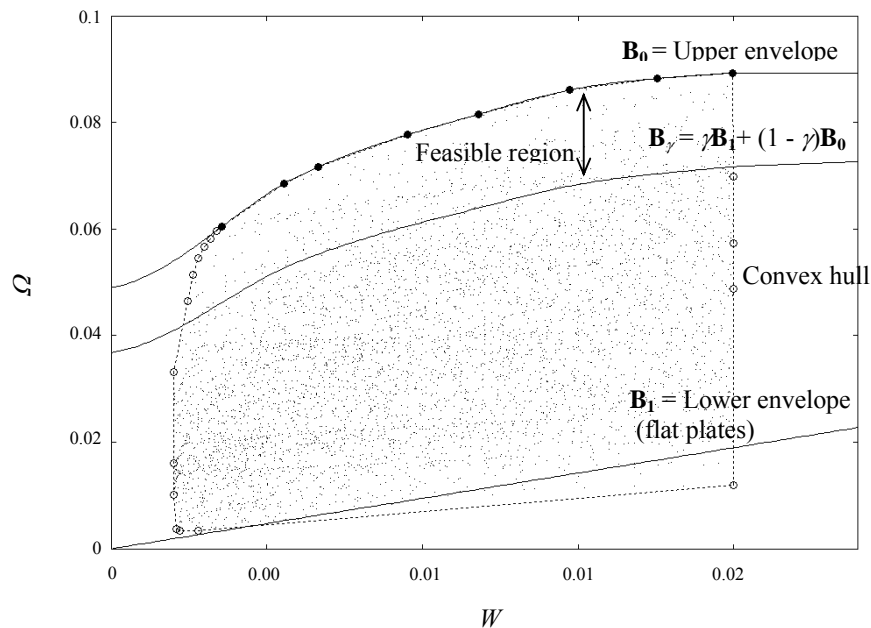


Figure 6.14 Graphical representation of the feasible region in the $\Omega - W$ objective function space.

The line \mathbf{B}_γ determined by the parameter γ (γ ranges between zero and one) denotes the feasible region.

Step 3. Transforming the objective function

Once the upper and lower envelopes are set, we transform the objective function Ω into Φ^1 by setting the value of Φ^1 at \mathbf{B}_1 to be one and \mathbf{B}_0 to be zero. Then the value Φ_i^1 of the design i is given by a linear interpolation between \mathbf{B}_1 and \mathbf{B}_0 ,

$$\Phi_i^1 = \frac{\Omega_i - \Omega_{\mathbf{B}_0}}{\Omega_{\mathbf{B}_1} - \Omega_{\mathbf{B}_0}}. \quad (6.17)$$

In the above, all the Ω are for the same weight as the design i . After this transformation we can plot the new objective function, Φ^1 as shown in Fig. 6.15. The feasible region is then $\Phi^1 < \gamma$.

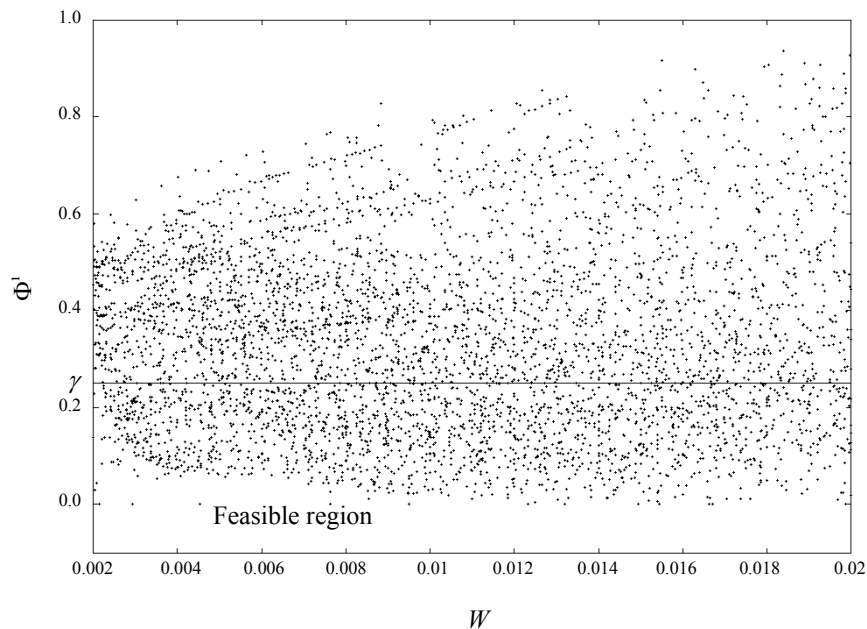


Figure 6.15 Transformed natural frequency vs. weight.

Step 4. Apply min-max method

The example shown in step 1 to step 3 is for transforming just the natural frequency. We need to repeat these steps to transform the other three objective functions. A modification is needed for objective functions $SNR(\Omega)$ and $SNR(U_{\max})$. For each of these objectives, the lower envelope is taken to be the lower boundary instead of the performance of a flat plate because we do not have SNR of a flat plate.

Once all the objectives are transformed we rewrite them as

Transformed natural frequency, Φ^1

Transformed maximum deflection, Φ^2

Transformed $SNR(\Omega)$, Φ^3

Transformed $SNR(U_{\max})$, Φ^4

The new quantity called feasibility index is set up using a min-max approach as

$$\Phi = \max(\Phi^1, \Phi^2, \Phi^3, \Phi^4) \quad (6.18)$$

By using the above index we can set up the feasible region using only one common upper limit of Φ and screen out the feasible designs. Figure 6.16 shows the increase in the number of feasible solutions as the limit γ is increased. We choose $\gamma = 0.25$ which leads to a total of 292 feasible solutions (6.5% of the total number of trial designs). Figures 6.17a to c show the natural frequency, maximum deflection and feasibility index of the feasible solutions (filled circles) in comparison with the trial designs (small dots).

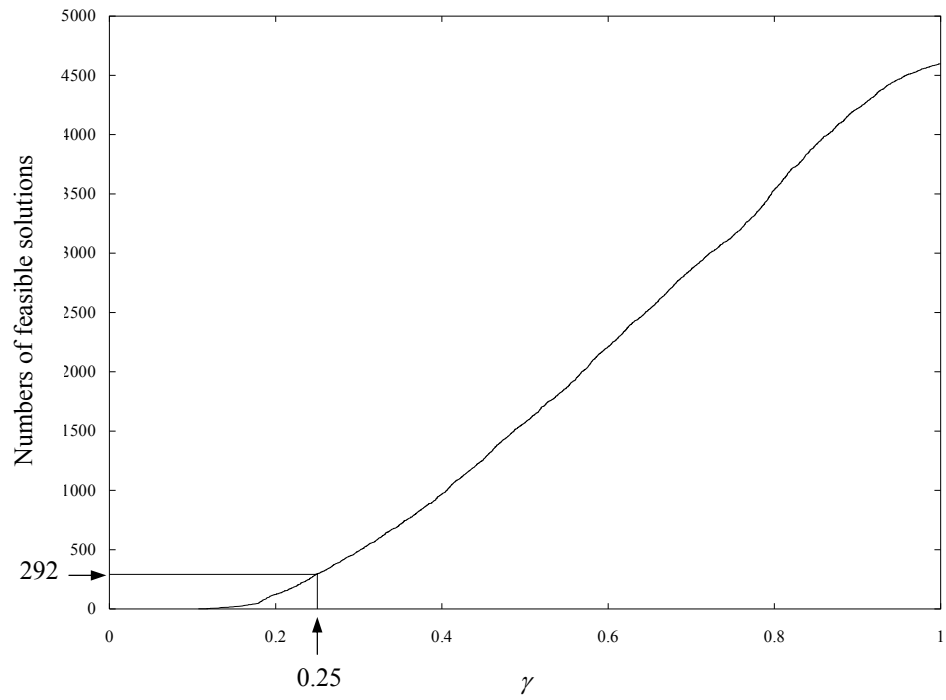


Figure 6.16 Numbers of feasible solutions vs. upper limit of the feasibility index.

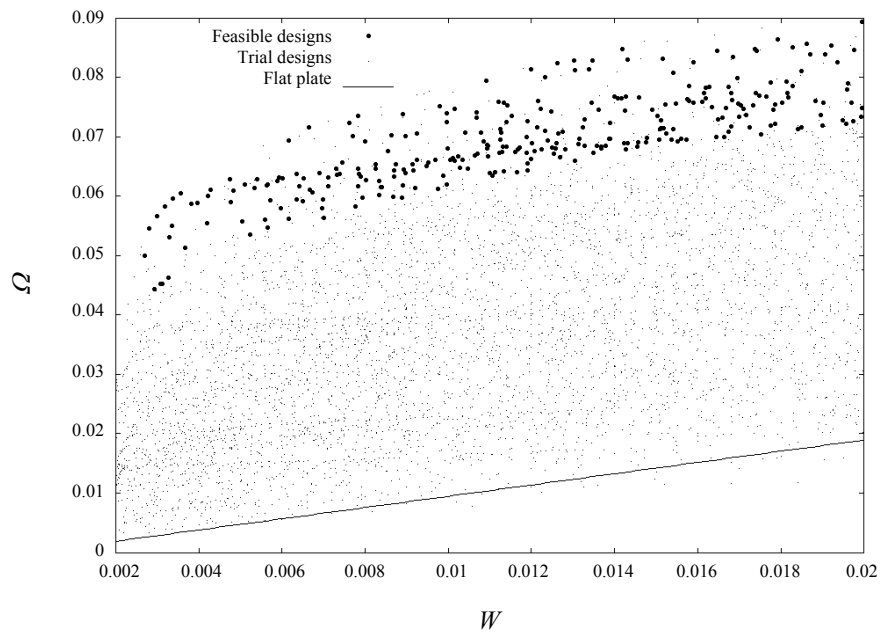


Figure 6.17a Natural frequency vs weight of the feasible designs in comparison with the trial designs and flat plates.

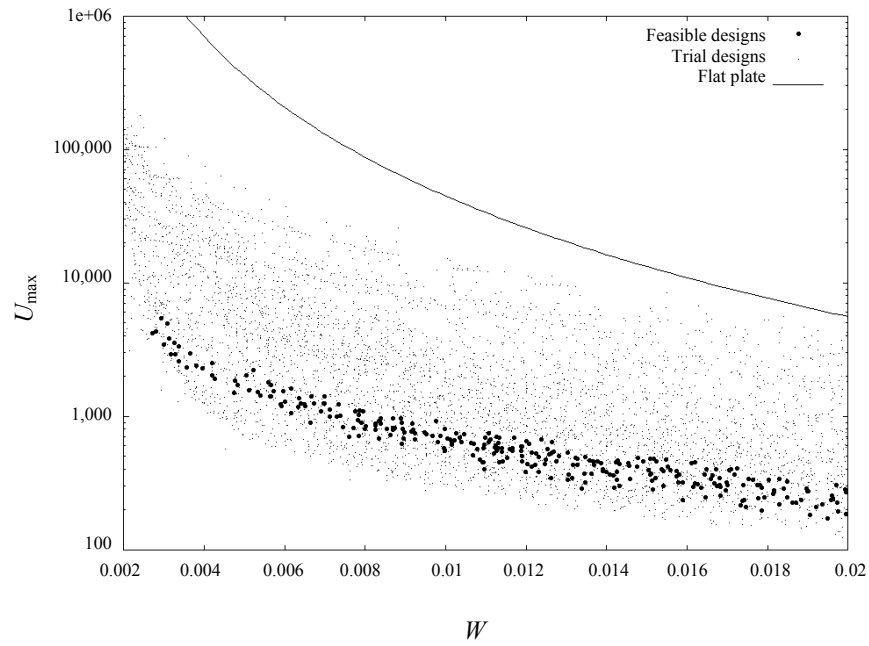


Figure 6.17b Maximum deflection vs weight of the feasible designs in comparison with the trial designs and flat plates.

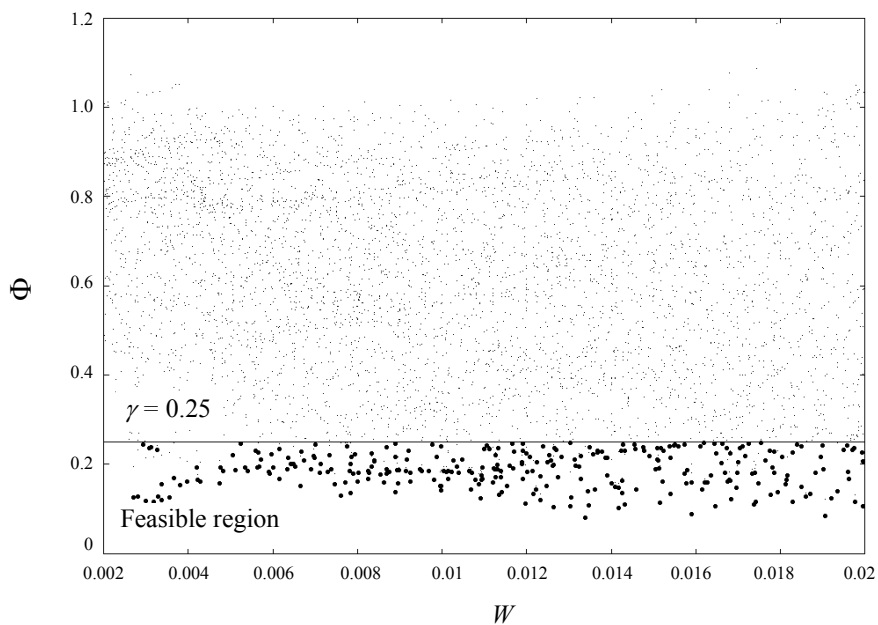


Figure 6.17c Feasibility index vs weight. Feasible designs are represented with filled circles. Small dots are trial designs.

6.3.3 Pareto robust-optimum solutions

To obtain the robust-optimum designs, it becomes necessary to drop the last two objective functions, $SNR(U_{\max})$: Φ^3 and $SNR(\Omega)$: Φ^4 . This is because the SNR that are computed using neighboring samples are not accurate enough to use for finding the Pareto solution (see discussion). And since the feasible designs obtained in the previous section are considered relatively robust already, we can now focus on the two original objectives, natural frequency and maximum deflection. We pursue the Pareto robust-optimum design by trying three different objectives which are:

Pareto set no. 1 (PS1): Maximizing natural frequency

Pareto set no. 2 (PS2): Minimizing maximum deflection

Pareto set no. 3 (PS3): Minimizing min-max objective function f where

$$f = \max (\Phi^1, \Phi^2). \quad (6.19)$$

To obtain each Pareto set, we set up the boundary searches in two-dimensional spaces of $\Omega - W$, $U_{\max} - W$ and $f - W$. The results are compared in Fig. 6.18a to c.

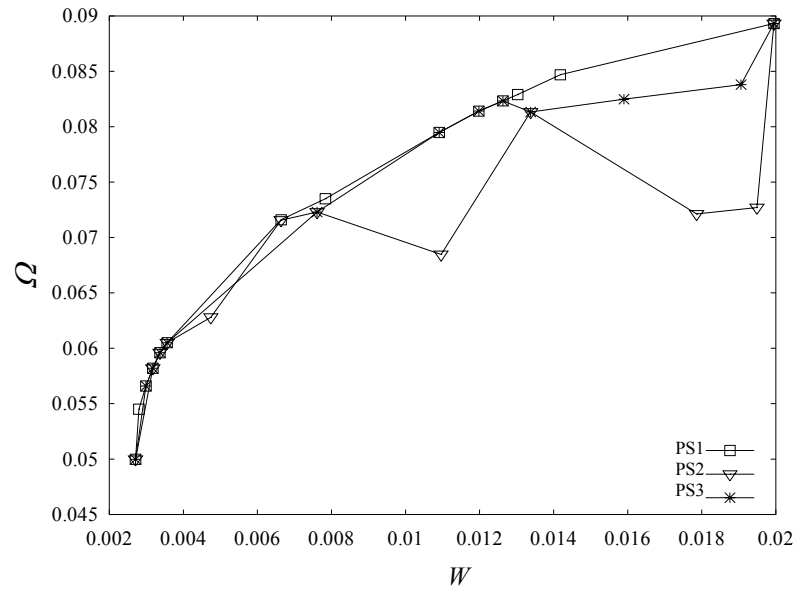


Figure 6.18a Natural frequency of Pareto sets number 1, 2 and 3.

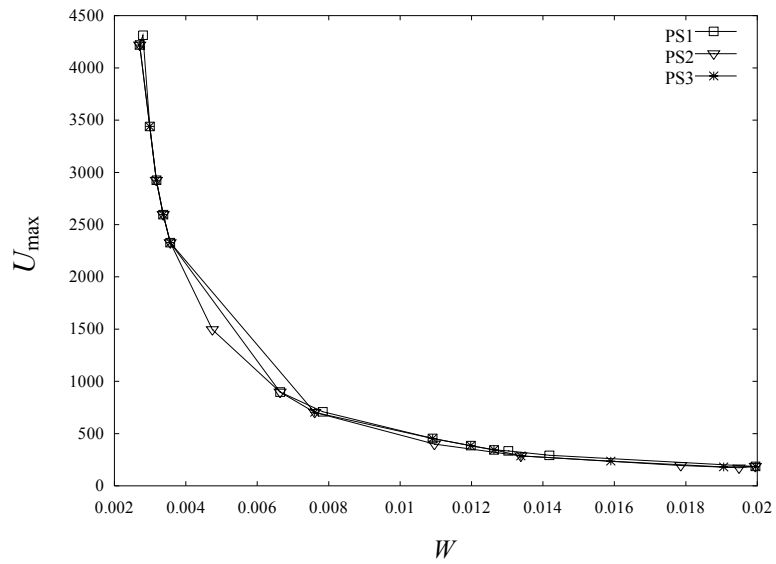


Figure 6.18b Maximum deflection of Pareto sets number 1, 2 and 3.

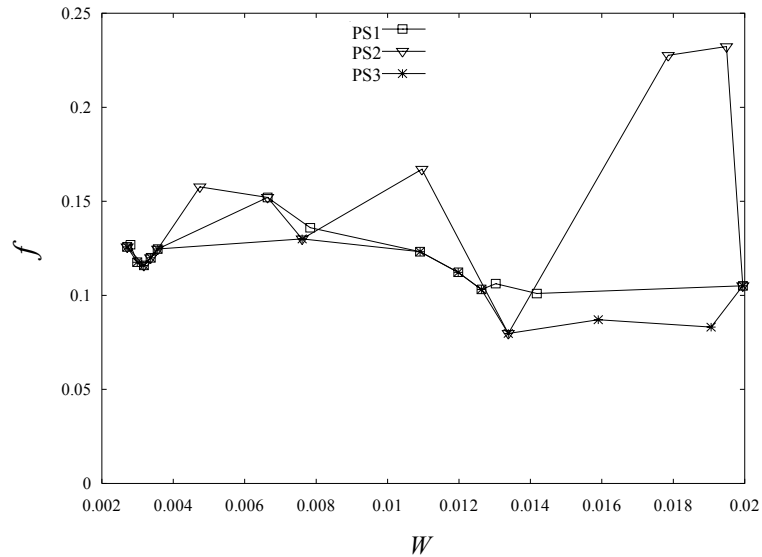
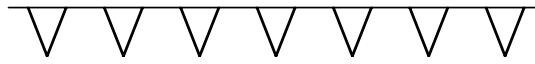
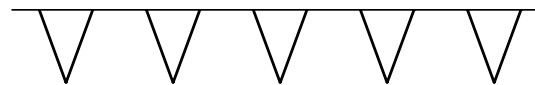
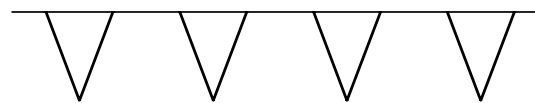


Figure 6.18c Min-max objective function of Pareto sets number 1, 2 and 3.

To select the best design set, we visually rank the performance of the three design sets from Fig. 6.18a to c and set up Table 6.2. From Fig. 6.18b, PS1 and PS3 have very close maximum deflection; hence the same rank is given in Table 6.2 for both design sets. Although PS1 and PS3 have the same overall rank, we select PS1 as the Pareto robust-optimum solution set because PS1 have the highest natural frequency among the feasible designs while having the maximum deflection close to that of PS3. Figure 6.19 shows cross-sectional geometry of the robust-optimum designs. In the next section, the characteristics of the design in PS1 are extracted and design rules are developed.

Table 6.2 Comparison of Pareto set.

Pareto set Number	Ranked by			Overall (add the three ranking)
	Natural frequency	Maximum deflection	Min-max objective function	
1	1	2	2	5
2	3	1	3	7
3	2	2	1	5

(a) $W = 0.003$ (b) $W = 0.01$ (c) $W = 0.02$ **Figure 6.19** Crosssectional geometry of robust-optimum corrugated panel designs.

6.3.4 Design rules for robust-optimum design

From the solution set obtained in 6.3.3, we observe the characteristic of the robust-optimum designs by making the plots between design variables and weight as shown in Fig. 6.20a to d. In those figures, small dots represent the trial designs, circles represent the feasible designs, filled squares connected with dashed lines are the robust-optimum designs and solid lines are the estimation of robust-optimum design variables. By least square fittings of the data set PS1, the relationships between the robust-optimum design variables and weight can be estimated by following formulas:

$$T = 0.31W \quad (6.20a)$$

$$P = 0.058 + 14W - 270W^2 \quad (6.20b)$$

$$H = 0.064 + 10W - 220W^2 \quad (6.20c)$$

$$\Gamma = 0 \text{ (triangle)} \quad (6.20d)$$

We generate a set of robust-optimum designs following the above formulas and solve for natural frequency and maximum deflection and also compute the feasibility index. The results are shown in Fig. 6.21a and c. From those results, least square fittings is performed to estimate the relationship between natural frequency and weight (Eq. 6.20e) and the relationship between maximum deflection and weight (Eq. 6.20f) of the robust-optimum designs. The formulas in Eq. 6.20a to f are the proposed design rules.

$$\Omega = 0.041 + 4.9W - 130W^2 \quad (6.20e)$$

$$U_{\max} = 0.54W^{-1.5} \quad (6.20f)$$

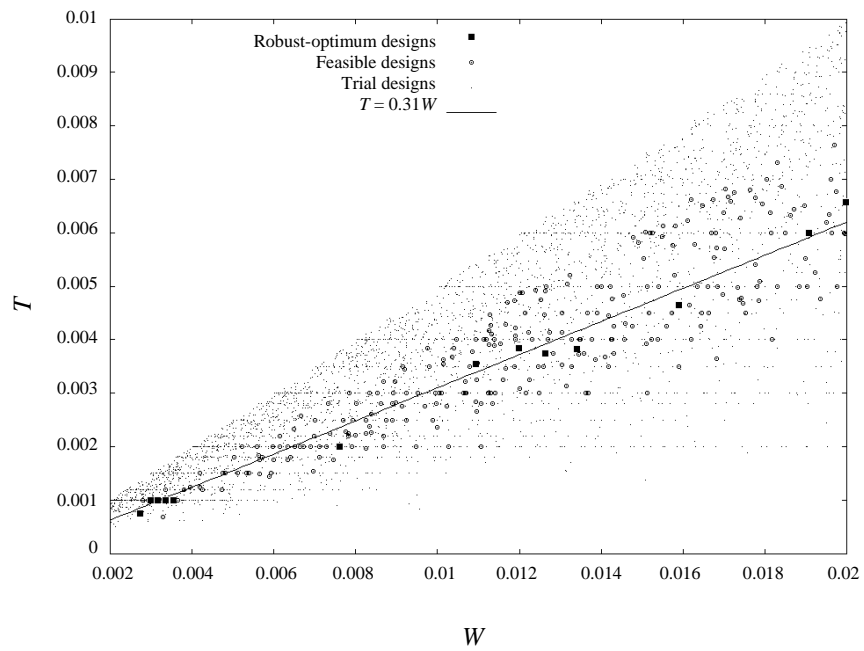


Figure 6.20a Thickness of robust-optimum designs compared to the thickness of the feasible designs and the trial designs.

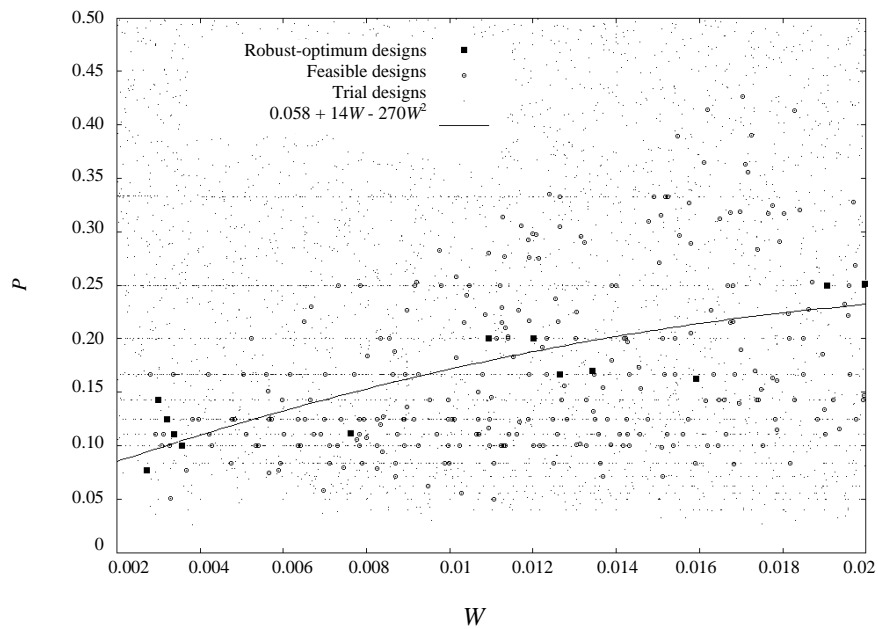


Figure 6.20b Pitch of robust-optimum designs compared to the pitch of the feasible designs and the trial designs.

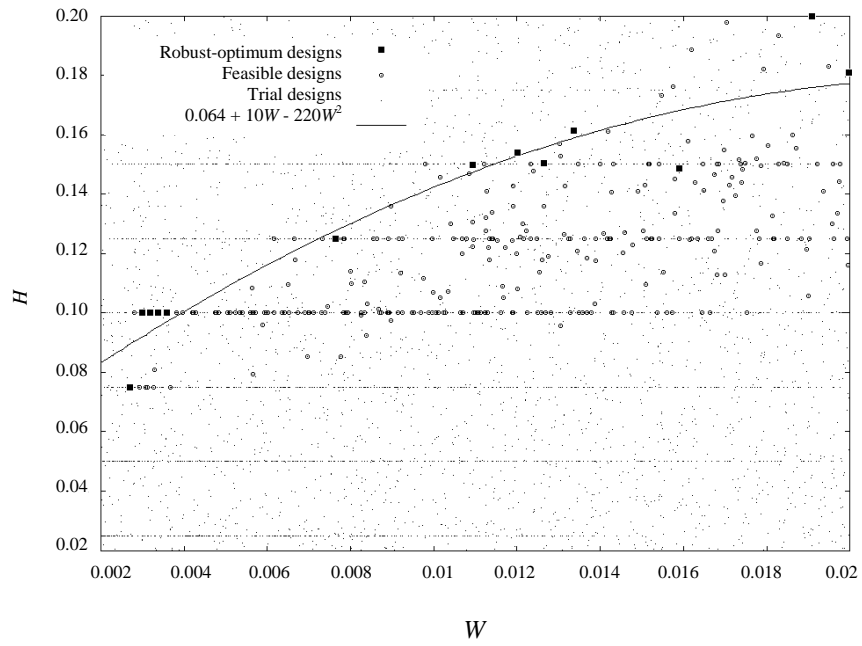


Figure 6.20c Height of robust-optimum designs compared to the height of the feasible designs and the trial designs.

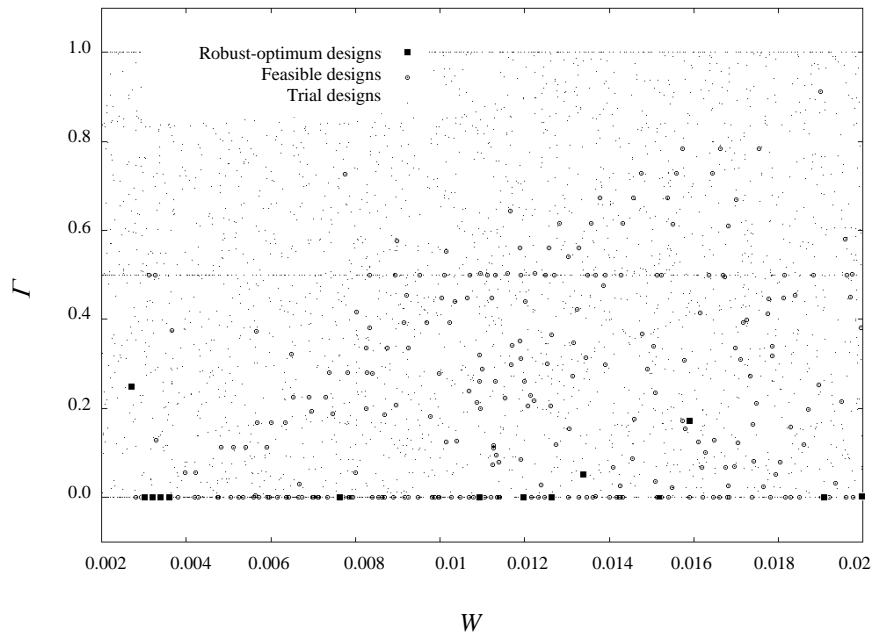


Figure 6.20d Shape of robust-optimum designs compared to the shape of the feasible designs and the trial designs.

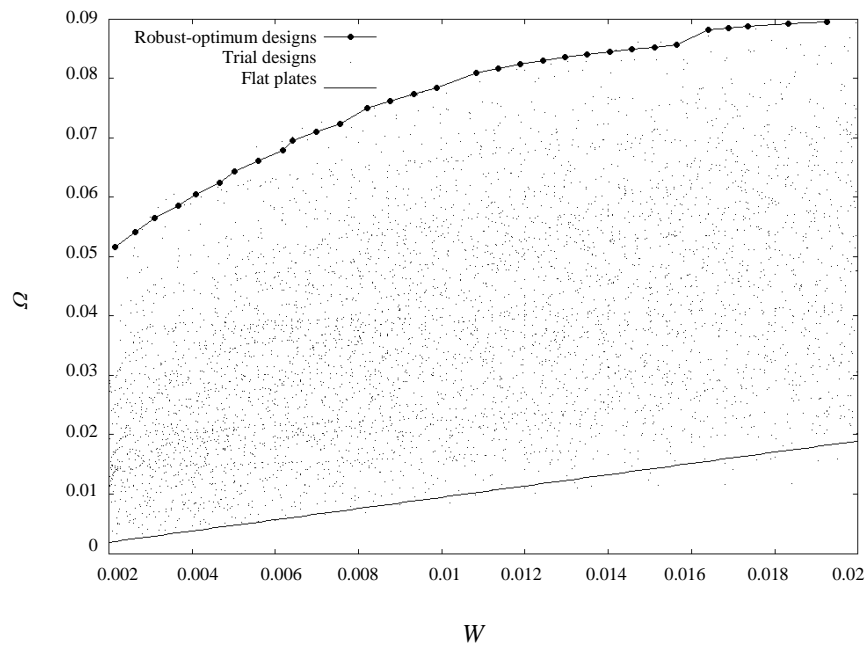


Figure 6.21a Natural frequency of robust-optimum designs generated using the proposed design rules compared with the natural frequency of the trial designs and flat plates.

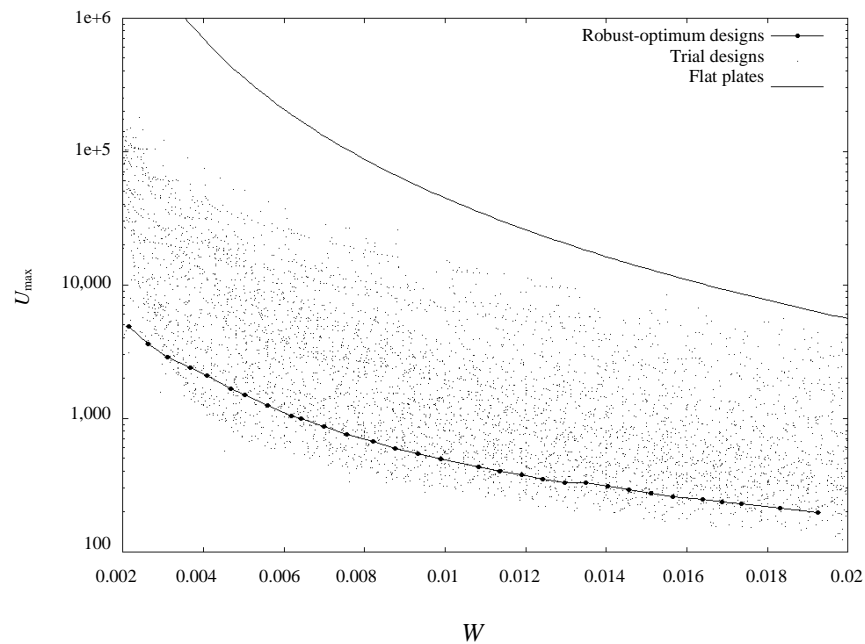


Figure 6.21b Maximum deflection of the robust-optimum designs generated using the proposed design rules compared with the maximum deflection of the trial designs and flat plates.

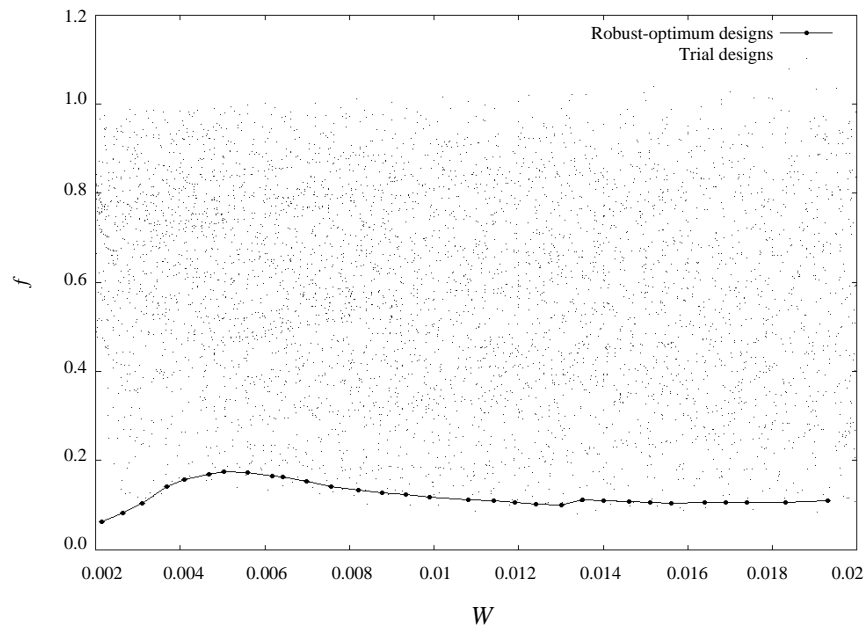


Figure 6.21c Min-max objective function of the robust-optimum designs generated using the proposed design rules compared with the min-max objective function of the trial designs.

In practice, there may exist specific geometric constraints, e.g. a height constraint because of space considerations. The robust-optimum designs under such constraints can be obtained by screening the trial designs in section 6.2 according to the constraints and following the same process as in 6.3.2. We perform such a process for height constraints of $H \leq 0.1$, $H \leq 0.075$ and $H \leq 0.05$. The design rules for all these cases are summarized in Table 6.3. For additional clarity, graphical representation of the relationships in Table 6.3 is shown in Fig. 6.22a to f.

Table 6.3 Design rules for robust-optimum corrugated panel structures.*

		Unconstrained	$H \leq 0.1$ **	$H \leq 0.075$	$H \leq 0.05$
Robust-optimum design variables	T	$0.31W$	$0.25W$	$0.25W$	$0.38W$
	P	$0.058 + 14W - 270W^2$	0.1	0.08	$6.5W + 0.037$
	H	$0.064 + 10W - 220W^2$	0.1	0.075	0.05
	Γ	0	$\text{Min}(56W - 0.2, 1)$	$\text{Min}(120W - 0.07, 1)$	1
Ω		$0.041 + 4.9W - 130W^2$	$0.06 + 0.59W$	$0.05 + 0.43W$	$0.038 + 0.18W$
U_{\max}		$0.54W^{-1.5}$	$(0.0024 + W)^{-1.5}$	$(0.0009 + 1.1W - 15W^2)^{-1.5}$	$(0.0013 + 0.55W - 5.4W^2)^{-1.5}$

Notes:

* This table is only applicable to isotropic materials with $\nu = 0.29$ and a weight range of $0.002 \leq W \leq 0.02$. Formulas for Ω and U_{\max} only provide a rough estimate.

** Use only when the formulas for unconstrained case fails to satisfy the height constraint

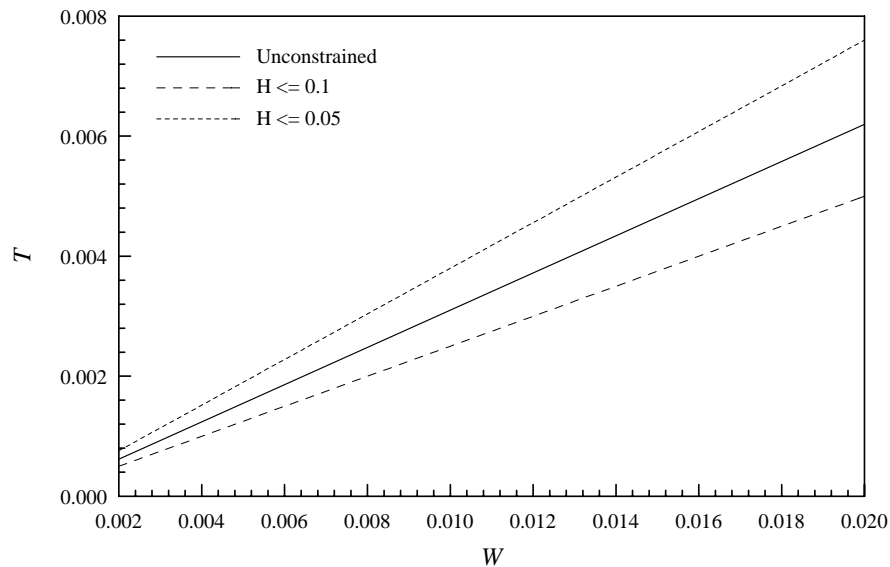


Figure 6.22a Graphical representation of the relationships between the thickness and weight of the robust-optimum corrugated panel structures according to the design rules in Table 6.3.

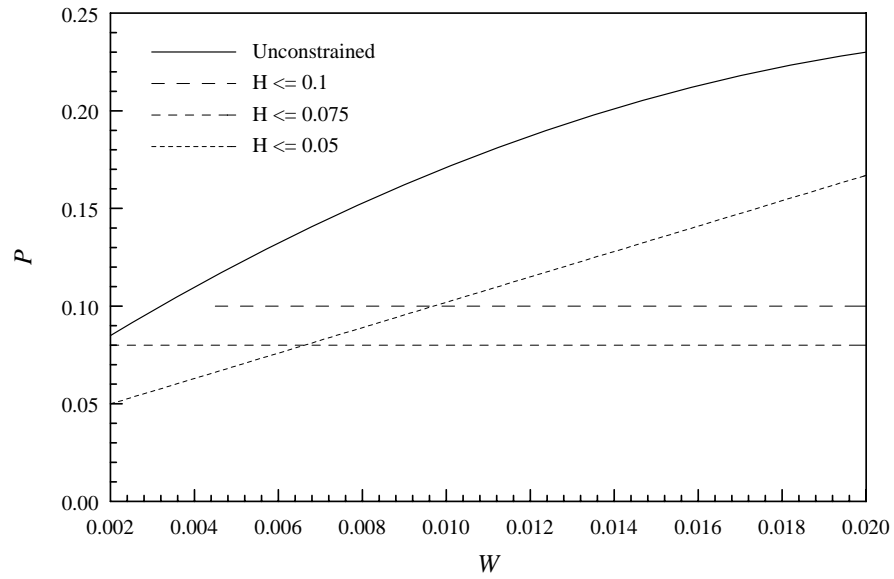


Figure 6.22b Graphical representation of the relationships between the pitch and weight of the robust-optimum corrugated panel structures according to the design rules in Table 6.3.

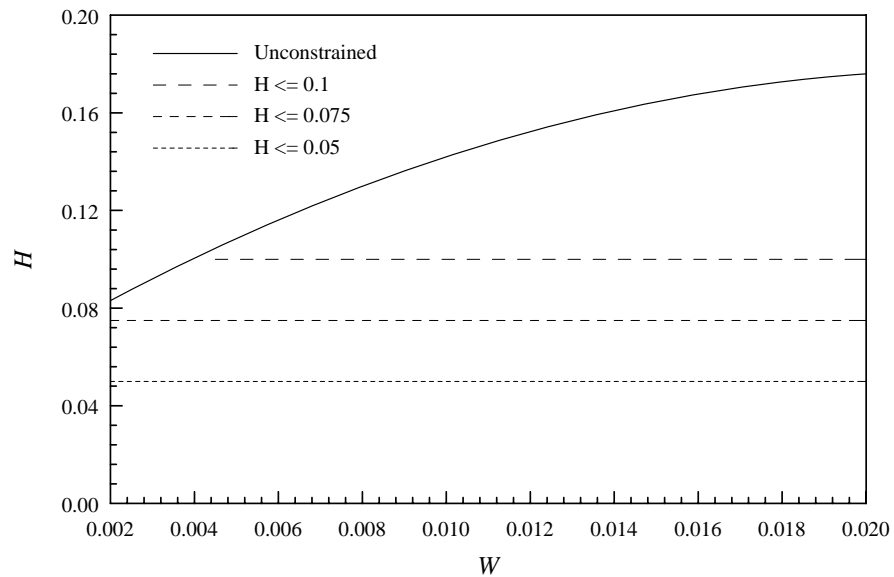


Figure 6.22c Graphical representation of the relationships between the height and weight of the robust-optimum corrugated panel structures according to the design rules in Table 6.3.

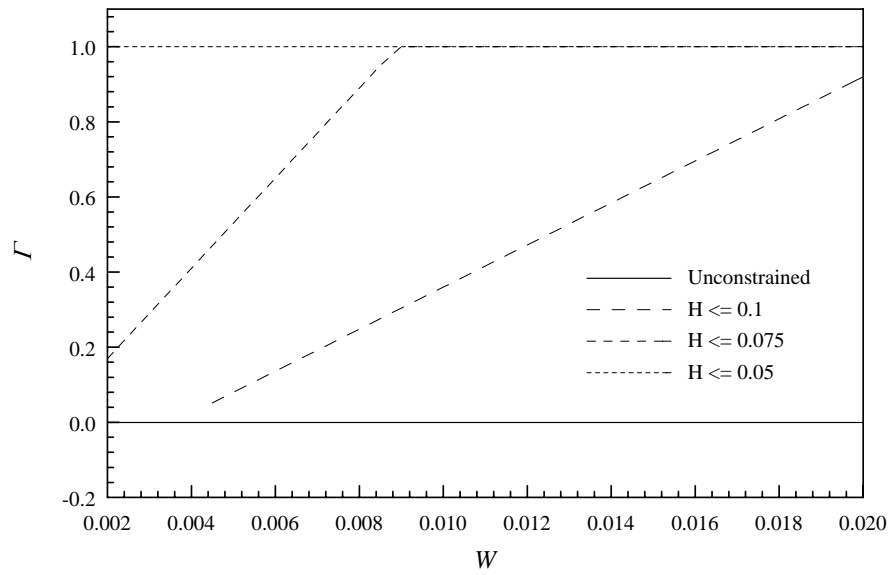


Figure 6.22d Graphical representation of the relationships between the shape and weight of the robust-optimum corrugated panel structures according to the design rules in Table 6.3.

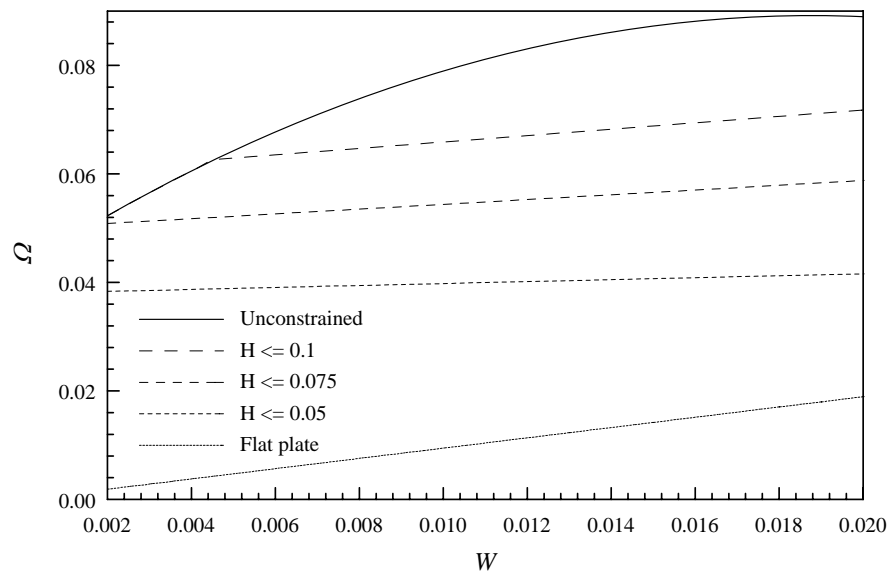


Figure 6.22e Graphical representation of the relationships between the natural frequency and weight of the robust-optimum corrugated panel structures according to the design rules in Table 6.3.

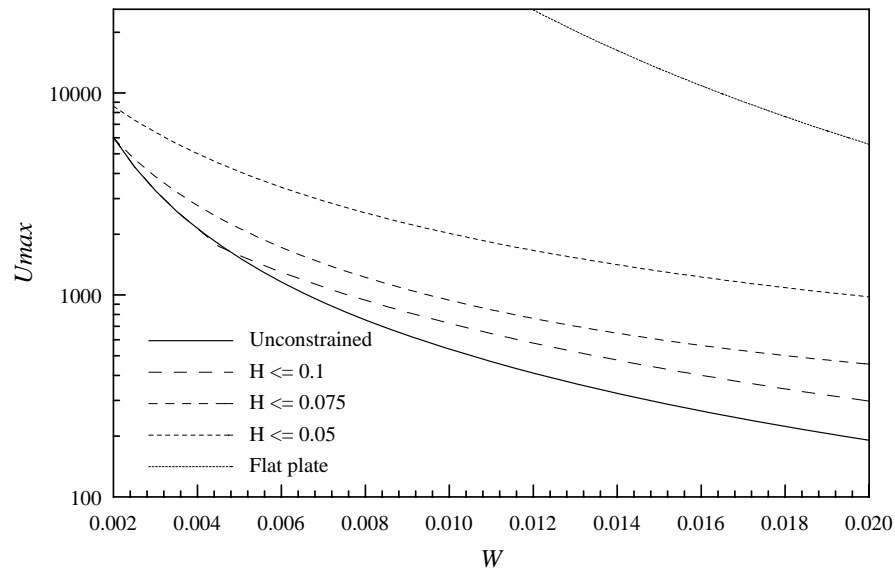


Figure 6.22f Graphical representation of the relationships between the maximum deflection and weight of the robust-optimum corrugated panel structures according to the design rules in Table 6.3.

Note that the design rules in Table 6.3 do not provide an explicit relationship between the design variables and weight since weight also a function of the four design variables hence the design rules must be used in a recursive manner. For example, designers would select weight, W^* , first then use W^* in Eq. 6.21a to c (first column of Table 6.3) to obtain T , P and H . Finally the actual weight, W , is calculated using T , P and H (the actual weight will turn out to be close to the selected weight). A practical example given in the next section demonstrates the use of design rules.

6.4 Example problems

6.4.1 Corrugated panel structure with deflection constraint

Suppose that one wants to design the square corrugated panel structure of width 1 meter to sustain a uniformly distributed load $q = 20 \text{ kN/m}^2$. The maximum allowable deflection is 0.1 mm. The material is isotropic steel with $E = 203 \text{ Gpa}$, $\nu = 0.29$ and $\rho = 7.85 \times 10^3 \text{ kg/m}^3$. To find such a design, first we need to determine the non-dimensional form of from the maximum deflection (using Eq. 6.9) which is $U_{\max} = 10^3$. Then we use U_{\max} to solve Eq. 6.20f and obtain the estimated weight, which is $W^* = 0.0066$. From W^* , we can obtain the values of robust-optimum design variables from Eq. 6.20a to d (also shown in Table 6.3), which are: $T = 0.002$, $P = 0.14$, $H = 0.12$ and the shape Γ which is triangular. Using these values of T , P , H and Γ , we solve for the actual values of weight, which is $W = 0.0065$. The natural frequency and maximum deflection are then obtained using I-DEAS, they are $\Omega = 0.07$ and $U_{\max} = 920$. In actual units, the robust-optimum design is; thickness = 2 mm., pitch = 14 cm., height = 12 cm., weight = 51 kg, natural frequency = 350 Hz and a maximum deflection = 0.09 mm. The cross-section of the structure is shown in Fig. 6.23.

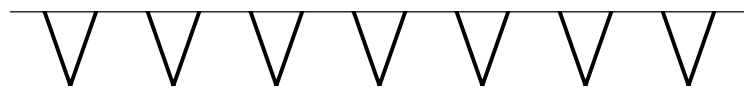


Figure 6.23 Cross-sectional wire-frame geometry of a robust-optimum corrugated panel structure for $U_{\max} = 10^3$.

6.4.2 Corrugated panel structure with deflection and height constraint

In this section the design problem of the earlier section is demonstrated with an imposed height constraint. If a height constraint of 75 mm. is imposed then the robust-optimum design with $H = 0.12$ does not satisfy the height constraint. In this case the formulas in the third column of Table 6.3 must be used instead. For $U_{\max} = 10^3$, we solve the estimated weight using the equation in the last row and obtain $W^* = 0.0095$. Then the design variables can be computed as $T = 0.0024$, $P = 0.08$, $H = 0.075$ and $\Gamma = 1$.

We now solve for the actual weight, which is $W = 0.0091$ and obtain $\Omega = 0.053$ and $U_{\max} = 990$ using I-DEAS. The robust-optimum design in physical units is; thickness = 2.4 mm., pitch = 8 cm., height = 7.5 cm., weight = 75 kg, natural frequency = 270 Hz and maximum deflection = 0.1 mm. The cross-section of the structure is shown in Fig. 6.24. Note that due to the height constraint, the weight in this case is larger than the previous case and the shape is different as well.



Figure 6.24 Cross-sectional wire-frame geometry of a robust-optimum corrugated panel structure for $U_{\max} = 10^3$ and $H = 0.075$

6.5 Discussion

6.5.1 Sensitivity analysis

Second order response functions are fitted to the 292 feasible designs in order to approximate the relative effect of each design variable on natural frequency, maximum deflection and weight of the feasible designs. Equation 6.21 shows the form of the second order response function to be.

$$\begin{aligned}
 F = & c_1 + c_2\mathbf{T} + c_3\mathbf{\Gamma} + c_4\mathbf{P} + c_5\mathbf{H} \\
 & + c_6\mathbf{T}^2 + c_7\mathbf{\Gamma}^2 + c_8\mathbf{P}^2 + c_9\mathbf{H}^2 \\
 & + c_{10}\mathbf{TT} + c_{11}\mathbf{TP} + c_{12}\mathbf{TH} + c_{13}\mathbf{\Gamma P} + c_{14}\mathbf{\Gamma H} + c_{15}\mathbf{PH}
 \end{aligned} \tag{6.21}$$

where F represents the dependent functions (W , Ω or U); \mathbf{T} , $\mathbf{\Gamma}$, \mathbf{P} and \mathbf{H} are in normalized forms, i.e. $\mathbf{T} = (T - T_{\min})/(T_{\max} - T_{\min})$. Coefficients c_i are obtained using least square fitting. To obtain a better fitting for maximum deflection, a new dependent variable letting $F = \log_{10}(U_{\max})$ is used instead of U_{\max} . Although the response functions do not accurately predict the relationships, the coefficients in the functions do provide reasonable approximation of the relative effects of design variables. The results are shown in Table 6.4.

Table 6.4 Coefficients of the response functions of the feasible designs.

	I	Variable	$F=W$	$F=\Omega$	$F=\log_{10}(U)$
c_0	1	1	0.00354	0.0467	3.52
First order, c_i/c_1	2	T	<u>6.89</u>	0.0682	<u>-0.568</u>
	3	Γ	0.0220	0.698	-0.0623
	4	P	-4.37	-0.704	0.402
	5	H	1.90	<u>2.18</u>	-0.460
Second order, c_i/c_1	6	T^2	-0.325	-0.814	<u>0.355</u>
	7	Γ^2	0.0542	-0.896	0.0201
	8	P^2	<u>7.34</u>	-0.231	-0.00606
	9	H^2	-0.632	<u>-2.30</u>	0.112
Mixed, c_i/c_1	10	$T\Gamma$	0.918	1.76	0.0340
	11	TP	<u>-5.75</u>	-0.0351	<u>-0.309</u>
	12	TH	3.64	1.81	0.137
	13	ΓP	-0.165	0.503	-0.0634
	14	ΓH	-0.216	<u>-3.43</u>	-0.0284
	15	PH	-4.34	0.773	0.0828
Average error(%)			2.1	1.7	4.9
Maximum error(%)			16	11	25
Normalization Factor	T_{\min}/T_{\max}		0.000682/ 0.00765		
	$\Gamma_{\min}/\Gamma_{\max}$		0.0/0.912		
	P_{\min}/P_{\max}		0.05/0.426		
	H_{\min}/H_{\max}		0.075/0.2		

Note that the result in Table 6.4 are only valid in the feasible region. The response functions over the total design space would be quite different. The coefficients of the first order terms suggest that height has the largest effect on the natural frequency while thickness has the largest effect on maximum deflection and weight of the structure. Shape of the corrugation has a relatively small overall effect. The second order terms describe the effect of the values of the design variables on robustness. They show that height has the most effect on robustness with respect to natural frequency.

6.5.2 Effect of numbers of samples on *SNR*

In the computation of *SNR* of the trial designs in section 6.3.1, the numbers of neighbor designs used for computation are different from one design to another (most of the design have 10 to 30 neighbors). Figure 6.25 shows the distribution of number of neighbors used in computing *SNR* for the trial designs. It is expected that the values of signal to noise ratios converge with the increasing numbers of neighbors, in order to make comparisons of *SNR* of different designs we assume that numbers of neighbors do not have much effect on the *SNR*.

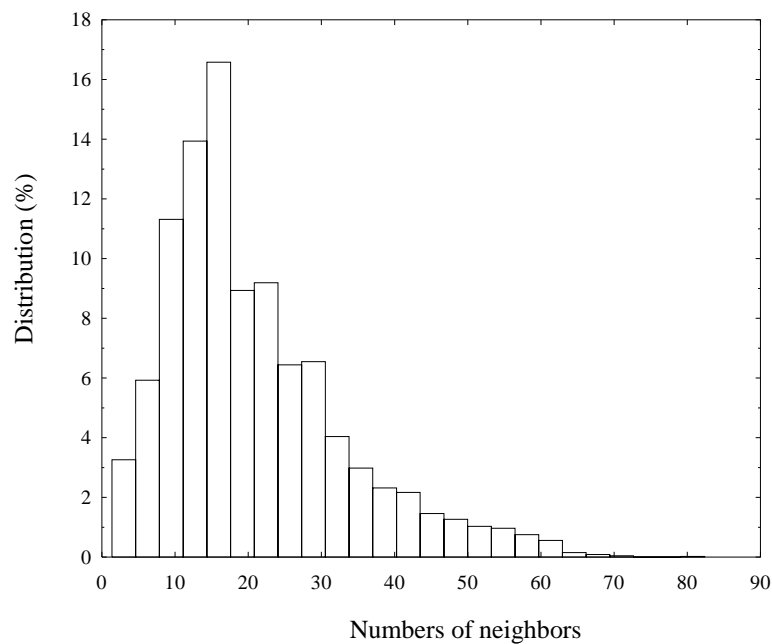


Figure 6.25 Distribution of numbers of samples used to compute *SNR*. Neighborhood radius = 10%.

To verify this assumption, a few designs (with varying numbers of neighbors) are chosen for the convergence study. The result in Fig. 6.26 shows that 25 to 50 neighbor

samples would be required for a good estimate of SNR but as few as twenty-five may be used for a rough estimation. This explains the reason why in section 6.3, we only use SNR can be used to screen out infeasible designs but may not be used to determine robust-optimum designs.

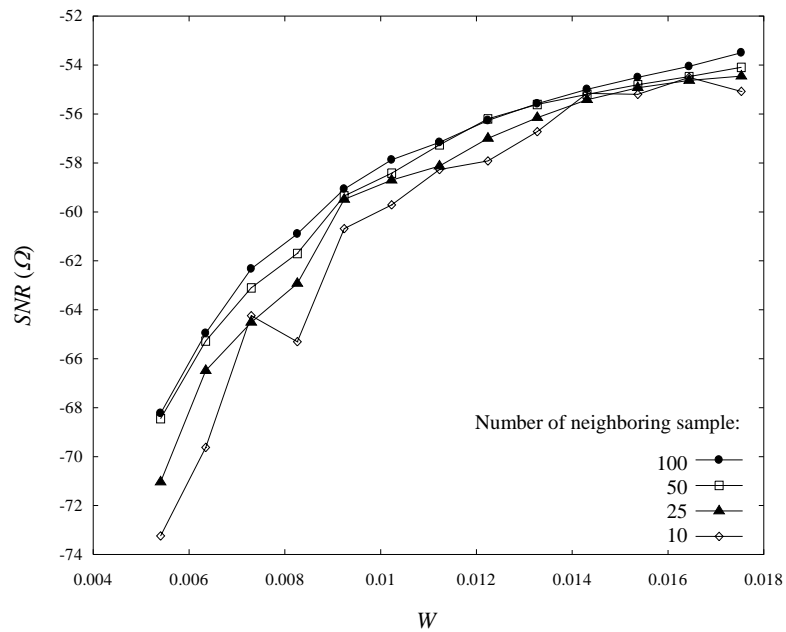


Figure 6.26 Convergence study of the signal-to-noise ratio of natural frequency. Neighborhood radius = 10%.

6.5.3 Stress

The coarsely meshed finite element models that were used in this study provide quite accurate results for natural frequency and deflection but are not accurate for determination of the stress. For this reason, we did not use stress as one of the objective functions but this does not necessarily imply that the robust-optimum designs are inferior in term of stress. In general, the designs that lead to lower deflection also have lower

stress. Figure 6.27 shows the maximum stress in the robust-optimum designs (obtained with the design guideline) compared to the trial design and flat plates. Note that, as we mentioned earlier, the stress solutions shown here are not accurate.

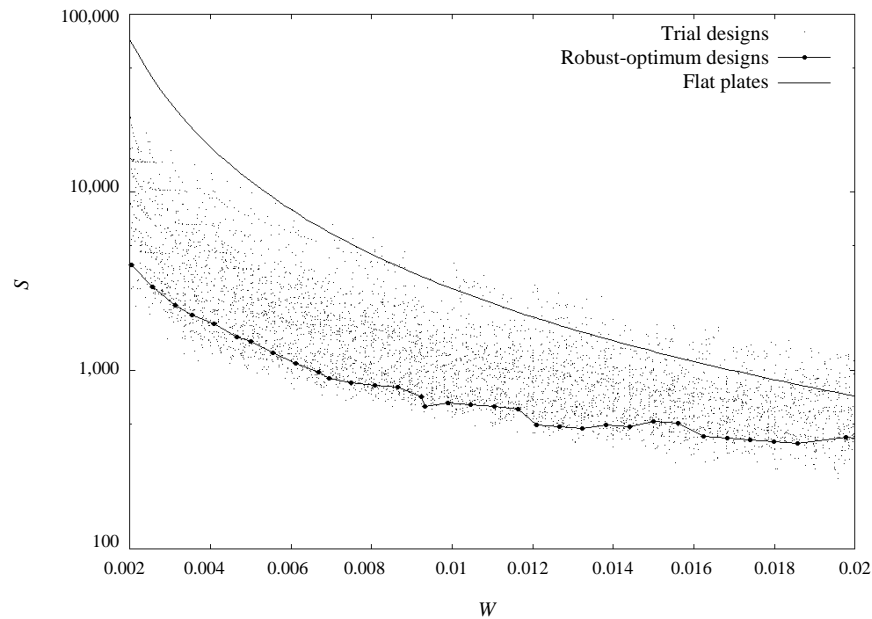


Figure 6.27 Maximum stress vs. weight.

6.5.4 Application of design rules

All the results are based on isotropic steel with a Poisson ratio of 0.29 so the rules can only be applied to steel and other alloys with similar Poisson ratio. Cross-sectional geometry of the corrugated plates is based on the three basis shapes in Fig. 6.5. Moreover, the computations are carried out only for square plates (aspect ratio = 1) under uniformly distribution loads with simply supported edges. The design rules are only valid in the range of $0.002 \leq W \leq 0.02$. However the rules may be used to suggest initial designs for design problems in the following cases.

Clamped supports

With clamped supports the suggested design will lead to a better performance in terms of deflection and natural frequency than that given in Fig. 6.21a and b.

Support on two opposite edges only

The ridges of the corrugated plate should be aligned parallel to the edges without the support. Dimension a should be based on the length of the unsupported edges.

Different aspect ratios

The dimension a should be based on the length of the shorter edges and the ridges of the corrugated plate should be parallel to the shorter edges.

Chapter 7

Concluding Remarks

This research focuses on the development of an optimum and robust design methodology by integrating existing CAD and CAE tools. We have demonstrated such integration in Chapter 4 for design optimization. In the CAD part of the work, use of NURBS curves (Bezier and B-spline form) allows the design space to be explored using only a few design variables. Moreover, the degree elevation property of Bezier curves enables us to explore the design space with minimal number of control points at first and progressively increase the number as needed. The CAE tools (governing equation solvers such as the flow solvers) are used as black boxes. A generic optimization algorithm was developed based on the black-box approach with the use of design of experiments (DOE) and steepest descent techniques and a computer program (“*optimizer*”) is written based on this algorithm. We were able to integrate the optimizer with several black-box solvers through the use of previously described CAD tools. In all the examples there are 3 to 5 design variables and they require direct solutions numbering $O(100)$ to converge to an optimum solution. These numbers can be decreased by improving the optimizer. One of the possible ways to increase efficiency of the optimizer is to develop some means (e.g.

some form of a trust region analysis) to track the behavior of the local response function during the search in order to automatically select a suitable DOE technique (finite difference, factorial design or small composite design) for each design iteration. For further improvement, one can also use the information obtained from the DOE such as the effects of each control point to identify the most sensitive region along the curve and specifically add more control points to that region instead of simply using a degree elevation algorithm.

A robustness analysis methodology was developed and tested in Chapter 5. In order to simulate noise, we perturbed the original geometry within a given tolerance zone using B-spline error curves. The effect of noise is quantified using mean, standard deviation, probability of failure (*POF*) and signal-to-noise ratios (*SNR*). The *SNR* and *POF* were found to be useful tools for robustness analysis. With these tools, we are able to identify robust designs in four example problems and show that an optimum design is not necessarily robust. We found that *SNR* is a quick tool for a relative comparison of different design while *POF* is a more meaningful quantity in an absolute sense. For use of *POF* as a measure, one needs to explore the use of appropriate probability distribution function. Moreover the patterns used for noise simulations should be designed to provide a good approximation of a distribution of noise if such a distribution is known.

In Chapter 6, a fixed-form (as opposed to free-form) geometric design problem is explored. The specific problem investigated is that of design of corrugated panel structures as a multicriteria, fixed-form geometric design problem. We continue using the

idea of a black-box solver and were able to automate the direct solution process. This enables us to explore the design space very exhaustively. A total computational time of 150 hours on a 500 MHz Pentium III machine was spent in solving for natural frequency and deflections of 4500 trial designs using I-DEAS Master Series 7 software. Since the design space is filled with a large number of trial designs, we are able to perform robustness analysis on every trial design by using the neighboring designs to represent the effect of noise. We use *SNR* for quick comparisons of robustness among the designs. After an intensive analysis of this information we observe a pattern among the design variables of the “robust-optimum designs” and we propose them as robust-optimum design rules.

One can see from the work presented in this thesis that complex design problems can be solved with integration of relatively simpler engineering tools. As CAD, CAE and CAM tools become more mature it is important for engineers to realized the capability of these existing tools and make most use out of them by using them together.

Bibliography

Armaly, B. F., F. Durst, J.C. F. Pereira and B. Sconung, 1983, "Experimental and theoretical investigation of backward-facing step flow", *Journal of Fluid Mechanics*, Vol. 127, pp. 473-496.

Bendsoe, M. P., 1989, "Optimal shape design as a material distribution problem", *Structural optimization*, No. 1, pp. 193-202.

Betti, R., 1997, "Finite element analysis I", Lecture note, Columbia University.

Boothroyd, G., P. Dewhurst and W. Knight, 1994, "Product design for manufacture and assembly", Marcel Dekker, Inc., New York.

Botkin, M. E., 1982, "Shape optimization of plate and shell structures", *AIAA Journal*, Vol. 20, No. 2, pp. 268-273.

Box, G. E. P. and K. B. Wilson, 1951, "On the experimental attainment of optimum conditions", *Journal of the royal statistical society, Series B*, Vol. 13, pp. 1-45.

Box, G. E. P. and D. W. Behnken, 1960, "Some new three-level design for the study of quantitative variables", *Technometrics*, Vol. 2, pp. 455-475.

Box, G. E. P., W. G. Hunter and J. S. Hunter, 1979, "Statistics for experiments" 2nd edition, Longman, London.

Box, G. E. P., 1988, "Signal-to-noise ratios performance criteria and transformations", *Technometrics*, Vol. 30, No. 1, pp. 1-18.

Cabuk, H. and V. Modi, 1990, "Shape optimization analysis: first- and second-order necessary conditions", *Optimal control applications and methods*, Vol. 11, pp. 173-190.

Cabuk, H. and V. Modi, 1992, "Optimum plane diffusers in laminar flow", *Journal of Fluid Mechanics*, Vol 237, pp. 373-393.

- Cagan, J. and B. Williams, 1993, "First-order necessary conditions for robust optimality", DE-Vol. 65-1, Advances in design automation, Vol. 1, ASME.
- Chen, W. and Xiaoping Du, 1999, "Towards a better understanding of modeling feasibility robustness in engineering design", Proceedings of the 1999 ASME Design Engineering Technical Conferences, paper no. DETC99/DAC-8565.
- Choi, K. K., and Haug, E. J., 1983, "Shape design sensitivity analysis of elastic structures", Journal of structure mechanics, Vol. 11, No. 2, pp 231-269.
- Farin G., 1993, "Curves and surfaces for computer aided geometric design: a practical guide" 3rd Edition, Academic Press, Inc.
- Faupel, H. H. and F. E. Fisher, 1981, "Engineering design: a synthesis of stress analysis and materials engineering", John Wiley & Sons, New York.
- Ferziger, J. H. and M. Peric, 1996, "Computational methods for fluid dynamics", Springer-Verlag.
- Ferziger, J. H., 1998, "Numerical methods for engineering applications", John Wiley & Sons.
- Haber, R. B., 1987, "A new variational approach to structural shape design sensitivity analysis", Computer aided optimal design: structural and mechanical system (ed. C.A. Mota Soares), NATO ASI series, Springer, pp. 573-588.
- Hooke, R. and T. A. Jeeves, 1961, "Direct search solution of numerical and statistical problems", ACM, vol 8, pp. 221-230.
- Hoschek, J. and D. Lasser, 1993, "Fundamentals of computer aided geometric design", A K Peters, Ltd.
- Hougen, E., 1968, "Probabilistic approaches to design", John Wiley and Sons.
- Huan, J. and V. Modi, 1996, "Design of minimum drag bodies in incompressible laminar flow", Inverse Problem in Engineering, vol. 3, pp. 233-260.
- Hwang, C. L. and A. S. M. Masud, 1979, "Multiple objective decision making: methods and application; a state-of the art survey", Springer, Berlin.
- Ignizio, J., 1976, "Goal programming and extensions", Lexington, Mass.
- Lee, C-L, Mioduchowski, A. and Faulkner, M.G., 1995, "Optimization of Corrugated Claddings", ASCE Journal of Structural Engineering, vol. 121, No. 8, pp. 1190-1196.

- Lee, D. J., A. C. Thornton, and T. Cunningham, 1995, "Key characteristics for agile product development and manufacturing," *Agility Forum 4th Annual Conference Proceedings*, March 7-9, 1995, Bethlehem, PA, pp. 258-268.
- Liggett, J. A. and P. L.-F Lui, 1983, "The Boundary integral method for porous media flow", George Allen & Unwin Ltd., London.
- Luo, J. and H. C. Gea, 1998, "A systematic topology optimization approach for optimal stiffener design", *Structural Optimization*, vol. 16, pp. 280-288.
- Meyer, M. H. and A. P. Lehnerd, 1997, "The power of product platforms", The Free Press, New York.
- Myers R. H., and D. C. Montgomery, 1995, "Response surface methodology: process and product optimization using designed experiments", John Wiley & Sons Inc.
- O'Rourke, J., 1993, "Computational geometry in C", Cambridge University Press.
- Pareto, V., 1906 "Manuale di economica politica, societa editrice libraria", Milano, Italy. (Translated into English by A.S. Schwier, "Manual of political economy", MacMillan, New York, 1971).
- Phadke, M. S., 1989, "Quality engineering using robust design", Prentice Hall.
- Pironneau, O., 1974, "On optimum design in fluid mechanics", *Journal of Fluid Mechanics*, Vol. 64, pp. 97-110.
- Pironneau, O., 1984, "Optimal shape design for elliptic systems", Springer-Verlag.
- Pottmann, H, B. Odehnal, M. Peternell, J. Wallner and R. Ait Haddou, 2000, "On optimal tolerancing in computer-aided design", *Geometric modeling and processing 2000*, edited by R. martin and W. Wang, IEEE Computer society, Los Alamitos, CA, pp. 347-363.
- Rahman, M. K., 1996, "Optimization of panel forms for improvement in ship structures", *Structural optimization*, vol. 11, pp. 195-212.
- Rao, J. S., 1999, "Dynamics of plates", Marcel Dekker, Inc., New York.
- Richards, R. A., 1995, "Zeroth-order shape optimization utilizing a learning classifier system" Ph.D. Dissertation, Mechanical Engineering Department, Stanford University.
- Schmidt, S. and R. Launsby, 1992, "Understanding industrial designed experiments", 3rd edition, Air Academy Press, Colorado.

Seaburg and Salmon, 1971, "Minimum weight design of light gage steel member", ASCE Journal of Structural Engineering, vol. 97, no. 1, pp.203-222.

Statnikov, R. B. and J. B. Matusov, 1995, "Multicriteria optimization and engineering", Chapman & Hall, New York.

Suh, N. P., 1990, "The principles of design", Oxford University Press, New York.

Taguchi, G., 1986, "Introduction to quality engineering: designing quality into products and processes", Asian Productivity Organization, Tokyo.

Timoshenko, S., 1940, "Theory of plates and shells", McGraw-Hill book company, Inc., New York.

Troitsky, M.S., 1967, "Orthotropic bridges theory and design", James F. Lincoln Arc Welding Foundation, Ohio.

Ulrich, K. T. and S. D. Eppinger, 1995, "Product design and development process", McGraw-Hill, Inc.

Wang, L. and R. V. Grandhi, 1996, "Multipoint approximations: comparisons using structural size, configuration and shape design", Structural Optimization, vol. 12, pp. 177-185.

Zagajac, J., 1998, "Constrained shape optimization: Can geometric modeling and engineering analysis system cooperate?", presented at the SIAM workshop on Mathematical Foundation for Feature in Computer-Aided Design Engineering and Manufacturing, October 1998, Troy, Michigan.

Zhang, S. and A. D. Belegundu, 1992, "A systematic approach for generating velocity fields in shape optimization", Structural Optimization, vol. 5, n 1-2, pp. 84-94.

Appendix

A. Multi-dimensional response function

This section provides a methodology to find coefficients of a response function by a least square approach. Consider a scalar value y that is a function of design variables $\mathbf{x} = (x_1, x_2, x_3, \dots, x_n)$. The exact relationship is unknown and is represented with a function F ; $y = F(\mathbf{x})$. We try to approximate the response of the function F with a response function \hat{F} ; $y = F(\mathbf{x}) \approx \hat{F}(\mathbf{x})$.

Let $\hat{F}(\mathbf{x}) = \sum_{i=1}^k c_i G_i(\mathbf{x})$ where c_i are unknown constant coefficients and G_i are

known functions and \hat{F} is called the response function. Two basic examples of response functions for $n = 3$ are given below

- linear response surface

$$k = n + 1 = 4$$

$$G_1 = 1, G_2 = x_1, G_3 = x_2 \text{ and } G_4 = x_3$$

- second-order response surface

$$k = \frac{1}{2} n (n - 1) + 2n + 1 = 10$$

$$G_1 = 1, G_2 = x_1, G_3 = x_2, G_4 = x_3,$$

$$G_5 = x_1^2, G_6 = x_2^2, G_7 = x_3^2,$$

$$G_8 = x_1 x_2, G_9 = x_1 x_3 \text{ and } G_{10} = x_2 x_3$$

To obtain the coefficients of the response function, first we must have a sufficient number of samples, $m \geq k$. A set of m samples can be written in the form of: $F(\mathbf{x}^i) = d^i$, $i = 1, 2, 3, \dots, m$. Then match the response function to the data set and write it in the matrix form as:

$$\mathbf{GC} = \mathbf{D}$$

$$\text{Where } \mathbf{G} = \begin{bmatrix} G_1(\mathbf{x}^1) & G_2(\mathbf{x}^1) & G_3(\mathbf{x}^1) & \dots & G_k(\mathbf{x}^1) \\ G_1(\mathbf{x}^2) & G_2(\mathbf{x}^2) & G_3(\mathbf{x}^2) & \dots & G_k(\mathbf{x}^2) \\ G_1(\mathbf{x}^3) & G_2(\mathbf{x}^3) & G_3(\mathbf{x}^3) & \dots & G_k(\mathbf{x}^3) \\ \vdots & & & & \vdots \\ G_1(\mathbf{x}^m) & \dots & & & G_k(\mathbf{x}^m) \end{bmatrix}$$

$$\mathbf{C} = \begin{bmatrix} c_1 \\ c_2 \\ c_3 \\ \vdots \\ c_k \end{bmatrix} \text{ and } \mathbf{D} = \begin{bmatrix} d^1 \\ d^2 \\ d^3 \\ \vdots \\ d^m \end{bmatrix}$$

The coefficient \mathbf{C} can be obtained from

$$\mathbf{C} = (\mathbf{G}^T \mathbf{G})^{-1} \mathbf{G}^T \mathbf{D}$$

This approach is called least square fitting because the response function obtained this way will minimize the square of error. This can be shown as the following;

Let \mathbf{E} be the error, $\mathbf{E} = \mathbf{D} - \mathbf{GC}$.

And let \mathbf{J} be the square of error,

$$\mathbf{J} = (\mathbf{D} - \mathbf{GC})^2 = \mathbf{D}^T \mathbf{D} - 2\mathbf{G}^T \mathbf{C}^T \mathbf{D} + \mathbf{C}^T \mathbf{G}^T \mathbf{GC}.$$

To find \mathbf{C} that minimize \mathbf{J} , set

$$\frac{d\mathbf{J}}{d\mathbf{C}} = -2\mathbf{G}^T \mathbf{D} + 2\mathbf{G}^T \mathbf{GC} = 0$$

$$\mathbf{C} = (\mathbf{G}^T \mathbf{G})^{-1} \mathbf{G}^T \mathbf{D}$$

B. Validation of the black-box solver

B.1 Potential flow solver

The potential flow solver by Liggett and Lui (1983) is designed to solve the Laplace equation using boundary element method. With this method, only the boundaries are required to be discretized, no internal grid is required. We test this solver for accuracy and grid convergence with a potential flow through a channel in Fig. B.1

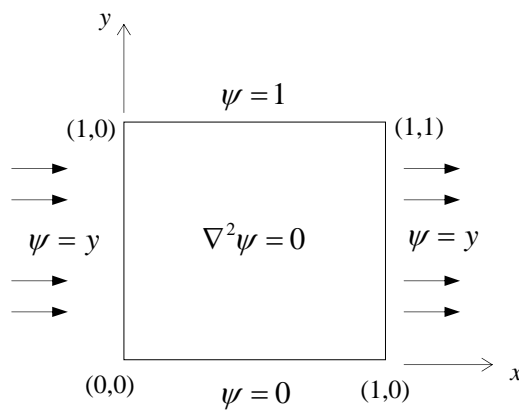


Figure B.1 Potential flow through a channel.

The average of magnitude of the transverse velocity components on the inlet and outlet boundaries is computed as V_{avg} . The theoretical value is trivial and is equal to zero. The solutions of V_{avg} for different element sizes are shown in Fig. B.2. The figure shows that the solutions converge to the theoretical value of zero as the element sizes are reduced.

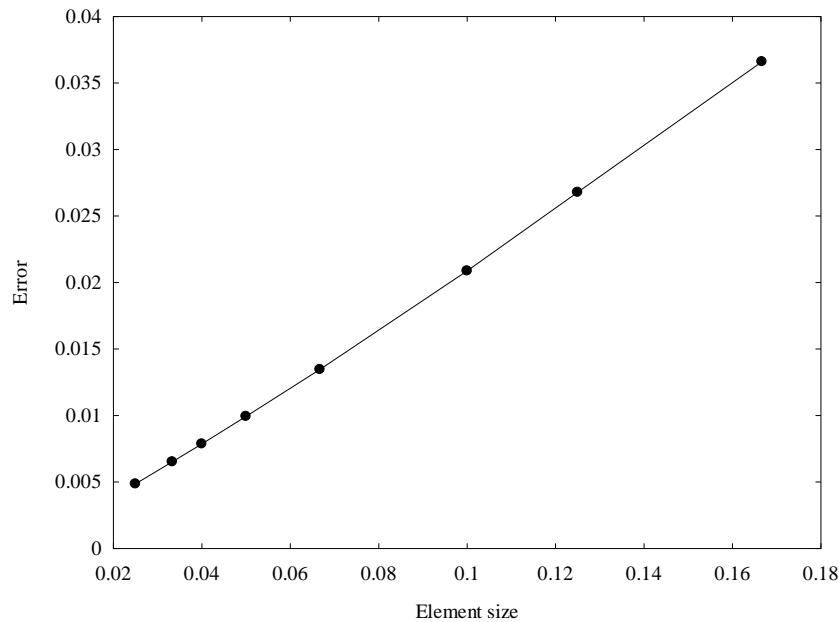


Figure B.2 Convergence study of the boundary element solver.

B.2 Laminar flow solver – CAFFA

CAFFA is developed by Ferziger and Peric (1996). It solves Navier-Stokes equations for incompressible laminar flow. The solver is designed to work with two-dimensional, non-orthogonal, multi-level structured grid using SIMPLE algorithm. We test CAFFA with a planar channel with backward-facing step on the lower wall as shown in Fig. B.3. According to the experimental result by Armaly et. al. (1983) the reattachment points vary with the inflow Reynolds number. The tests are conducted at $Re = 50, 100, 150$ and 200 . Initially the computational domain is divided into 50×10 control volumes, CAFFA then subdivides the grids in half, i.e. second grid level is 100×20 and third grid level is 200×40 . In Fig. B.4, a plot between distance to the reattachment point, X_r and Reynolds number is presented. We observe from the figure that the flow solver does have grid convergence behavior and that the trend of numerical results agrees with

that of experimental results. However, due to the strong re-circulation (as shown in Fig. B.5 for $Re = 100$), it is normal for the flow solver has a certain amount of error in predicting the flow field.

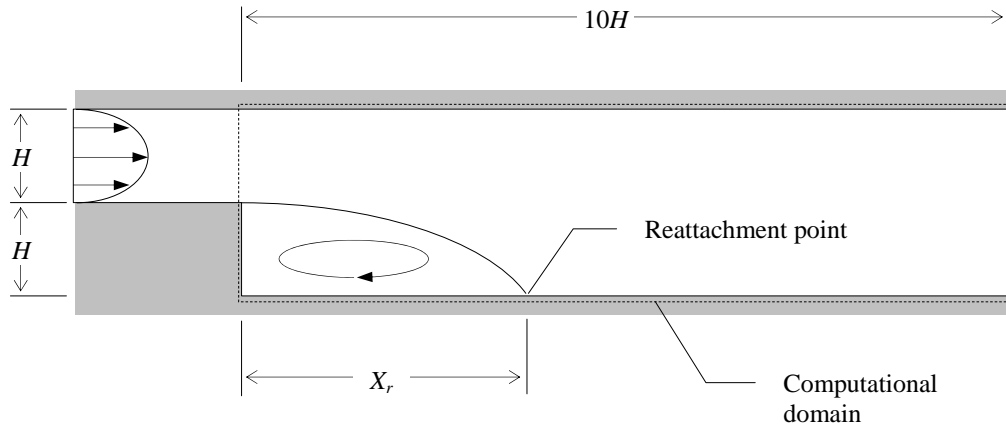


Figure B.3 Schematic diagram of flow in a planar channel with a backward-facing step on the lower wall.

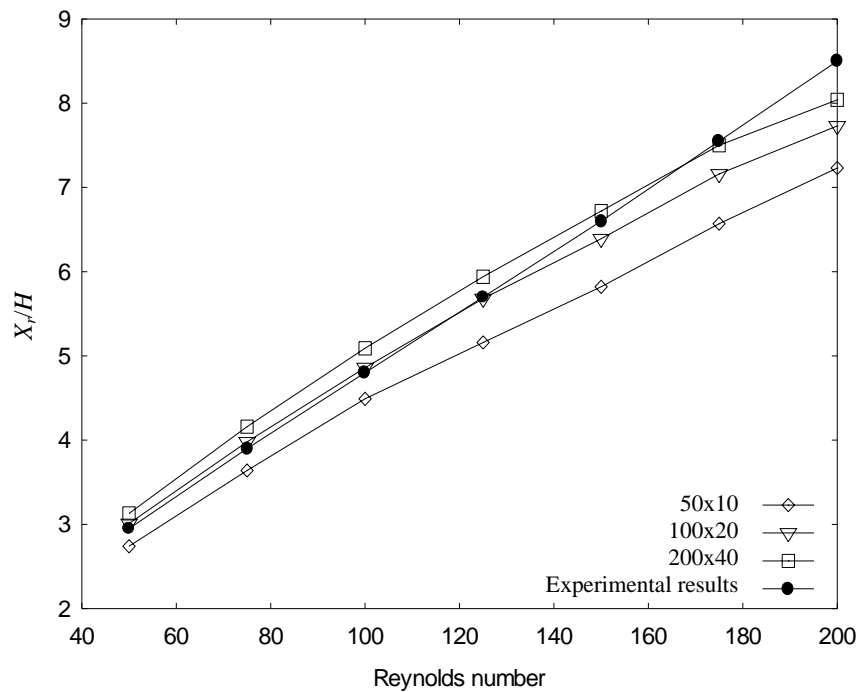


Figure B.4 Grid convergence study of CAFFA flow solver

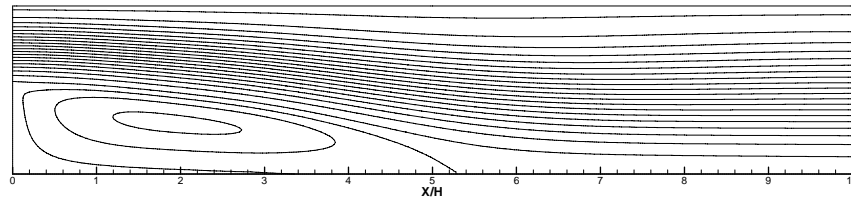


Figure B.5 Streamline plot of the flow in a planar channel with a backward-facing step on the lower wall. $Re = 100$.

B.3 Static finite element solver

The finite element flow solver is developed by Betti (1997). It solves two dimensional linear quadrilateral shell elements for stress and deflection. We use a simple cantilever beam problem to test grid convergence property of this solver. The configuration of the problem is shown in Fig. B.6. The thickness of the beam is t , and Young's modulus is E

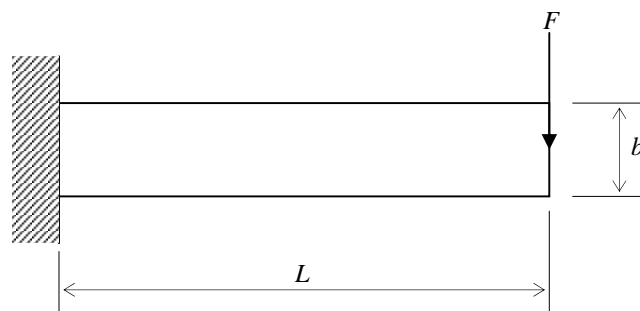


Figure B.6 Cantilever beam

The theoretical solutions for stress and maximum deflection are;

$$\sigma_{\max} = \frac{4FL^3}{Eb^3t}$$

$$\delta_{\max} = \frac{FL^3}{3EI}, \quad I = \frac{b^3t}{12}$$

We consider those theoretical solutions as exact solutions. The numerical solutions are performed with different element sizes. Figure B.7 shows decreasing in errors as element sizes decrease.

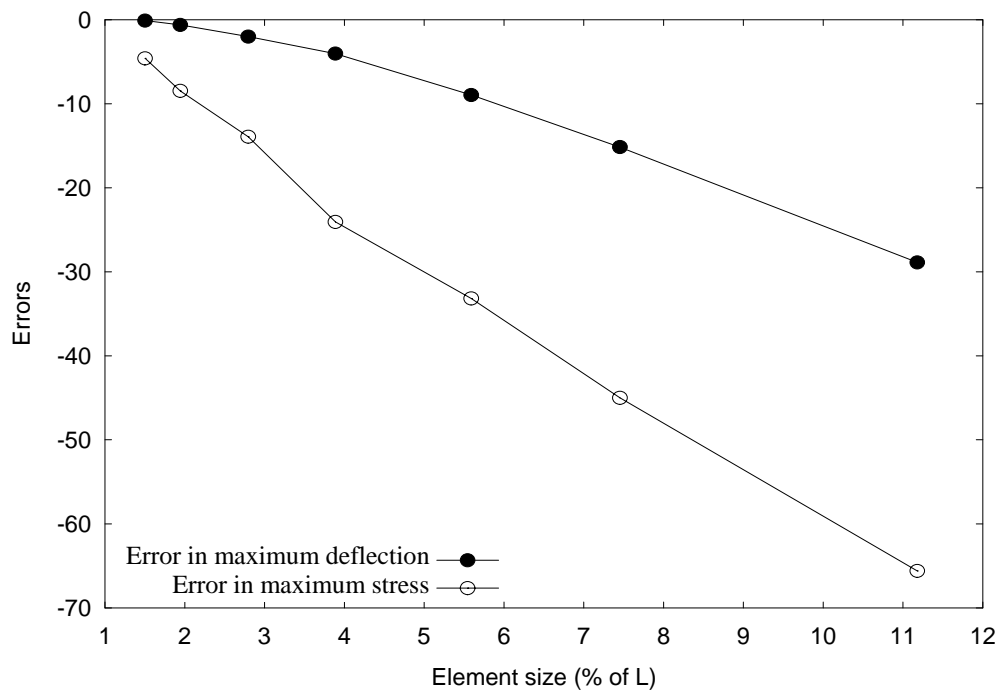


Figure B.7 Grid convergence study of the finite element solver.

B.4 I-DEAS linear statics and normal mode dynamics solvers

The solvers are validated with a simple problem of a thin square plate of thickness t and width a with simply supports on all four edges. For static solution the plate is subjected to a uniformly distributed load of intensity q . The analytical solutions for maximum deflection, maximum stress and natural frequency are

$$u_{\max} = 0.00406 \frac{a^4 q}{D}$$

$$\sigma_{\max} = 0.287q \frac{a^2}{t^2}$$

and

$$\omega = 0.907 \frac{t}{a^2} \sqrt{\frac{E}{\rho(1-\nu^2)}} \quad \text{where } D = \frac{Et^3}{12a(1-\nu^2)}.$$

Figure B.8 shows that magnitudes of errors of the numerical solutions of u_{\max} and ω decrease with the decreasing element sizes. Stress solutions do not exhibit grid convergence behavior.

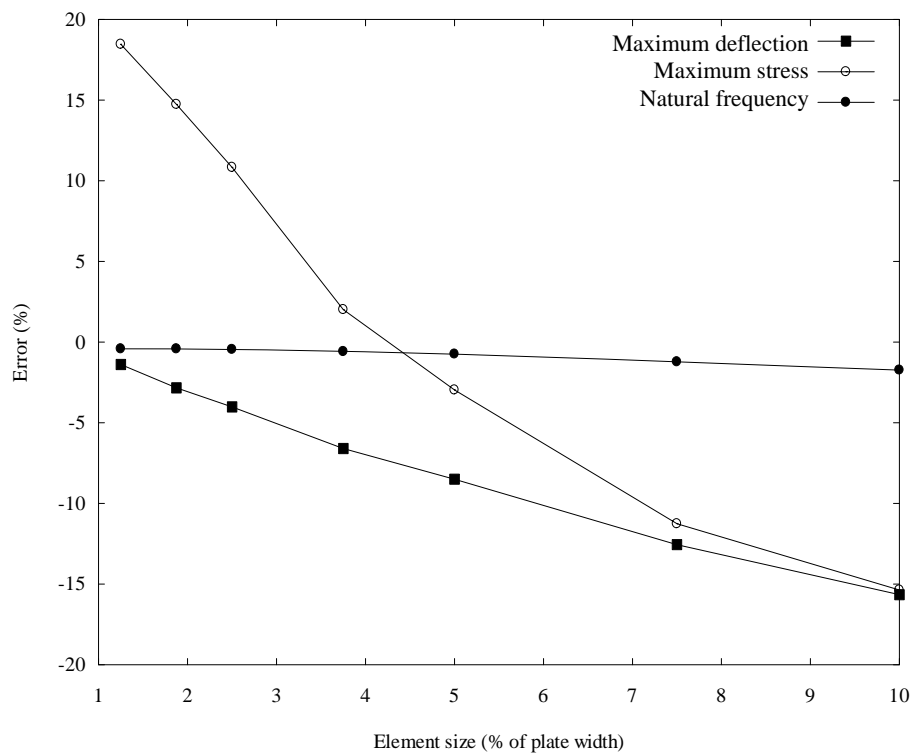


Figure B.8 Grid convergence study of I-DEAS finite element solvers.

C. Batch mode program for I-DEAS Master Series 7

In order to generate solutions for a large set of trial designs in Chapter 6, batch program is used. I-DEAS geometry based finite element model is not suitable for batch operation in this case because topology changes from one design to another. This makes it hard to select surface in grid generation process. To by-pass this problem, for each design a finite element model consisted of nodal coordinates, nodal connectivity and boundary conditions is generated by a Fortran program and input to I-DEAS via program files (node.prg, element.prg, restraint.prg and force.prg). The main program file, run.prg, is written manually to execute those program files. Run.prg is invariant with design changes. The procedures are described with Fig. C.1 and followed by example of program files.

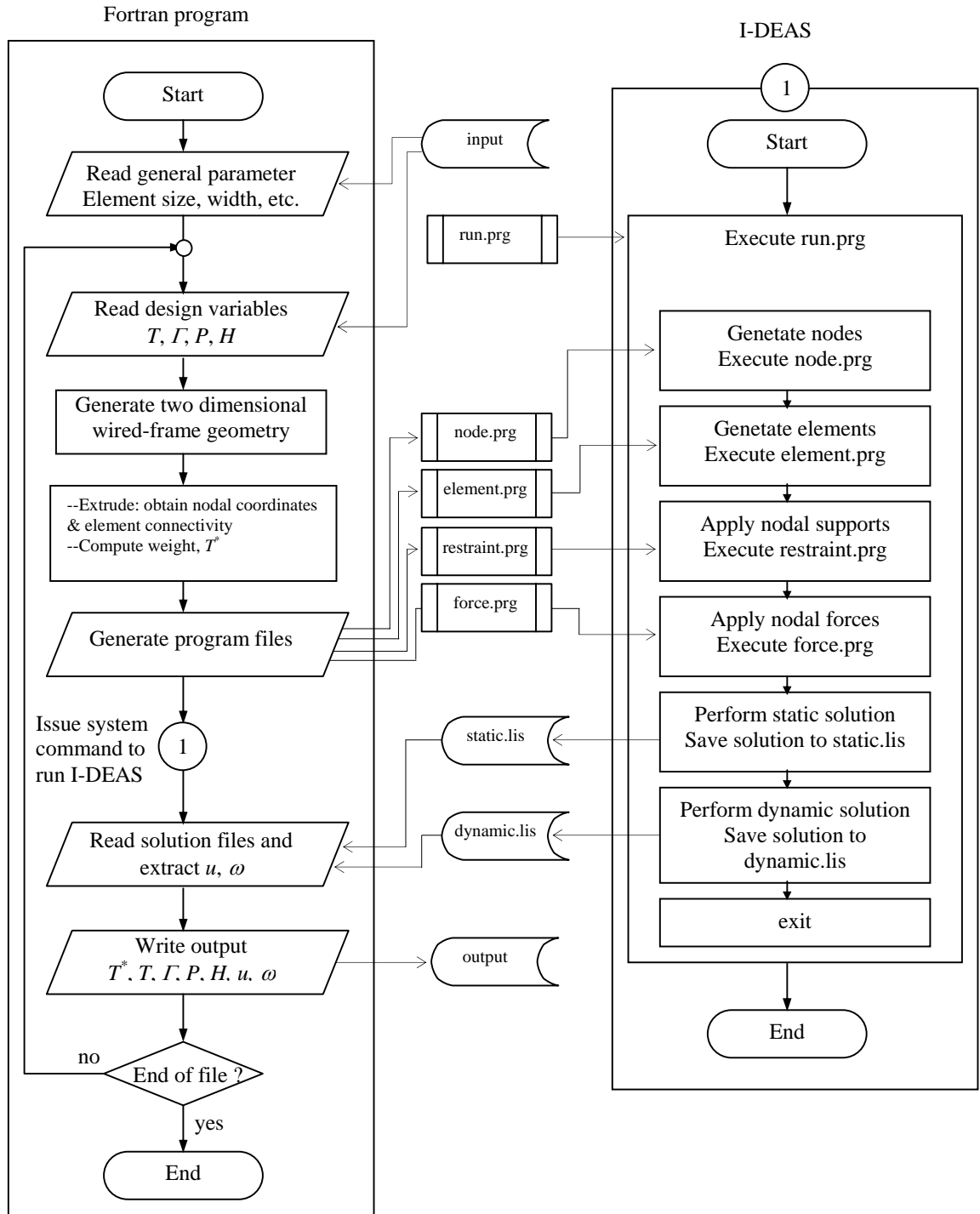


Figure C.1 Flow chart of I-DEAS batch mode program.

In Fig. C.1 the system command issued from Fortran program to run I-DEAS in batch mode is:

```
d:\ideas\ms7\bin\ideas.cmd -b -q -g -m "DUL01" -a SI -e "/f pr r fil run.prg"; okay
```

run.prg

```

K : $ return
K : $ /ta ME
CL: ---Create nodes
K : $ /f pr r fil node.prg; okay
CL: ---Set isometric view
K : $ mpos ;; /v v pe of; e 3 4 5 0;
okay;
K : $ AU
CL: ---Create THIN SHELL1 elements
K : $ /f pr r fil element.prg; okay
CL: ---Boundary conditions-statics
K : $ /ta BO
K : $ mpos ;; /a li
K : $ mpos ;; /b
K : $ okay;
CL: ---Restraint set
K : $ /f pr r fil restrain.prg; okay
CL: ---Forces
K : $ /f pr r fil force.prg; okay
K : $ /ta bo b
K : SE RT ON
K : ! SE LO 1;
K : APPL
K : OKAY
CL: ---Model solution--linear statics
K : $ /ta MO
K : $ mpos ;; /ss
K : CRE
K : OKAY
CL: 1 - SOLUTION SET1
K : DMN 1;
K : MOD
K : OS
K : OTY 1;
K : STL STI
K : OTY 2;
K : STL STI
K : APPL
K : OKAY
K : OKAY
K : CANC
CL: ---solve
K : $ mpos ;; /so
K : LOF statics.lis
K : OKAY
CL: ---Delete linear static solution
K : $ /ta MO
K : $ mpos ;; /ss
K : DMN 1;
K : DEL
K : Y
K : CANC
CL: ---Boundary condition--dynamics
K : $/ ta BO
K : $ mpos ;; /a no
K : $ mpos ;; /b
K : SE RT ON
K : APPL
K : OKAY
CL: ---Model solution--dynamics
K : $ $ $ /ta MO
K : $ mpos ;; /ss
K : CRE
K : TY NDL
K : OKAY
CL: 1 - SOLUTION SET1
K : DMN 1;
K : MOD
K : OS
K : OTY 1;
K : STL STI
K : APPL
K : OKAY
K : OKAY
K : CANC
CL: ---solve
K : $ mpos ;; /so
K : LOF dynamics.lis
K : OKAY
CL: ---exit, no save
K : $/f e n:
E : **** END OF SESSION ****

```

node.prg

```

K : $ return
K : $ /ta me n cr
K : OKAY
K : Y
K : OKAY
K : 0.0000,0.0000,0.0000
K : 25.000,0.0000 ,0.0000
K : 50.000 ,0.0000 ,0.0000
K : 75.000 ,0.0000 ,0.0000
K : 100.00 ,0.0000 ,0.0000
K : 125.00 ,0.0000 ,0.0000
K : 150.00 ,0.0000 ,0.0000
K : 175.00 ,0.0000 ,0.0000

...

K : 935.13 , -66.667 ,1000.0
K : 930.07 , -33.333 ,1000.0
K : 959.80 , -100.00 ,1000.0
K : 964.87 , -66.667 ,1000.0
K : 969.93 , -33.333 ,1000.0
K : done
K :
E :
```

element.prg

```

K : $ return
K : $ /ta me e cr
K : EL D2
K : EF TN
K : P 1
K : ET LQ
K : OKAY
K : LAB
K : 2; 3; 114; 113
K : 3; 4; 115; 114
K : 6; 7; 118; 117
K : 7; 8; 119; 118
K : 10; 11; 122; 121

...

K : 2145; 2146; 2257; 2256
K : 2146; 2147; 2258; 2257
K : 2149; 2150; 2261; 2260
K : done:
K : $ return
K : $ mpos ; /ph mo
K : 3
K : 1
K : 23.500 ;0;0;0
K : done:
E :
```

restraint.prg

```

K : $ return
K : $ /ta bo cr re
K : LAB
K :
K : node
K : 1
K : 2
K : 3
K : 4

...

K : 2028
K : 2029
K : don
K : RT B
K : okay
K :
E :
```

force.prg

```

K : $ return
K : $ /ta bo cr f
K : LAB
K :
K : node
K : 1;
K : don
K : XF 0.00
K : YF -0.116E+05
K : ZF 0.00
K : okay
K :
K : $ /ta bo cr f
K : LAB
K :
K : node
K : 102;
K : don
K : XF 0.00
K : YF -0.116E+05
K : ZF 0.00
K : okay
K :

...

K :
E :
```